Draft version April 26, 2019
Typeset using LaTeX **modern** style in AASTeX61

THE DEATH THROES OF A STRIPPED MASSIVE STAR: AN ERUPTIVE MASS-LOSS HISTORY ENCODED IN PRE-EXPLOSION EMISSION, A RAPIDLY RISING LUMINOUS TRANSIENT, AND A BROAD-LINED IC SUPERNOVA

Anna Y. Q. Ho,[1] Daniel A. Goldstein,[1,*] Steve Schulze,[2]
David K. Khatami,[3] Daniel A. Perley,[4] Mattias Ergon,[5] Avishay Gal-Yam,[2]
Alessandra Corsi,[6] Igor Andreoni,[1] Cristina Barbarino,[5] Eric C. Bellm,[7]
Nadia Blagorodnova,[8] Joe S. Bright,[9] E. Burns,[10] S. Bradley Cenko,[11,12]
Virginia Cunningham,[13] Kishalay De,[1] Richard Dekany,[14] Alison Dugas,[1]
Rob P. Fender,[9] Claes Fransson,[5] Christoffer Fremling,[15]
Adam Goldstein,[16] Matthew J. Graham,[15] David Hale,[14] Assaf Horesh,[17]
Tiara Hung,[18] Mansi M. Kasliwal,[1] N. Paul M. Kuin,[19] S. R. Kulkarni,[1]
Thomas Kupfer,[20] Ragnhild Lunnan,[5] Frank J. Masci,[21]
Chow-Choong Ngeow,[22] Peter E. Nugent,[23] Eran O. Ofek,[2]
Maria T. Patterson,[7] Glen Petitpas,[24] Ben Rusholme,[21] Hanna Sai,[25]
Itai Sfaradi,[17] David L. Shupe,[21] Jesper Sollerman,[5]
Maayane T. Soumagnac,[2] Yutaro Tachibana,[26] Francesco Taddia,[5]
Richard Walters,[1] Xiaofeng Wang,[25] Yuhan Yao,[1] and Xinhan Zhang[25]

[1] *Cahill Center for Astrophysics, California Institute of Technology, MC 249-17, 1200 E California Boulevard, Pasadena, CA, 91125, USA*

[2] *Department of Particle Physics and Astrophysics, Weizmann Institute of Science, 234 Herzl St, 76100 Rehovot, Israel*

[3] *Department of Astronomy, University of California, Berkeley, CA, 94720*

[4] *Astrophysics Research Institute, Liverpool John Moores University, IC2, Liverpool Science Park, 146 Brownlow Hill, Liverpool L3 5RF, UK*

[5] *The Oskar Klein Centre & Department of Astronomy, Stockholm University, AlbaNova, SE-106 91 Stockholm, Sweden*

[6] *Department of Physics and Astronomy, Texas Tech University, Box 1051, Lubbock, TX 79409-1051, USA*

[7] *DIRAC Institute, Department of Astronomy, University of Washington, 3910 15th Avenue NE, Seattle, WA 98195, USA*

[8] *Department of Astrophysics/IMAPP, Radboud University, Nijmegen, The Netherlands*

[9] *Department of Physics, University of Oxford, Denys Wilkinson Building, Keble Road, Oxford OX1 3RH, UK*

[10] *NASA Postdoctoral Program Fellow, Goddard Space Flight Center, Greenbelt, MD 20771, USA*

[11] *Astrophysics Science Division, NASA Goddard Space Flight Center, Mail Code 661, Greenbelt, MD 20771, USA*

[12] *Joint Space-Science Institute, University of Maryland, College Park, MD 20742, USA*

[13] *Astronomy Department, University of Maryland, College Park, MD 20742, USA*
[14] *Caltech Optical Observatories, California Institute of Technology, MC 11-17, 1200 E. California Blvd., Pasadena, CA 91125 USA*
[15] *Division of Physics, Mathematics and Astronomy, California Institute of Technology, Pasadena, CA 91125, USA*
[16] *Science and Technology Institute, Universities Space Research Association, Huntsville, AL 35805, USA*
[17] *Racah Institute of Physics, Hebrew University, Jerusalem 91904, Israel*
[18] *Department of Astronomy and Astrophysics, University of California, Santa Cruz, CA 95064, USA*
[19] *Mullard Space Science Laboratory, University College London, Holmbury St. Mary, Dorking, Surrey RH5 6NT, UK*
[20] *Kavli Institute for Theoretical Physics, University of California, Santa Barbara, CA 93106, USA*
[21] *IPAC, California Institute of Technology, 1200 E. California Blvd, Pasadena, CA 91125, USA*
[22] *Graduate Institute of Astronomy, National Central University, 32001, Taiwan*
[23] *Lawrence Berkeley National Laboratory, 1 Cyclotron Road, Berkeley, CA, 94720, USA*
[24] *Harvard-Smithsonian Center for Astrophysics, 60 Garden Street, Cambridge, MA 02138, USA*
[25] *Physics Department/Tsinghua Center for Astrophysics, Tsinghua University; Beijing, 100084, China*
[26] *Department of Physics, Tokyo Institute of Technology, 2-12-1 Ookayama, Meguro-ku, Tokyo 152-8551, Japan*

ABSTRACT

We present detailed observations of ZTF18abukavn (SN2018gep), discovered in high-cadence data from the Zwicky Transient Facility as a rapidly rising (1.3 mag/hr) and luminous ($M_{g,\mathrm{peak}} = -20$ mag) transient. It is spectroscopically classified as a broad-lined stripped-envelope supernova (Ic-BL SN). The rapid rise to peak bolometric luminosity and blue colors at peak (t_{rise} ∼0.5–3 day, $L_{\mathrm{bol}} \gtrsim 3 \times 10^{44}\,\mathrm{erg\,s^{-1}}$, $g - r = -0.3$) resemble the high-redshift Ic-BL iPTF16asu, as well as several other unclassified fast transients. The early discovery of SN2018gep (within an hour of shock breakout) enabled an intensive spectroscopic campaign, including the highest-temperature ($T_{\mathrm{eff}} \gtrsim 40,000$K) spectra of a stripped-envelope SN. A retrospective search revealed luminous ($M_g \sim M_r \approx -14\,\mathrm{mag}$) emission in the days to weeks before explosion, the first definitive detection of precursor emission for a Ic-BL. We find a limit on the isotropic gamma-ray energy release $E_{\gamma,\mathrm{iso}} < 4.9 \times 10^{48}\,\mathrm{erg}$, a limit on X-ray emission $L_{\mathrm{X}} < 10^{40}\,\mathrm{erg\,s^{-1}}$, and a limit on radio emission $\nu L_\nu \lesssim 10^{37}\,\mathrm{erg\,s^{-1}}$. Taken together, we find that the data are best explained by shock breakout in a massive shell of dense circumstellar material ($0.02\,M_\odot$) at large radii (3×10^{14} cm) that was ejected in eruptive pre-explosion mass-loss episodes.

* Hubble Fellow

1. INTRODUCTION

Recent discoveries by optical time-domain surveys challenge our understanding of how energy is deposited and transported in stellar explosions (Kasen 2017). For example, ~ 100 transients have been discovered with rise times and peak luminosities too rapid and too high, respectively, to be explained by radioactive decay (Poznanski et al. 2010; Drout et al. 2014; Shivvers et al. 2016; Tanaka et al. 2016; Arcavi et al. 2016; Rest et al. 2018; Pursiainen et al. 2018). Possible powering mechanisms include interaction with extended circumstellar material (CSM; Chevalier & Irwin 2011), and energy injection from a long-lived central engine (Kasen & Bildsten 2010; Woosley 2010; Kasen et al. 2016). These models have been difficult to test because the majority have been discovered *post facto* and located at cosmological distances ($z \sim 0.1$).

The discovery of iPTF16asu (Whitesides et al. 2017) in the intermediate Palomar Transient Factory (iPTF; Law et al. 2009) showed that at least some of these fast-luminous transients are energetic (10^{52} erg) high-velocity ("broad-lined"; $v \gtrsim 20,000\,\mathrm{km\,s^{-1}}$) stripped-envelope (Ic) supernovae (Ic-BL SNe). The light curve of iPTF16asu was unusual in being inconsistent with ^{56}Ni-decay (Cano 2013; Taddia et al. 2019). Possible power sources included energy injection by a magnetar, cooling-envelope emission from CSM interaction, and an engine-driven explosion similar to low-luminosity gamma-ray bursts. However, the high redshift ($z = 0.187$) precluded a definitive conclusion.

Today, optical surveys such as ATLAS (Tonry et al. 2018) and the Zwicky Transient Facility (ZTF; Bellm et al. 2019a; Graham et al. 2019) have the areal coverage to discover rare transients *nearby*, as well as the cadence to discover transients when they are young (< 1 day). For example, the recent discovery of AT2018cow at 60 Mpc (Smartt et al. 2018; Prentice et al. 2018) represented an unprecedented opportunity to study a fast-luminous optical transient up close, in detail, and in real-time. Despite an intense multiwavelength observing campaign, the nature of AT2018cow remains unknown – possibilities include an engine-powered stellar explosion (Perley et al. 2019a; Margutti et al. 2019; Ho et al. 2019) and the tidal disruption of a white dwarf by an intermediate-mass black hole (Kuin et al. 2018; Perley et al. 2019a). Regardless of the origin, it is clear that the explosion took place within a dense environment (Perley et al. 2019a; Margutti et al. 2019; Ho et al. 2019).

Here we present SN2018gep, discovered as a rapidly rising ($1.3\,\mathrm{mag\,hr^{-1}}$) and luminous ($M_{g,\mathrm{peak}} = -20$) transient in high-cadence data from ZTF (Ho et al. 2018b). The high inferred velocities ($> 20,000\,\mathrm{km\,s^{-1}}$), the spectroscopic evolution from a blue continuum to a Ic-BL SN (Costantin et al. 2018), the rapid rise (t_{rise} $\sim$0.5–3 day) to high peak luminosity ($L_{\mathrm{bol}} \gtrsim \times 10^{44}\,\mathrm{erg\,s^{-1}}$) all suggest that SN2018gep is the first low-redshift analog to iPTF16asu. The early discovery enabled an intensive follow-up campaign within the first day of the explosion, including the highest-temperature

($T_{\rm eff} \gtrsim 40,000\,$K) spectra of a stripped-envelope SN to-date. A retrospective search in ZTF data revealed the first definitive detection of pre-explosion activity in a Ic-BL.

The structure of the paper is as follows. We present our radio through X-ray data in Section 2. In Section 3 we outline basic properties of the explosion and its host galaxy. In Section 4 we attribute the power source for the light curve to shock breakout in extended CSM. In Section 5 we compare SN2018gep to unidentified fast-luminous transients at high redshift. Finally, in Section 6 we summarize our findings and look to the future. Throughout the paper, absolute times are reported in UTC and relative times are reported with respect to t_0, which is defined in Section 2.1. We assume a standard ΛCDM cosmology (Planck Collaboration 2016).

2. OBSERVATIONS

2.1. *Zwicky Transient Facility Discovery*

ZTF18abukavn was discovered in the ZTF extragalactic high-cadence partnership survey, which covers $1725\,\mathrm{deg}^2$ in six visits per night, 3 in g-band and 3 in r-band (Bellm et al. 2019b). The light curve passed a filter in the GROWTH marshal (Kasliwal et al. 2019) written for infant SNe. ZTF employs a custom mosaic camera (Dekany et al. 2016) on the 48-inch Samuel Oschin Telescope (P48) at Palomar Observatory. Images are processed and reference-subtracted by the IPAC ZTF pipeline (Masci et al. 2019) using the method described in Zackay et al. (2016). P48 zero-points are derived using the Pan-STARRS1 catalog (Flewelling et al. 2016).

ZTF18abukavn was discovered in an image taken at 2018-09-09 03:55:17.760 (start of exposure). In this image, the source position was measured to be R.A. = 16:43:48.22, decl. = +41:02:43.4 (J2000), coincident with a compact galaxy (Figure 1). The magnitude was $r = 20.5 \pm 0.3\,$mag. Spectra obtained after the discovery showed narrow galaxy emission lines at $z = 0.03154$ or $d \approx 143\,$Mpc.

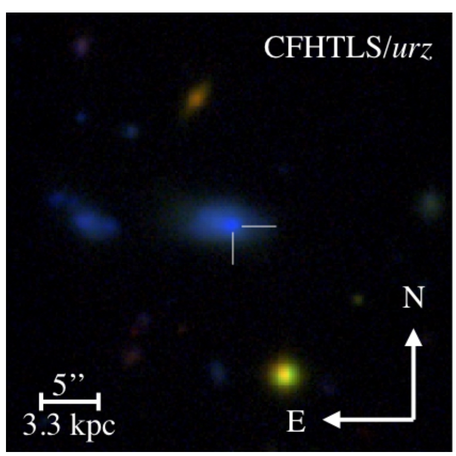

Figure 1. The position of SN2018gep (white crosshairs) in its host galaxy. Images from the Canada-France-Hawaii Telescope Legacy Survey (2004–2012), combined using the prescription in Lupton et al. (2004).

As shown in Figure 2, the source brightened by over two magnitudes within three hours of discovery, and over the next two days by two additional magnitudes. Lowering the threshold for detection from 5-σ to 3-σ showed an additional r-band point prior to the discovery. A linear fit to the early g-band photometry gives a rise of $1.3\,\mathrm{mag\,hr^{-1}}$ at a discovery magnitude of $M_g \approx -17\,\mathrm{mag}$. This rise rate is second only to the IIb SN 16gkg (Bersten et al. 2018) but several orders of magnitude more luminous at discovery.

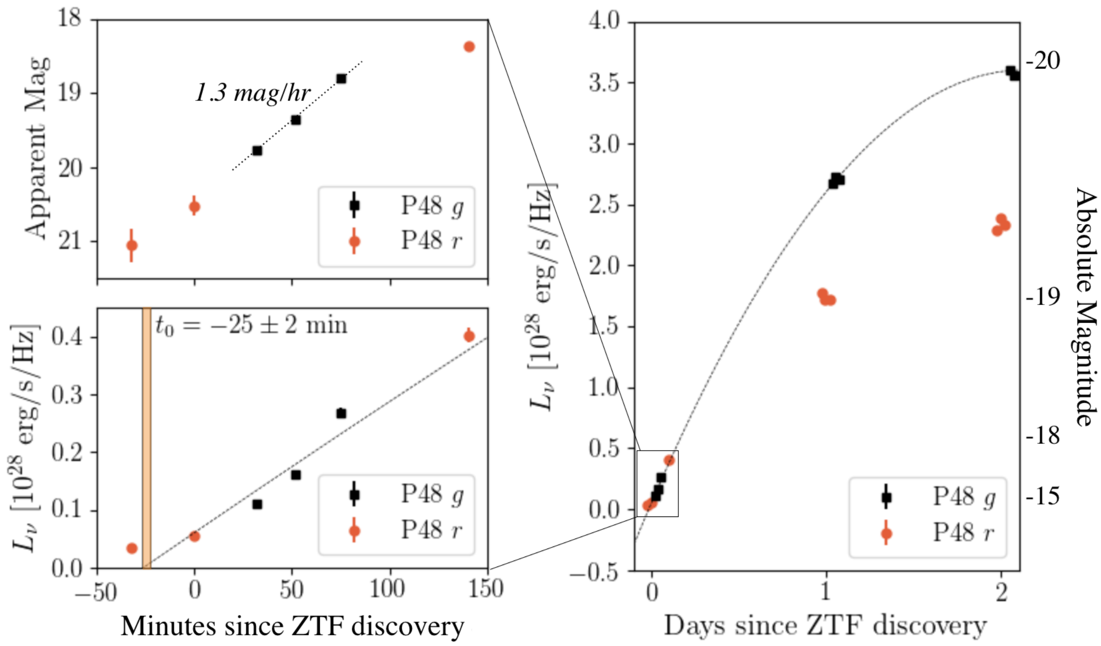

Figure 2. The rapid rise in the first few minutes and first few days after the ZTF discovery of SN2018gep. We also show an r-band point from prior to discovery that was found in retrospect by lowering the detection threshold from 5-σ to 3-σ. Top left: the rise in magnitudes gives an almost unprecedented rate of $1.3\,\mathrm{mag\,hr^{-1}}$. Bottom left: the rise in flux space together with the quadratic fit and definition of t_0. Right: the rise in flux space showing the quadratic fit.

To establish a reference epoch, we fit a second-order polynomial to the first three days of the g-band light curve in flux space, and define t_0 as the time at which the flux is zero. This gives t_0 as being 25 ± 2 minutes prior to the first detection, or $t_0 \approx$ UTC 2018-09-09 03:30. Note that this time is after the first r-band detection. In flux space, the light curve seems to flatten out at early times, which can be seen in the bottom-left panel of Figure 2). We revisit this flattening and the physical interpretation of t_0 in Section 4.2.

We announced the discovery and fast rise via the Astronomer's Telegram (Ho et al. 2018b), and the transient was given the IAU name SN2018gep. Motivated by the rapid rise to high luminosity, we triggered ultraviolet (UV) and optical observations with the UV/Optical Telescope (UVOT; Roming et al. 2005) aboard the *Neil Gehrels Swift Observatory* (Gehrels et al. 2004), and observations began 10.2 hours after the

ZTF discovery (Schulze et al. 2018a). A search of IceCube data found no temporally coincident high-energy neutrinos (Blaufuss 2018).

2.2. *Photometry*

From $\Delta t \approx 1$ day to $\Delta t \approx 60$ day, we conducted a photometric follow-up campaign at UV and optical wavelengths using *Swift*/UVOT, the Spectral Energy Distribution Machine (SEDM; Blagorodnova et al. 2018) mounted on the automated 60-inch telescope at Palomar (P60; Cenko et al. 2006), the optical imager (IO:O) on the Liverpool Telescope (LT; Steele et al. 2004), and the Lulin 1-m Telescope (LOT).

Basic reductions for the LT IO:O imaging were performed by the LT pipeline[1]. Digital image subtraction and photometry for the SEDM, LT and LOT imaging was performed using the Fremling Automated Pipeline (`FPipe`; Fremling et al. 2016). `Fpipe` performs calibration and host subtraction against Sloan Digital Sky Survey reference images and catalogs (SDSS; Ahn et al. 2014).

The UVOT data were retrieved from the NASA *Swift* Data Archive[2] and reduced using standard software distributed with HEASOFT version 6.19[3]. Photometry was measured using UVOTMAGHIST with a $3''$ circular aperture. To remove the host contribution, we obtained a final epoch in all broad-band filters on 18 October 2018 and built a host template using UVOTIMSUM and UVOTSOURCE with the same aperture used for the transient.

Figure 3 shows the full set of light curves. The photometry is listed in Table 5 in Appendix A. In Figure 4 we compare the rise time and peak absolute magnitude to other rapidly evolving transients from the literature.

2.3. *Spectroscopy*

The first spectrum was taken 0.7 day after discovery by the Spectrograph for the Rapid Acquisition of Transients (SPRAT; Piascik et al. 2014) on the Liverpool Telescope (LT). The spectrum showed a blue continuum with narrow galaxy emission lines, establishing this as a luminous transient ($M_{\rm g,peak} = -19.7$). Twenty-three optical spectra were obtained from +0.7 day until +61.1 day, using SPRAT, the Andalusia Faint Object Spectrograph and Camera (ALFOSC) on the Nordic Optical Telescope (NOT), the Double Spectrograph (DBSP; Oke & Gunn 1982) on the 200-inch Hale telescope at Palomar Observatory, the Low Resolution Imaging Spectrometer (Oke et al. 1995) on the Keck I 10-m telescope, and the Xinglong 2.16-m telescope (XLT+BFOSC) of NAOC, China (Wang et al. 2018). As discussed in Section 3.2, the early $\Delta t < 5$ day spectra show broad absorption features that evolve redward with time, which we attribute to carbon and oxygen. By $\Delta t \sim 8$ day, the spectrum resembles a stripped-envelope SN, and the usual broad features of a Ic-BL emerge (Costantin et al. 2018).

[1] https://telescope.livjm.ac.uk/TelInst/Pipelines/#ioo
[2] https://heasarc.gsfc.nasa.gov/cgi-bin/W3Browse/swift.pl
[3] https://heasarc.nasa.gov/lheasoft/

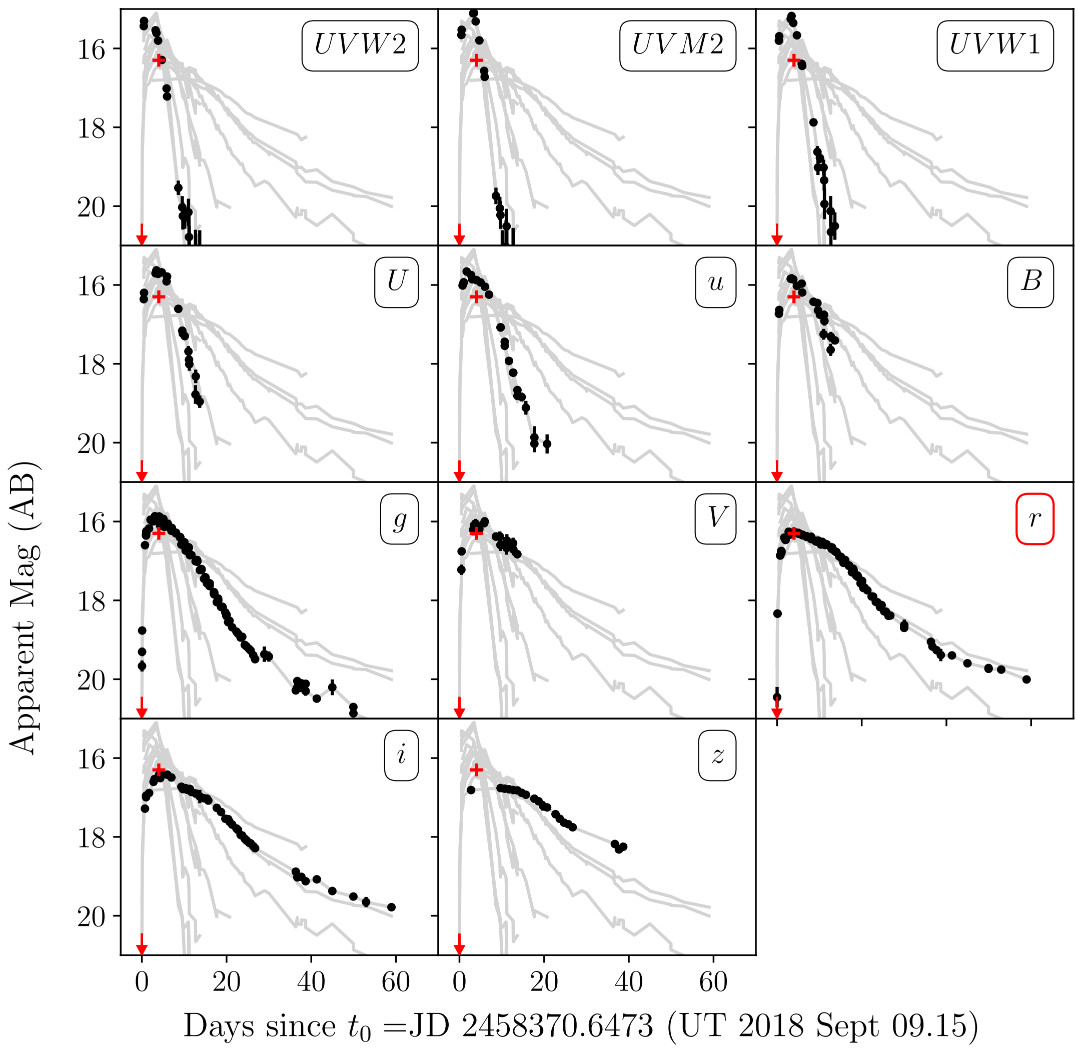

Figure 3. UV and optical light curves from *Swift* and ground-based facilities. The arrow marks the last non-detection, which was in r-band. The red cross marks the peak of the r-band light curve, which is 16.3 mag at $\Delta t = 4$ day. The full set of light curves are shown as grey lines in the background, and each panel highlights an individual filter in black. We correct for Galactic extinction using the attenuation curve from Fitzpatrick (1999) and $E_{B-V} = R_V/A_V = 0.01$ for $R_V = 3.1$ and $A_V = 0.029$ (Schlafly & Finkbeiner 2011).

We use the automated LT pipeline reduction and extraction for the LT spectra. LRIS spectra were reduced and extracted using `Lpipe` (Perley 2019b). The NOT spectrum was obtained at parallactic angle using a 1″ slit, and was reduced in a standard way, including wavelength calibration against an arc lamp, and flux calibration using a spectrophotometric standard star. The XLT+BFOSC spectra were reduced using the standard IRAF routines, which involves corrections for bias, flat field, and

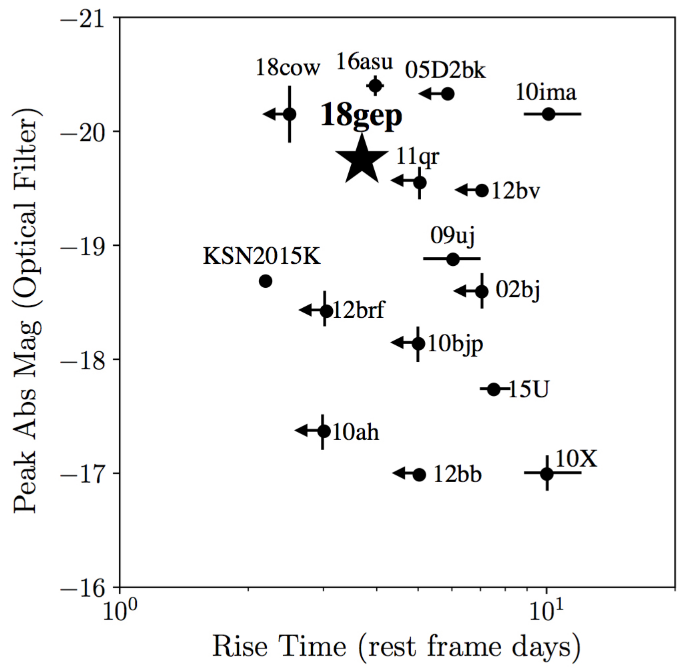

Figure 4. The phase space of rise time vs. peak absolute magnitude at optical wavelengths, adapted from Figure 4 of Rest et al. (2018). For KSN2015K, the uncertainty in the observed band is smaller than the symbol size. However, because there were observations in only one filter, there is some additional uncertainty that is not being shown. the time from t_0 to peak is 3 day in g-band ($M_{g,\mathrm{pk}} = -19.9$) and 4 day in r-band ($M_{r,\mathrm{pk}} = -19.5$). For iPTF16asu, the best-fit rise time (time from best-fit explosion time to peak g-band magnitude) is 3.97 ± 0.19 day (Whitesides et al. 2017). For AT2018cow, there was only one detection prior to optical peak, so the rise time of 2.5 day in g-band is an upper limit. The peak luminosity is $M_{g,\mathrm{pk}} = -20.4$ and $M_{r,\mathrm{pk}} = -19.9$ (Perley et al. 2019a).

removal of cosmic rays. The Fe/Ar and Fe/Ne arc lamp spectra obtained during the observation night are used to calibrate the wavelength of the spectra, and the standard stars observed on the same night at similar airmasses as the supernova were used to calibrate the flux of spectra. The spectra were further corrected for continuum atmospheric extinction during flux calibration, using mean extinction curves obtained at Xinglong Observatory. Furthermore, telluric lines were removed from the data.

The *Swift* grism data were processed using the calibration and software described by Kuin et al. (2015). During the observation, the source spectrum was centered on the detector, which is the default location for *Swift*/UVOT observations. Because of this, there is second-order contamination from a nearby star, which was reduced by using a narrow extraction width (1.3″ instead of 2.5″). The contamination renders the spectrum unreliable at wavelengths longer than 4100 Å, but is negligible in the range 2850–4100 Ådue to absorption from the ISM. Below 2200 Å, the spectrum overlaps with the spectrum from another star in the field of view.

See Appendix B for a spectral log, as well as a figure showing the full spectral evolution. In Section 3.2 we present an overview of the spectral evolution, and interpret the feature in the early spectra, including the grism spectrum.

2.4. *Search for pre-explosion outbursts*

We performed forced photometry using the PSF-fitting code of Yao et al. (in prep) at the position of SN2018gep on single-epoch difference images produced by the IPAC ZTF difference imaging pipeline. We loaded this photometry into a local instance of SkyPortal (van der Walt et al. 2019), an open-source web application that interactively displays astronomical datasets for annotation, analysis, and discovery.

Deep difference images were obtained by subtracting long-baseline references from 1-to-3 day stacks of ZTF science images. The reference images were generated by performing an inverse-variance weighted coaddition of 298 R-band and 69 g-band images from PTF/iPTF taken between 2009 and 2016 using the `CLIPPED` combine strategy in `SWarp` (Bertin 2010; Gruen et al. 2014). PTF/iPTF images were used instead of ZTF images to build references as they were taken years earlier and were thus less likely to contain any transient flux. No cross-instrument corrections were applied to the references prior to subtraction. Pronounced regions of negative flux on the PTF/iPTF references caused by crosstalk from bright stars were masked out manually.

Next, ZTF science images taken between 2018 Feb 22 and 2018 Aug 31 were stacked in a rolling window (segregated by filter) with a width of 3 days and a period of 1 day, also using the `CLIPPED` technique in `SWarp`. Images taken between 2018 Sep 01 and t_0 were stacked in a window with a width of 1 day and a period of 1 day. Subtractions were obtained using the `HOTPANTS` (Becker 2015) implementation of the Alard & Lupton (1999) PSF matching algorithm. Many of the ZTF science images during this period were obtained under exceptional conditions, and the seeing on the ZTF science coadds was often significantly better than the seeing on the PTF/iPTF references. To correct for this effect, ZTF science coadds were convolved with their own point spread functions (PSFs), extracted using `PSFEx`, prior to subtraction. During subtraction, PSF matching and convolution were performed on the template and the resulting subtractions were normalized to the photometric system of the science images. We show two example subtractions in Figure 5.

PSF photometry was performed at the location of SN2018gep on the subtractions using the PSF of the science images. To estimate the uncertainty on the flux measurements made on these subtractions, we employed a Monte Carlo technique, in which thousands of PSF fluxes were measured at random locations on the image, and the PSF-flux uncertainty was taken to be the 1σ dispersion in these measurements.

We detected significant flux excesses at the location of SN2018gep in both g and r bands in the weeks preceding its first detection in single-epoch ZTF subtractions (at $t = t_0$). We show these measurements in Figure 6. The effective dates are determined by taking an inverse-flux variance weighted average of the input image dates. The detections in the week leading up to explosion are $m_g \sim m_r \approx 22$, which is approximately the magnitude limit of the coadd subtractions. However, in an r-band

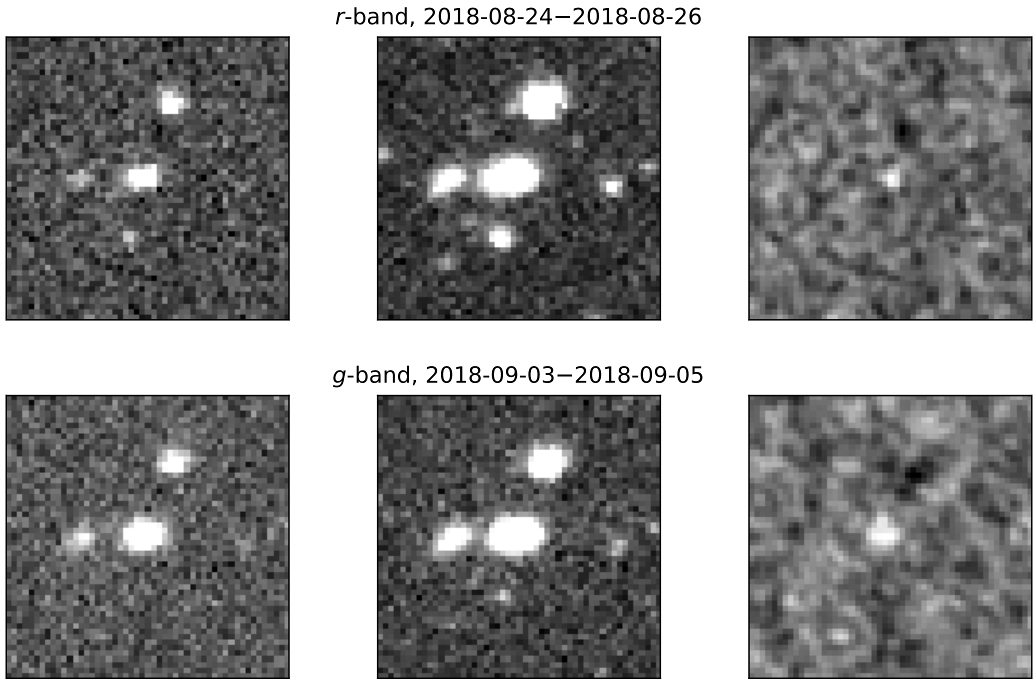

Figure 5. Sample pre-explosion subtractions of deep PTF/iPTF references from ZTF science images stacked in 3-day bins (see Section 2.4). Each cutout is centered on the location of SN2018gep. The subtractions show clear emission at the location of the SN in both g and r-bands days to weeks before the discovery of the SN in ZTF.

stack of images from August 24–26 (inclusive), we detect emission at $m_r \sim 21.5$ at 5σ above the background.

It is unlikely that this variability arises from AGN activity. In Section 3.3 we infer a low host mass of $\log M/M_\odot \approx 8.11\, M_\odot$. We also show that the position in the BPT diagram is unlike AGN (Figure 16).

There was a tentative detection of pre-explosion emission in the Ic-BL SN PTF 11qcj (Corsi et al. 2014), and Corsi et al. (2014) suggested that precursor eruptions may be a feature characterizing the final pre-explosion evolution of Ic-BL SNe. In that case, the detections were 1.5 years and 2.5 years prior to the discovery of the SN. Unlike SN2018gep, however, PTF 11qcj was characterized by a high radio luminosity, suggesting a more extended dense CSM.

Figure 6 shows the full g and r-band light curves, including the measurements of precursor emission. We also show the timeline of the first two days of follow-up. In future work we will extend the precursor light curve and explore the more extensive history of progenitor activity.

2.5. *Radio follow-up*

We observed the field of SN2018gep with the Karl G. Jansky Very Large Array (VLA) on three epochs: on September 14 under the Program ID VLA/18A-242 (PI: D. Perley; Ho et al. 2018c), and on 2018 September 25 and 2018 November 23 under

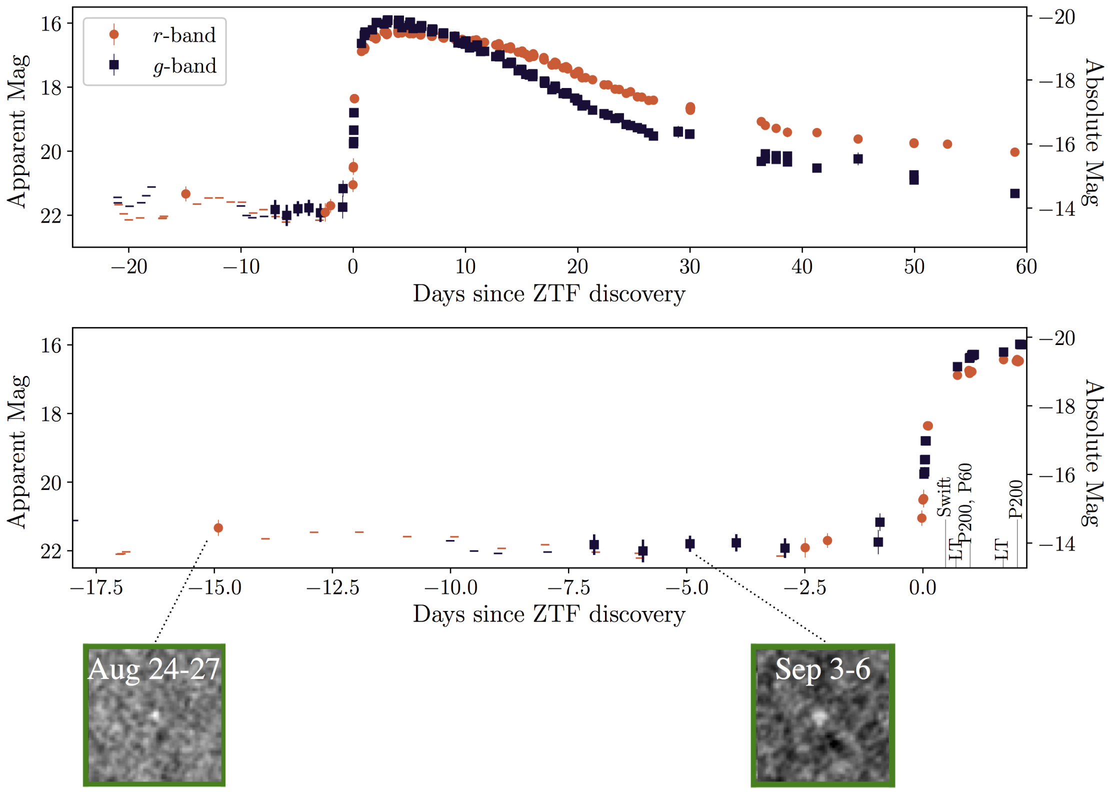

Figure 6. Full r and g-band light curves of SN2018gep. 3-σ upper limits are shown as horizontal lines. Points at $t < 0$ are from 3-day stacks of ZTF/P48 data as described in Section 2.4. Sample subtractions from two of these stacks are shown in the bottom row.

the Program ID VLA/18A-176 (PI: A. Corsi). We used 3C286 for flux calibration, and J1640+3946 for gain calibration. The observations were carried out in X- and Ku-band (nominal central frequencies of 9 GHz and 14 GHz, respectively) with a nominal bandwidth of 2 GHz. The data were calibrated using the automated VLA calibration pipeline available in the CASA package (McMullin et al. 2007) then inspected for further flagging. The CLEAN procedure (Högbom 1974) was used to form images in interactive mode. The image rms and the radio flux at the location of SN2018gep were measured using `imstat` in CASA. Specifically, we report the maximum flux within pixels contained in a circular region centered on the optical position of SN2018gep with radius comparable to the FWHM of the VLA synthesized beam at the appropriate frequency. The source was detected in the first two epochs, but not in the third (see Table 1). As we discuss in Section 4, the first two epochs were conducted in a different array configuration than the third epoch, and may have had a contribution from host galaxy light.

Radio observations of the field of SN2018gep were conducted using the AMI large array (AMI-LA; Zwart et al. 2008; Hickish et al. 2018). AMI-LA is a radio interferometer comprised of eight, 12.8-m in diameter, antennas producing 28 baselines which extends from 18-m up to 110-m in length and operates with a 5 GHz bandwidth around a central frequency of 15.5 GHz. The first AMI-LA observations of SN2018gep occurred on September 12 and 23, 2018, about three and fourteen days after optical detection, four hours each. Another four-hour observation took place on October 20, 2018.

Initial data reduction, flagging and calibration of the phase and flux, was carried out using `reduce_dc`, a customized AMI data reduction software package (e.g. Perrott et al. 2013). Phase calibration was conducted using short interleaved observations of J1646+4059, while for absolute flux calibration we used 3C286. Additional flagging and imaging were preformed using CASA. All three observations resulted in null-detections with 3-σ upper limits of $\approx 120\,\mu$Jy in the first two observations, and a 3-σ upper limit of $\approx 120\,\mu$Jy in the last observation.

SN2018gep was observed with the Submillimeter Array (SMA; Ho et al. 2004) on UT 2018 Sep 15 under its target-of-opportunity program. The project ID was 2018A-S068. Observations were performed in the sub-compact configuration using seven antennas. The observations were performed using RxA and RxB receivers tuned to LO frequencies of 225.55 GHz and 233.55 GHz respectively, providing 32 GHz of continuous bandwidth ranging from 213.55 GHz to 245.55 GHz with a spectral resolution of 140.0 kHz per channel. The atmospheric opacity was around 0.16-0.19 with system temperatures around 100-200 K. The nearby quasars 1635+381 and 3C345 were used as the primary phase and amplitude gain calibrators with absolute flux calibration performed by comparison to Neptune. Passband calibration was derived using 3C454.3. Data calibration was performed using the MIR IDL package for the SMA, with subsequent analysis performed in MIRIAD (Sault et al. 1995). For the flux measurements, all spectral channels were averaged together into a single continuum channel and an rms of 0.6 mJy was achieved after just 75 minutes on-source. The full set of radio measurements are listed in Table 1.

Table 1. Radio flux density measurements for SN2018gep.

Start Time (UTC)	Δt (days)	Instrument	ν (GHz)	f_ν (μJy)	L_ν ($\mathrm{erg\,s^{-1}\,Hz^{-1}}$)	θ_{FWHM} $''$	Int. time (hr)
2018-09-12 17:54	3.6	AMI	15	<120	$<2.9\times10^{27}$	43.53×30.85	4
2018-09-23 15:35	14.5	AMI	15	<120	$<2.9\times10^{27}$	39.3×29.29	4
2018-10-20 14:01	41.4	AMI	15	<120	$<2.9\times10^{27}$	43.53×30.85	4
2018-09-15 02:33	6.0	SMA	230	<590	$<1.4\times10^{28}$	4.828×3.920	1.25
2018-09-14 01:14	4.9	VLA	9.7	34 ± 4	8.3×10^{26}	7.06×5.92	0.5
2018-09-25 00:40	15.9	VLA	9	24.4 ± 6.8	6.0×10^{26}	7.91×6.89	0.7
2018-09-25 00:40	15.9	VLA	14	26.8 ± 6.8	6.6×10^{26}	4.73×4.26	0.5
2018-11-23 13:30	75.4	VLA	9	<16	$<3.9\times10^{26}$	3.52×2.08	0.65
2018-11-23 13:30	75.4	VLA	14	<17	$<4.2\times10^{26}$	2.77×1.32	0.65

Note—For VLA measurements: The quoted errors are calculated as the quadrature sums of the image rms, plus a 5% nominal absolute flux calibration uncertainty. When the peak flux density within the circular region is less than three times the RMS, we report an upper limit equal to three times the RMS of the image. For AMI measurements: non-detections are reported as 3-σ upper limits. For SMA measurements: non-detections are reported as a 1-σ upper limit.

2.6. *X-ray follow-up*

We observed the position of SN2018gep with *Swift*/XRT from $\Delta t \approx 0.4$ day to $\Delta t \approx 14$ day. We downloaded the *Swift*/XRT data products using web-based tools developed by the *Swift*-XRT team (Evans et al. 2009), using the default values. The source was not detected in any epoch. For the first epoch, the 3-σ upper limit was 0.003 ct/s. To convert the upper limit from count rate to flux, we assumed[4] a Galactic neutral hydrogen column density of $1.3 \times 10^{20}\,\mathrm{cm}^{-2}$, and a power-law spectrum with photon index $\Gamma = 2$. This gives[5] an unabsorbed 0.3–10 keV flux of $< 9.9 \times 10^{-14}\,\mathrm{erg\,cm^{-2}\,s^{-1}}$, and $L_X < 2.5 \times 10^{41}\,\mathrm{erg\,s^{-1}}$.

We obtained two epochs of observations with the Advanced CCD Imaging Spectrometer (ACIS; Garmire et al. 2003) on the *Chandra* X-ray Observatory via our approved program (Proposal No. 19500451; PI: Corsi). The first epoch began at 9:25 UTC on 10 October 2018 ($\Delta t \approx 15$ day) under ObsId 20319 (integration time 12.2 ks), and the second began at 21:31 UTC on 4 December 2018 ($\Delta t \approx 70$ day) under ObsId 20320 (integration time 12.1 ks). No X-ray emission is detected at the location of SN2018gep in either epoch, with a 90% upper limit on the 0.5–7.0 keV count rate of $\approx 2.7 \times 10^{-4}\,\mathrm{ct\,s^{-1}}$ in both epochs. Using the same values of hydrogen column density and power-law photon index as in our XRT measurements, we find upper limits on the unabsorbed 0.5–7 keV X-ray flux of $< 3.2 \times 10^{-15}\,\mathrm{erg\,cm^{-2}\,s^{-1}}$, or (for a direct comparison to the XRT band) a 0.3–10 keV X-ray flux of $< 4.2 \times 10^{-15}\,\mathrm{erg\,cm^{-2}\,s^{-1}}$. This corresponds to a 0.3–10 keV luminosity upper limit of $L_X < 1.0 \times 10^{40}\,\mathrm{erg\,s^{-1}}$.

2.7. *Search for prompt gamma-ray emission*

We searched the *Fermi*-GBM online GRB catalog[6] (Gruber et al. 2014; von Kienlin et al. 2014; Narayana Bhat et al. 2016) and the INTEGRAL SPI-ACS online GRB catalog[7] (Mereghetti et al. 2003) but did not find any gamma-ray burst (GRB) consistent with the position and t_0 of SN2018gep.

By searching the spacecraft pointing history we find that at t_0 SN2018gep was visible to the *Swift* Burst Alert Telescope (BAT; Barthelmy et al. 2005). More precisely, the position was in the BAT field-of-view from UTC 03:13:40 to 03:30:38, and then *Swift* slewed to another location. The code to search the *Swift* pointing history is publicly available on Github[8].

At t_0 SN2018gep was also visible to the *Fermi* Gamma-Ray Burst Monitor (GBM; Meegan et al. 2009). We ran a targeted GRB search in 10–1000 keV *Fermi*/GBM data from three hours prior to t_0 to half an hour after t_0. We use the soft template, which is a smoothly broken power law with low-energy index -1.9 and high-energy index -2.7, and an SED peak at 70 keV. The search methodology (and parameters of the other templates) are described in Blackburn et al. (2015) and Goldstein et al.

[4] https://heasarc.gsfc.nasa.gov/cgi-bin/Tools/w3nh/w3nh.pl
[5] https://heasarc.gsfc.nasa.gov/cgi-bin/Tools/w3pimms/w3pimms.pl
[6] https://heasarc.gsfc.nasa.gov/W3Browse/fermi/fermigbrst.html
[7] https://www.isdc.unige.ch/integral/science/grb
[8] https://github.com/lanl/swiftbat_python.

(2016). No signals with a consistent location were found. For the 100 s integration time, the fluence upper limit is 2×10^{-6} erg cm^{-2}. This limit corresponds to a 10–1000 keV isotropic energy release of $E_{\gamma,\mathrm{iso}} < 4.9 \times 10^{48}$ erg. Limits for different spectral templates and integration times are shown in Figure 7.

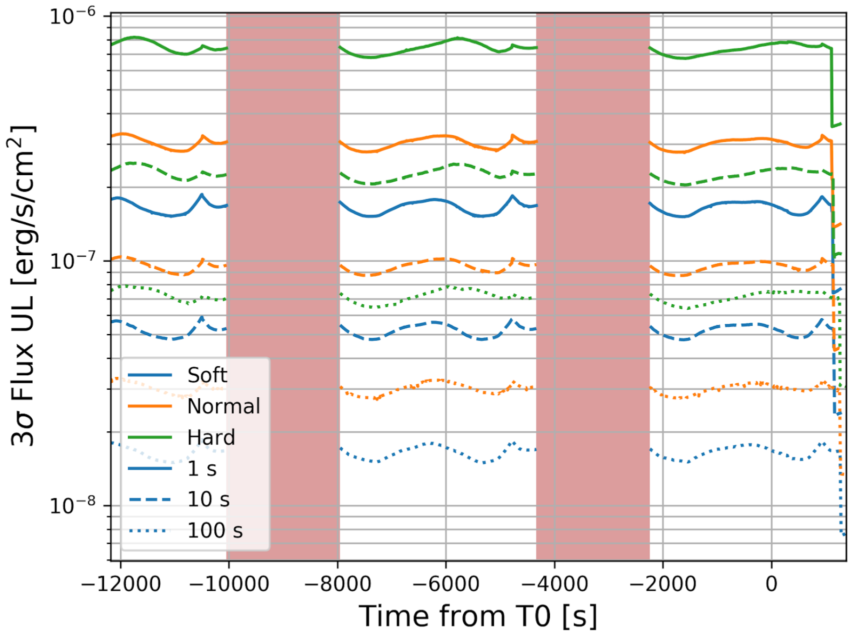

Figure 7. 3-σ upper limits from GBM GRB search, which we performed for three hours prior to t_0. The red vertical bars indicate epochs when GBM was not taking data due to passing through the South Atlantic Anomaly. The time of t_0 was estimated from a fit to the early data (Figure 6), and is 26 ± 5 minutes prior to the first detection.

2.8. *Host galaxy data*

We measure line fluxes using the Keck optical spectrum obtained at $\Delta t \approx 61$ day (Figure 25). We model the local continuum with a low-order polynomial and each emission line by a Gaussian profile of FHWM ~ 5.3 Å. This is appropriate if Balmer absorption is negligible, which is generally the case for starburst galaxies. For the host of SN2018gep, the Balmer decrement between Hβ, Hγ and Hδ does not show any excess with respect to the expected values in Osterbrock & Ferland (2006). The resulting line fluxes are listed in Table 7.

We retrieved archival images of the host galaxy from *Galaxy Evolution Explorer* (*GALEX*) Data Release (DR) 8/9 (Martin et al. 2005), Sloan Digital Sky Survey (SDSS) DR9 (Ahn et al. 2012), Panoramic Survey Telescope And Rapid Response System (PanSTARRS, PS1) DR1 (Chambers et al. 2016), Two-Micron All Sky Survey (2MASS; Skrutskie et al. 2006), and *Wide-Field Infrared Survey Explorer* (*WISE*; Wright et al. 2010). We also used UVOT photometry from *Swift*, and NIR photometry from the Canada-France-Hawaii Telescope Legacy Survey (CFHTLS; Hudelot et al. 2012).

The images are characterized by different pixel scales (e.g., SDSS 0.″40/px, GALEX 1.″/px) and different point spread functions (e.g., SDSS/PS1 1–2″, *WISE*/W2 6.″5). To obtain accurate photometry, we use the matched-aperture photometry software package Lambda Adaptive Multi-Band Deblending Algorithm in R (LAMBDAR; Wright et al. 2016) that is based a photometry software package developed by Bourne et al. (2012). To measure the total flux of the host galaxy, we defined an elliptical aperture that encircles the entire galaxy in the SDSS/r'-band image. This aperture was then convolved in LAMBDAR with the point-spread function of a given image that we specified directly (*GALEX* and *WISE* data) or that we approximated by a two-dimensional Gaussian (2MASS, SDSS and PS1 images). After instrumental magnitudes were measured, we calibrated the photometry against instrument-specific zeropoints (*GALEX*, SDSS and PS1 data), or as in the case of 2MASS and *WISE* images against a local sequence of stars from the 2MASS Point Source Catalogue and the AllWISE catalogue. The photometry from the UVOT images were extracted with the command uvotsource in HEAsoft and a circular aperture with a radius of 8″. The photometry of the CFHT/WIRCAM data was done performed the software tool presented in Schulze et al. (2018b)[9]. To convert the 2MASS, UVOT, WIRCAM and *WISE* photometry to the AB system, we applied the offsets reported in Blanton, & Roweis (2007), Breeveld et al. (2011) and Cutri et al. (2013). The resulting photometry is summarized in Table 8.

3. BASIC PROPERTIES OF THE EXPLOSION AND ITS HOST GALAXY

The observations we presented in Section 2 constitute some of the most detailed early-time observations of a stripped-envelope SN to date, as well as the first definitive detection of a precursor activity in a Ic-BL. In this section we use this data to derive basic properties of the explosion: the evolution of bolometric luminosity, radius, and effective temperature over time (Section 3.1), the evolution of velocity as measured from the spectra (Section 3.2), and the mass, metallicity, and SFR of the host galaxy (Section 3.3).

3.1. *Physical evolution from blackbody fits*

By interpolating the UVOT and ground-based photometry onto common epochs, we construct multi-band SEDs and fit a Planck function at the redshift of SN2018gep on each epoch. To estimate the uncertainties, we perform a Monte Carlo simulation with 600 trials, each time adding noise corresponding to a 15% systematic uncertainty on each data point, motivated by the need to obtain a combined χ^2/dof ~ 1 across all epochs. The uncertainties for each parameter are taken as the 16-to-84 percentile range from this simulation. The SED fits are shown in Appendix A, and the resulting

[9] https://github.com/steveschulze/aperture_photometry

Table 2. Physical evolution of AT2018gep from blackbody fits.

Δt	$L(10^{10}L_\odot)$	R (AU)	T (kK)
0.05	$0.04^{+0.04}_{-0.02}$	21^{+14}_{-6}	13^{+5}_{-4}
0.48	$7.4^{+8.6}_{-4.1}$	22^{+7}_{-5}	46^{+16}_{-13}
0.73	$4.5^{+5.5}_{-2.8}$	31^{+11}_{-6}	35^{+12}_{-11}
1.0	$2.2^{+2.1}_{-1.2}$	46^{+18}_{-9}	24^{+6}_{-6}
1.7	$3.5^{+4.2}_{-2.1}$	46^{+22}_{-10}	27^{+9}_{-8}
2.7	$1.3^{+1.2}_{-0.4}$	78^{+22}_{-20}	16^{+5}_{-3}
3.2	$3.5^{+2.2}_{-1.3}$	50^{+14}_{-8}	26^{+6}_{-5}
3.8	$2.9^{+1.7}_{-0.8}$	56^{+11}_{-11}	23^{+5}_{-3}
4.7	$1.7^{+0.7}_{-0.3}$	69^{+16}_{-14}	18^{+3}_{-2}
5.9	$0.88^{+0.17}_{-0.08}$	100^{+14}_{-21}	13^{+1}_{-0}
8.6	$0.46^{+0.08}_{-0.06}$	220^{+46}_{-39}	$7.4^{+0.6}_{-0.5}$
9.6	$0.33^{+0.04}_{-0.03}$	200^{+33}_{-24}	$7.1^{+0.4}_{-0.4}$
10.0	$0.31^{+0.04}_{-0.03}$	210^{+34}_{-28}	$6.9^{+0.4}_{-0.4}$
11.0	$0.28^{+0.04}_{-0.03}$	220^{+35}_{-33}	$6.5^{+0.4}_{-0.3}$
13.0	$0.25^{+0.04}_{-0.03}$	260^{+50}_{-42}	$5.8^{+0.3}_{-0.3}$
14.0	$0.22^{+0.04}_{-0.03}$	270^{+60}_{-47}	$5.5^{+0.4}_{-0.3}$
16.0	$0.17^{+0.04}_{-0.03}$	260^{+76}_{-58}	$5.3^{+0.5}_{-0.5}$
18.0	$0.15^{+0.04}_{-0.02}$	300^{+77}_{-64}	$4.7^{+0.4}_{-0.4}$
21.0	$0.11^{+0.03}_{-0.02}$	250^{+83}_{-58}	$4.7^{+0.4}_{-0.4}$
25.0	$0.073^{+0.02}_{-0.013}$	240^{+95}_{-85}	$4.5^{+0.9}_{-0.5}$
38.0	$0.034^{+0.012}_{-0.007}$	180^{+86}_{-55}	$4.2^{+0.6}_{-0.5}$

evolution in bolometric luminosity, photospheric radius, and effective temperature is listed in Table 2 and shown in Figure 8.

The bolometric luminosity peaks between $\Delta t = 0.5$ day and $\Delta t = 3$ day, at $> 3\times10^{44}\,\mathrm{erg\,s^{-1}}$. As in iPTF16asu, it falls as an exponential at late times ($t > 10$ day). The total integrated UV and optical ($\approx$ 2000–9000Å) blackbody energy output from $\Delta t = 0.5$–40 day is $\sim 10^{50}$ erg, similar to that of iPTF16asu. The earliest photospheric radius we measure is $\sim$ 20 AU, at $\Delta t = 0.05$ day. Until $\Delta t \approx 17$ day the radius expands over time with a very large inferred velocity of $v \approx 0.1c$. After that, it remains flat, and even appears to recede. This possible recession corresponds to a flattening in the temperature at $\sim$ 5000 K, which is the recombination temperature of carbon and oxygen. This effect was not seen in iPTF16asu, which remains hotter (and more luminous) for longer. Finally, the effective temperature is seen to rise before falling as $\sim t^{-1}$. We discuss this rising temperature in the context of shock-cooling emission in Section 4.2.

3.2. *Spectral evolution and velocity measurements*

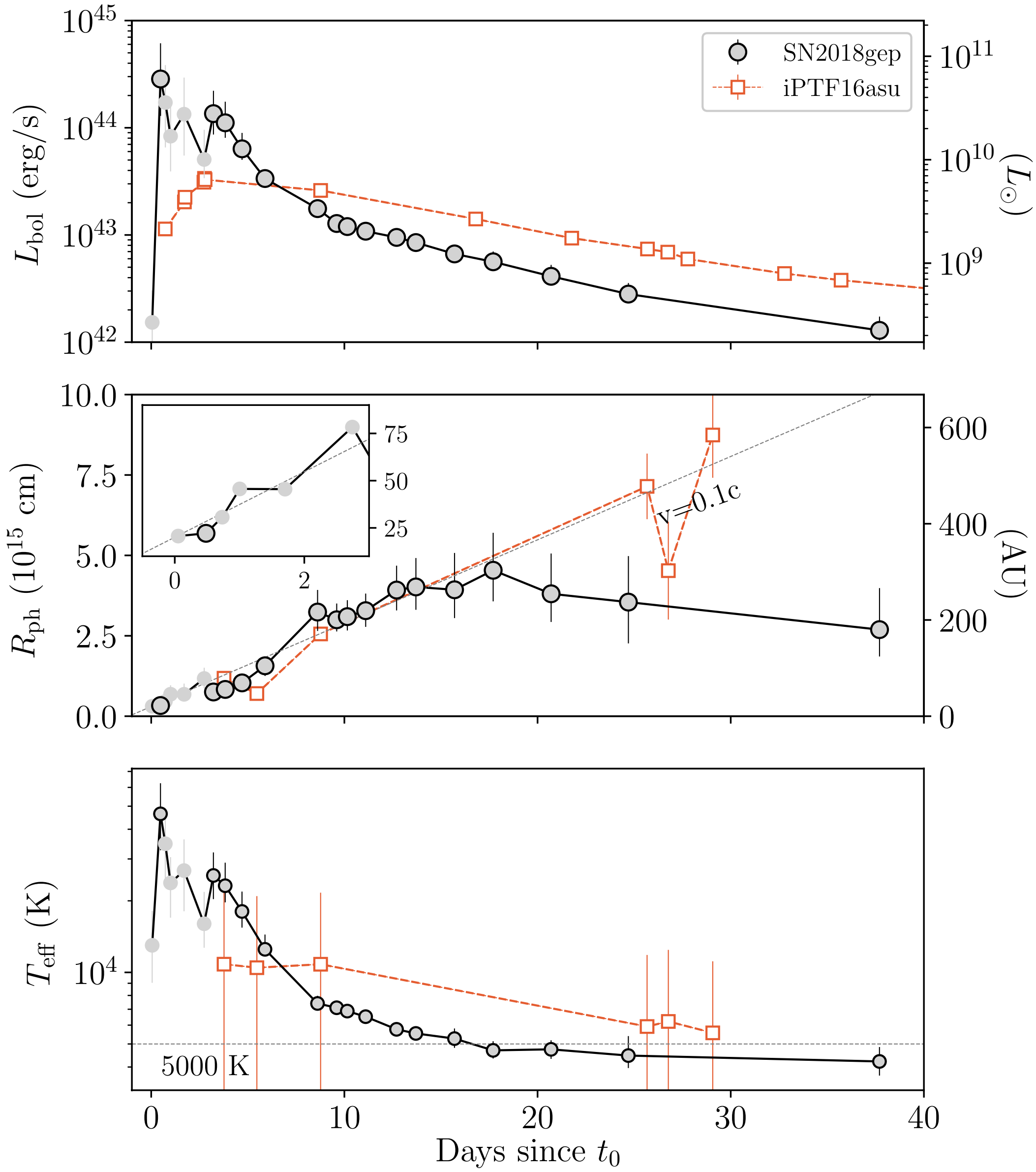

Figure 8. Evolution of blackbody properties (luminosity, radius, temperature) over time compared to the Ic-BL SN iPTF16asu. The light grey circles are derived from optical data only. The outlined circles are derived from UV and optical data. Middle panel: dotted line shows $v = 0.1c$. Note that $R \neq 0$ at t_0, and instead $R(t = 0) = 3 \times 10^{14}$ cm. Bottom panel: dotted horizontal line shows 5000 K, the recombination temperature for carbon and oxygen. Once this temperature is reached, the photosphere flattens out (and potentially begins to recede).

We obtained nine spectra of SN2018gep in the first five days after discovery. These early spectra are shown in Figure 10, when the effective temperature declined from 50,000 K to 20,000 K. To our knowledge, our early spectra have no analogs in the literature, in that there has never been a spectrum of a stripped-envelope SN at such a high temperature (excluding spectra during the afterglow phase of GRBs). As shown in the middle panel of Figure 10, the earliest spectra of PTF10vgv (Corsi et

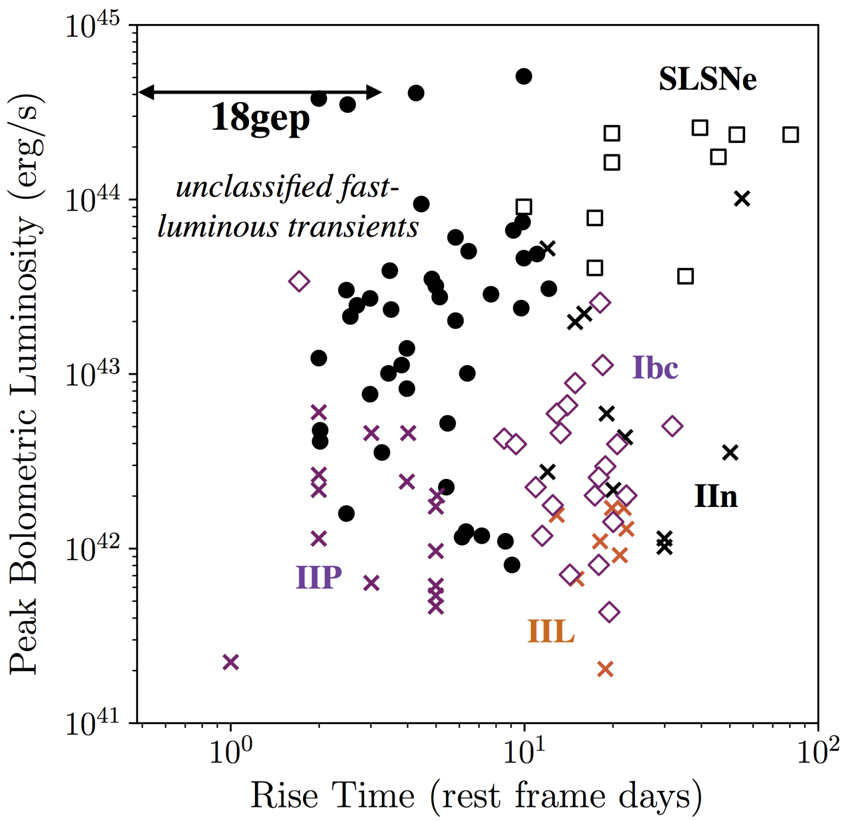

Figure 9. Rise to peak bolometric luminosity compared to other classes of transients. Modified from Figure 1 in Margutti et al. (2019).

al. 2012) and PTF12gzk (Ben-Ami et al. 2012), which were taken at $\Delta t = 2$ day and $\Delta t = 3$ day respectively, are redder and exhibit more features. There is however a spectrum of a Type II SN at a comparable temperature: iPTF13dqy was $\sim 50,000$ K at the time of the first spectrum (Yaron et al. 2017).

At $\Delta t \approx 4$ day, a "W" feature emerges in the wavelength range 3800–4350 Å (rest-frame). In the bottom panel of Figure 10 we make a comparison to "W" features seen in SN 2008D (e.g. Modjaz et al. 2009) and in typical pre-max stripped-envelope superluminous supernovae (Type I SLSNe; Moriya et al. 2018; Gal-Yam 2018). The absorption lines are broadened much more than in PTF12dam (Nicholl et al. 2013) and probably more than in SN2008D as well. Finally, SN2018gep cooled more slowly than SN 2008D: only after 4.25 days did it reach the temperature that SN 2008D reached after < 2 days.

The lack of comparison data at such early epochs (high temperatures) motivated us to model one of the early spectra. We use the spectral synthesis code JEKYLL (Ergon et al. 2018), configured to run in steady-state using a full NLTE-solution. An inner blackbody boundary was placed at an high continuum optical depth ($\sim$50), and the temperature at this boundary was iteratively determined to reproduce the observed luminosity. The atomic data used is based on what was specified in Ergon et al. (2018), but has been extended as described in Appendix C. We have explored models

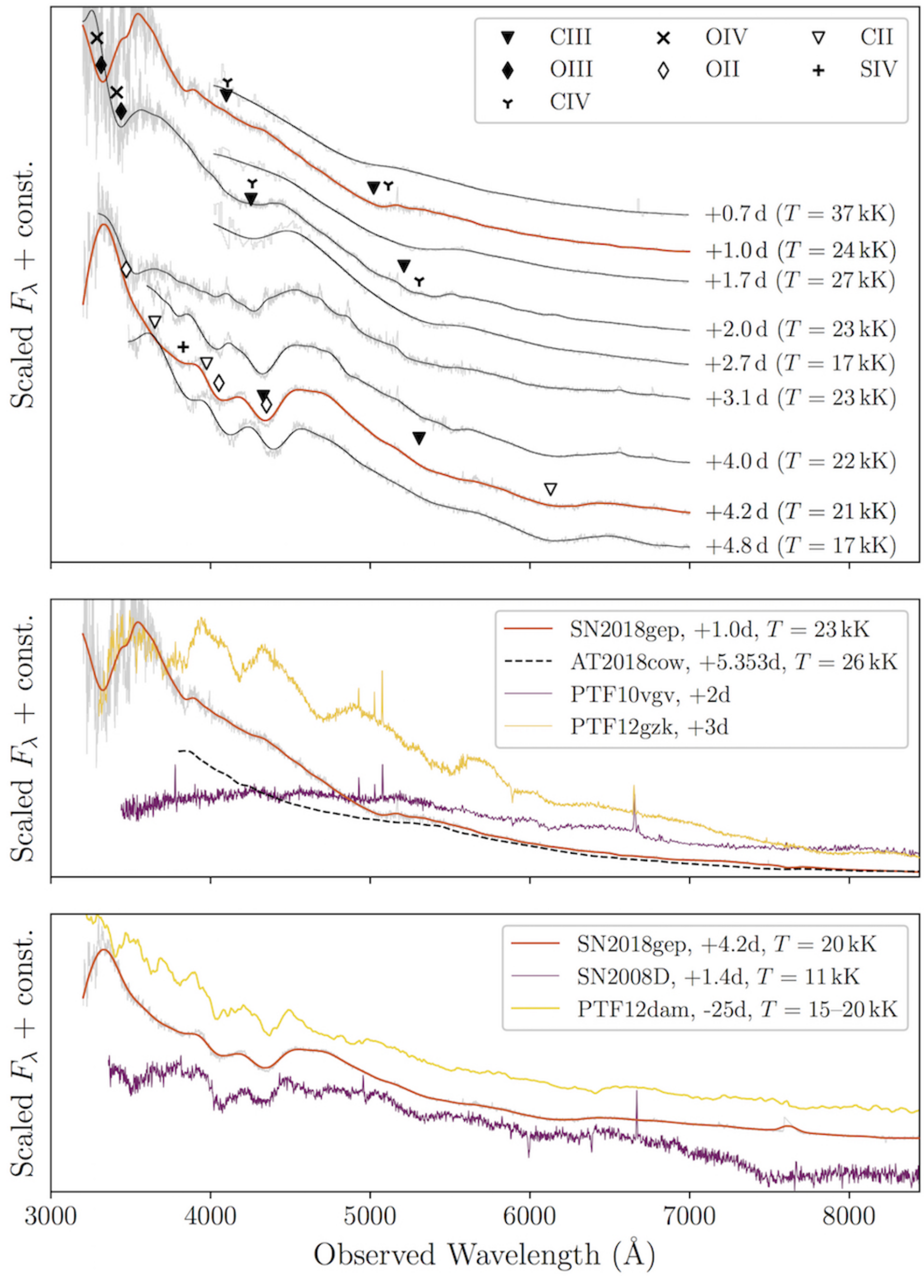

Figure 10. Top panel: spectra of SN2018gep taken in the first five days. Broad absorption features are consistent with ionized carbon and oxygen, which evolve redward with time. Bottom panel: The spectrum at $\Delta t = 4.2$ day shows a "W" feature, which we compare to similar "W" features seen in an early spectrum of SN2008D from Modjaz et al. (2009), and a typical pre-max spectrum of a SLSN-I (PTF12dam, from Nicholl et al. 2013). We boost the SLSN spectrum by an additional expansion velocity of $\sim 15000\,\mathrm{km\,s^{-1}}$, and apply reddening of $E(B-V) = 0.63$ to SN 2008D. Weak features in the red are also similar to what are seen in PTF12dam, and are consistent with arising from CII and CIII lines, following the analysis of Gal-Yam (2018). The lack of narrow carbon features as well as the smooth spectrum below 3700 Å suggest a large velocity dispersion leading to significant line broadening, compared to the intrinsically narrow features observed in SLSNe-I (Gal-Yam 2018; Quimby et al. 2018).

with C/O and O/Ne/Mg composition taken from a model by Woosley & Heger (2007) and a power-law density profile, where the density at the inner border was adjusted to fit the observed line velocities. Except for the density at the inner border, various power-law indices where also explored, but in the end an index close to the canonical value of −10 worked out best.

Figures 11 and 12 show the model with the best overall agreement with the spectra and the SED (as listed in Table 6 the spectrum was obtained at high airmass, making it difficult to correct for telluric features). The model has a C/O composition, an inner border at 22,000 km s^{-1} (corresponding to an optical depth of ∼50), a density of 4×10^{-12} g cm^{-3} at this border and a density profile with a power-law index of −9. In Figure 11 we show that the model does a good job of reproducing both the spectrum and the SED of SN2018gep. In particular, it is interesting to note that the "W" feature seem to arise naturally in C/O material at the observed conditions. A similar conclusion was reached by Dessart et al. (2018), whose magnetar-powered SLSN-I models, calculated using the NLTE code CMFGEN, show the "W" feature even when non-thermal processes where not included in the calculation (as in our case).

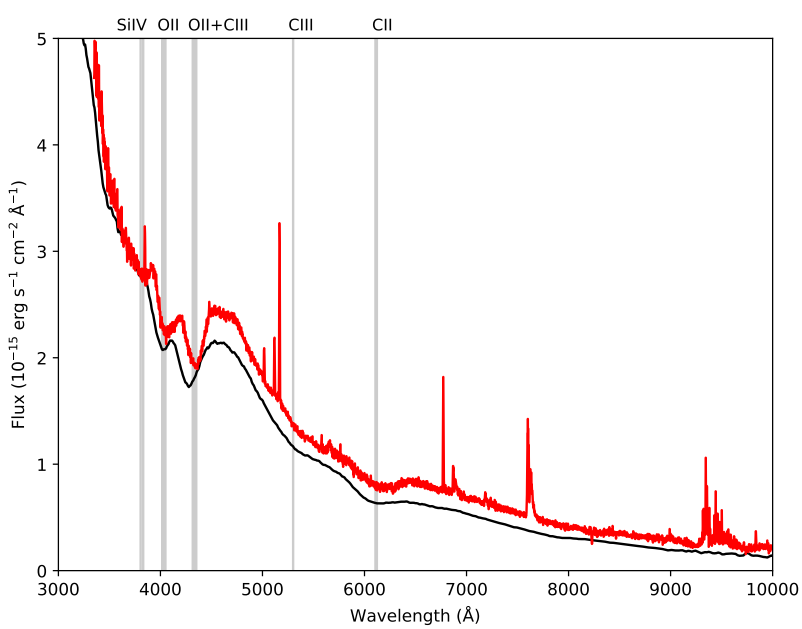

Figure 11. Observed spectrum (red) at 4.2 day, compared to our model spectrum (black) from the spectral synthesis code JEKYLL configured to run in steady-state using a full NLTE solution. The model has a C/O composition, an inner border at 22,000 km s^{-1}, a density of 4×10^{-12} g cm^{-3}, and a density profile with a power-law index of −9. The absolute (but not relative) flux of the spectrum was calibrated using the interpolated P48 g and r magnitudes. We also show the O II, C II, C III and Si IV lines discussed in the text shifted to the velocity of the model photosphere.

In the model, the "W" feature mainly arises from the O II $2p^2$(3P)3s 4P ↔ $2p^2$(3P)3p 4D° (4639–4676 Å), O II $2p^2$(3P)3s 4P ↔ $2p^2$(3P)3p 2D (4649 Å) and O II $2p^2$(3P)3s 4P ↔ $2p^2$(3P)3p 4P° (4317–4357 Å) transitions. The departure from LTE is modest in the line-forming region, and the departure coefficients for the O II states are small. The spectrum redward of the "W" feature is shaped by carbon lines, and the features near 5700 and 6500 Å arise from the C II 3s 2S ↔ 3p 2P° (6578,6583 Å) and C III 2s3p 1P° ↔ 2s3d 1D (5696 Å) transitions, respectively. In the model, the C II feature is too weak, suggesting that the ionization level is too high in the model. There is also a contribution from the C III 2s3s 3S ↔ 2s3p 3P° (4647–4651 Å) transition to the red part of the "W" feature, which could potentially be what is seen in the spectra from earlier epochs. In addition, there is a contribution from Si IV 4s 2S ↔ 4p 2P° (4090, 4117 Å) near the blue side of the "W" feature, which produce a distinct feature in models with lower velocities and which could explain the observed feature on the blue side of the "W" feature.

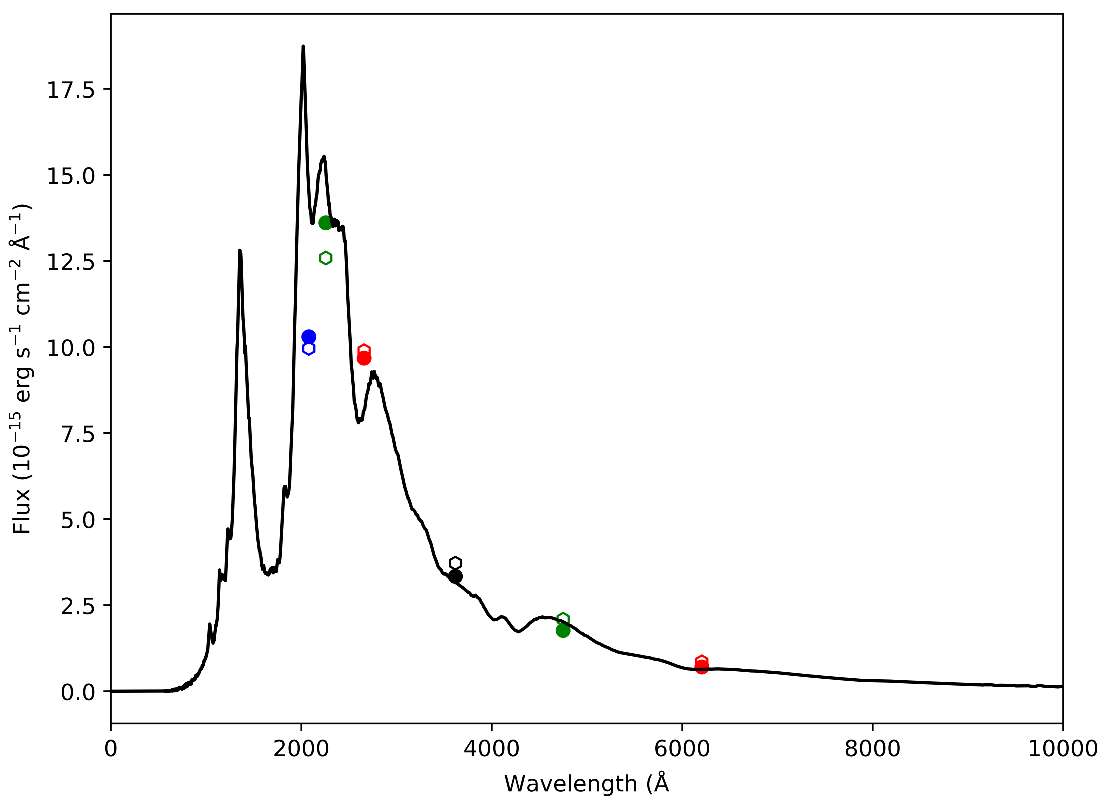

Figure 12. Comparison of model (filled circles) and observed (unfilled circles) mean fluxes through the *Swift* UVW1 (blue), UVM2 (green), UVW2 (red), and the SDSS u (black), g (green) and r (red) filters. We also show the model spectrum in black.

In spite of the overall good agreement, there is also some differences between the model and the observations. In particular the model spectrum is bluer and the velocities are higher. These two quantities are in tension and a better fit to one of them would result in a worse fit to the other. As mentioned above, the ionization level might be too high in the model, which suggests that the temperature might be too high as well. It should be noted that adding host extinction (which is assumed to be zero) or reducing the distance (within the error bars) would help in making the model redder (in the observer frame), and the latter would also help in reducing the temperature. The (modest) differences between the model and the observations could also be related to physics not included in the model, like a non-homologous velocity field, departures from spherical asymmetry and clumping.

The total luminosity of the model is $6.2{\times}10^{43}$ erg s^{-1}, the photosphere is located at $\sim$33,000 km s^{-1} and the temperature at the photosphere is $\sim$17,500 K, which is consistent with the values estimated from the blackbody fits (although the blackbody radius and temperature fits refer to the thermalization layer). As mentioned, we have also tried models with a O/Ne/Mg composition. However, these models failed to reproduce the carbon lines redwards of the "W" feature. We therefore conclude that the (outer) ejecta probably has a C/O-like composition, and that this composition in combination with a standard power-law density profile reproduce the spectrum of SN2018gep at the observed conditions (luminosity and velocity) 4.2 days after explosion. Further spectral modelling at other epochs is outside the scope of the paper, and something we hope to explore in future work.

Swift obtained three UV-grism spectra between 2018-09-15 3:29 and 6:58 UTC ($\Delta t \approx 6.4$ day) for a total exposure time of 3918 s. The UVOT grism spectrum (Figure 13) shows a single broad feature between 2200 Å and 3000 Å (rest frame). One possibility is that this is a blend of the UV features seen in SLSNe. Line identifications for these features vary in the SLSN literature, but are typically blends of Ti III, Si III, C II, C III, and Mg II (Quimby et al. 2011; Howell et al. 2013; Mazzali et al. 2016; Yan et al. 2017). In our model, this feature is dominated by the strong Mg II (2796,2803 Å) resonance line. However, a direct comparison is not reliable because the ionization is probably lower at this epoch than what we consider for our model.

After five days, we have a gap in coverage, and by the next epoch ($\Delta t = 7.8$ day) the spectrum qualitatively resembles a stripped-envelope supernova. From these spectra, we measure velocities from the Fe IIλ5169 line, which has been shown to be a good tracer of photospheric velocity (e.g., Branch et al. 2002). In SNe Ic-BL, this measurement is complicated by the blending of the Fe IIλ5169 line with the nearby Fe II$\lambda\lambda$4924,5018 lines due to the high velocities. To combat this, we employ the convolution method in Modjaz et al. (2016).

In Figure 14 we show the velocities inferred for SN2018gep from ionized C and O in the early spectra, as well as from Fe II in the Ic-BL spectra. The velocities are comparable to those measured for Ic-BL SNe associated with low-luminosity GRBs

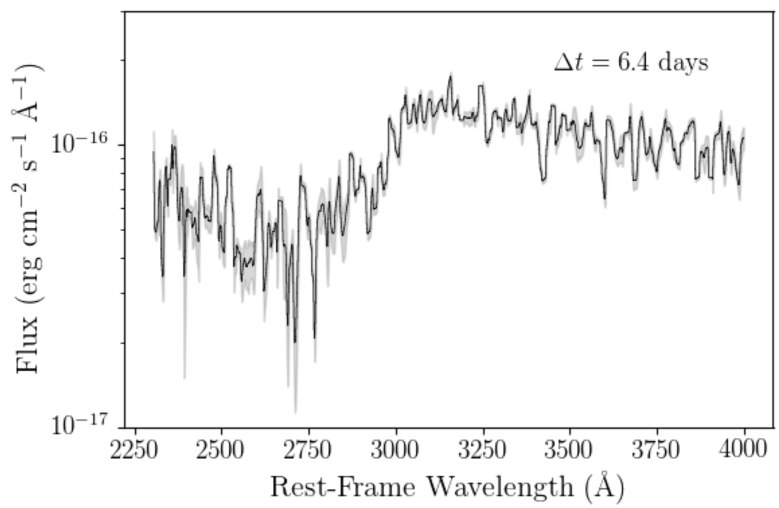

Figure 13. *Swift*/UVOT grism spectrum shifted to the rest frame. Black line shows the data binned such that each bin size is 10 Å. Light grey represents 1-σ uncertainties after binning. The spectrum has been scaled to match the UVOT u-band flux at this epoch (integrated from 3000 Å to 3900 Å), which was determined by interpolating the *Swift* u-band light curve.

(LLGRBs), which are systematically higher than those of Ic-BL SNe lacking GRBs (Modjaz et al. 2016), which in turn are systematically higher than Ic SNe (by definition).

3.3. *Properties of the host galaxy*

We infer a star-formation rate of 0.09 ± 0.01 $M_\odot\,\mathrm{yr}^{-1}$ from the Hα emission line using the Kennicutt (1998) relation converted to use a Chabrier initial mass function (Chabrier 2003; Madau, & Dickinson 2014). We note that this is a lower limit as the slit of the Keck observation did not enclose the entire galaxy. We estimate a correction factor of 2–3: the slit diameter in the Keck spectra was 1.0", and the extraction radius was $\sim 1.75''$ in the February observation and $\sim 1.21''$ in the March observation. The host diameter is roughly 4".

We derive an electron temperature of $13,100^{+900}_{-1000}$ K from the flux ratio between [O III]λ4641 and [O III]λ5007, using the software package PyNeb version 1.1.7 (Luridiana et al. 2015). In combination with the flux measurements of [O II]$\lambda\lambda$3226,3729, [O III]λ4364, [O III]λ4960, [O III]λ5008, and Hβ, we infer a total oxygen abundance of $8.01^{+0.10}_{-0.09}$ (statistical error; using Eqs. 3 and 5 in Izotov et al. 2006). Assuming a solar abundance of 8.69 (Asplund et al. 2009), the metallicity of the host is $\sim 20\%$ solar.

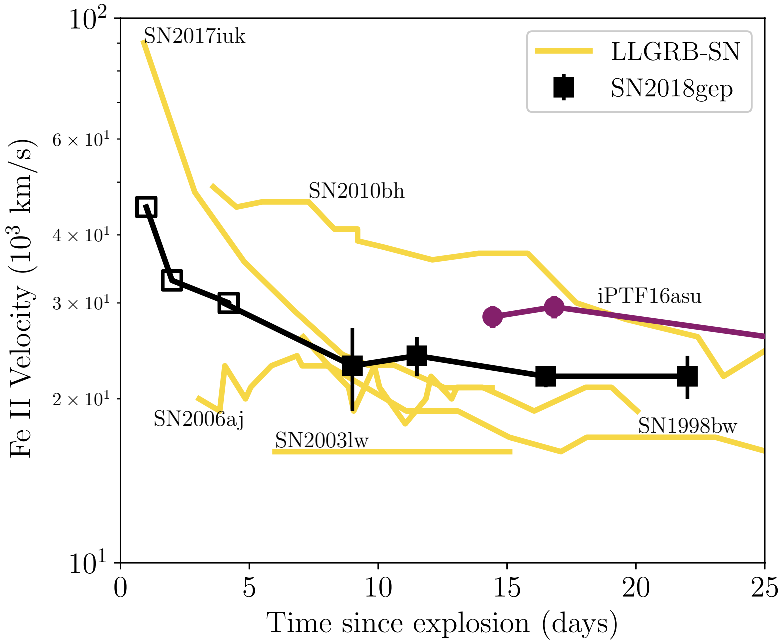

Figure 14. Velocity evolution over time as measured from spectral absorption features. Open symbols for SN2018gep come from C/O velocities measured from line minima. Closed symbols come from the Fe II feature in the Ic-BL spectra. The velocities are comparable to those measured for Ic-BL SNe associated with low-luminosity GRBs (LLGRBs). The velocity evolution for SN2017iuk is taken from Izzo et al. (2019). Velocities for iPTF16asu are taken from Whitesides et al. (2017). Velocities for the other Ic-BL SNe are taken from Modjaz et al. (2016) and shifted from V-band max using data from Galama et al. (1998), Campana et al. (2006), Malesani et al. (2004), and Bufano et al. (2012).

We also compute the oxygen abundance using the strong-line metallicity indicator O3N2 (Pettini, & Pagel 2004) with the updated calibration reported in Marino et al. (2013). The oxygen abundance in the O3N2 scale is $8.05 \pm 0.01\,(\mathrm{stat}) \pm 0.10\,(\mathrm{sys})$.[10]

We also estimate mass and star-formation rate by modeling the host SED; see Appendix D for a table of measurements, and details on where we obtained them. We use the software package LePhare version 2.2 (Arnouts et al. 1999; Ilbert et al. 2006)[11]. We generated 3.9×10^6 templates based on the Bruzual & Charlot (2003) stellar population-synthesis models with the Chabrier initial mass function (IMF; Chabrier 2003). The star formation history (SFH) was approximated by a declining exponential function of the form $\exp(t/\tau)$, where t is the age of the stellar population and τ the e-folding time-scale of the SFH (varied in nine steps between 0.1 and 30 Gyr). These templates were attenuated with the Calzetti attenuation curve (Calzetti et al. 2000) varied in 22 steps from $E(B-V) = 0$ to 1 mag .

As shown in Figure 15, the SED is well characterized by a galaxy mass of $\log M/M_\odot = 8.11^{+0.07}_{-0.08}$ and an attenuation-corrected star-formation rate of

[10] Note, the oxygen abundance of SN2018gep's host lies outside of the domain calibrated by Marino et al. (2013). However, we will use the measurement from the O3N2 indicator only to put the host in context of other galaxy samples that are on average more metal-enriched.

[11] http://www.cfht.hawaii.edu/~arnouts/LEPHARE/lephare.html

$0.12^{+0.08}_{-0.05}\,M_\odot\,\mathrm{yr}^{-1}$. The derived star-formation rate is comparable to measurement inferred from Hα. The attenuation of the SED is marginal, with $E(B-V)_{\rm star} = 0.05$, and consistent with the negligible Balmer decrement 2.8.

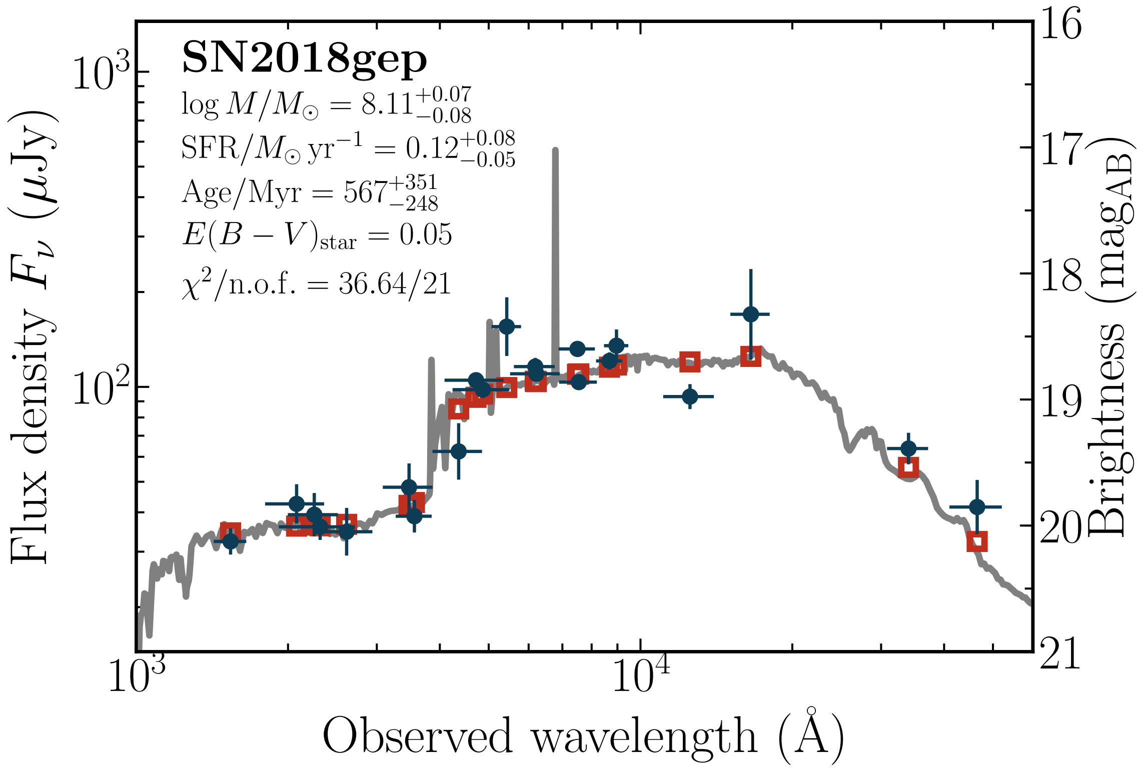

Figure 15. The spectral energy distribution of the host galaxy of SN2018gep from 1,000 to 60,000 Å and the best fit (solid line) in the observer frame. Filled data points represent photometric measurements. The error bars in the 'x' direction indicate the full-width half maximum of each filter response function. The open data points signify the model-predicted magnitudes. The quoted values of the host properties represent the median values and the corresponding 1-σ errors.

Figure 16 shows that the host galaxy of SN2018gep is even more low-mass and metal-poor than the typical host galaxies of Ic-BL SNe, which are low-mass and metal-poor compared to the overall CC SN population to begin with. The figure uses data for 28 Ic-BL SNe from PTF and iPTF (Modjaz et al. 2019; Taddia et al. 2019) and a sample of 11 long-duration GRBs (including LLGRBs, all at $z < 0.3$). We measured the emission lines from the spectra presented in Taddia et al. (2019) and used line measurements reported in Modjaz et al. (2019) for objects with missing line fluxes. The photometry was taken from Schulze et al. (in prep.). Photometry and spectroscopy were taken from a variety of sources[12]. The oxygen abundances were measured in the O3N2 scale like for SN2018gep and their SEDs were modelled with

[12] Gorosabel et al. (2005), Bersier et al. (2006), Margutti et al. (2007), Ovaldsen et al. (2007) Kocevski et al. (2007), Thöne et al. (2008), Michałowski et al. (2009), Han et al. (2010), Levesque et al. (2010), Starling et al. (2011), Hjorth et al. (2012), Thöne et al. (2014), Schulze et al. (2014), Krühler et al. (2015), Stanway et al. (2015), Toy et al. (2016), Izzo et al. (2017), and Cano et al. (2017)

Table 3. Key observational properties of SN2018gep and its host galaxy

Parameter	Value	Notes
z	0.03154	From host emission
$L_{\rm peak}$	$\gtrsim 3 \times 10^{43}$ erg	Peak UVOIR bolometric luminosity
$t_{\rm rise}$	0.5–3 day	Time from t_0 to $L_{\rm peak}$
$E_{\rm rad}$	10^{50} erg	UVOIR output, $\Delta t = 0.5$–40 day
$M_{r,\rm prog}$	-15	Peak luminosity of pre-explosion emission
$E_{\gamma,\rm iso}$	$< 4.9 \times 10^{48}$	Limit on prompt gamma-ray emission from *Fermi*/GBM
L_X	$< 2.5 \times 10^{41}\,\rm erg\,s^{-1}$	X-ray upper limit from *Swift*/XRT at $\Delta t = 0.4$–14 day
	$< 10^{40}\,\rm erg\,s^{-1}$	X-ray upper limit from *Chandra* at $\Delta t = 15$ and $\Delta t = 70$ day
νL_ν	$\approx 10^{37}\,\rm erg\,s^{-1}$	9 GHz radio luminosity from VLA at $\Delta t = 5$ and $\Delta t = 16$
$M_{*,\rm host}$	$1.3 \times 10^8\,M_\odot$	Host stellar mass
$\rm SFR_{host}$	$0.12\,M_\odot\,\rm yr^{-1}$	Host star-formation rate
Host metallicity	1/5 solar	Oxygen abundance on O3N2 scale

the same set of galaxy templates. For reference, the mass and SFR of the host of AT2018cow was $1.4 \times 10^9\,M_\odot$ and $0.22\,M_\odot\,\rm yr^{-1}$, respectively (Perley et al. 2019a). The mass and SFR of the host of iPTF16asu was $4.6^{+6.5}_{-2.3} \times 10^8\,M_\odot$ and $0.7\,M_\odot\,\rm yr^{-1}$, respectively (Whitesides et al. 2017).

4. INTERPRETATION

In the death of a massive star, the collapse of the core launches a shockwave dominated and mediated by radiation. Sustained by absorbing $\sim 1\%$ of the thermal neutrinos produced in the core, this bounce shock propagates through the collapsing material and accelerates through a steepening density profile. In its wake, stellar material is compressed and heated, and expands. Initially the expansion of this ejecta is accelerated through the conversion of radiation energy to bulk kinetic energy. Eventually the kinetic energy density dominates over the radiation energy density, and the ejecta coasts at a constant velocity (free homologous expansion).

Initially, no electromagnetic radiation can escape because the optical depth of the ejecta is too high. As the ejecta expands, however, its optical depth drops. Photons emitted at the shock front escape when their diffusion time becomes shorter than the dynamical expansion time of the ejecta, $t_{\rm diff} \sim \tau R_{\rm ej}/c < R_{\rm ej}/v_{\rm ej}$, corresponding to $\tau < c/v_{\rm ej}$. The emergence of these photons, referred to as "shock breakout," is the first electromagnetic signal from the explosion (Colgate 1974; Nakar & Sari 2010; Rabinak & Waxman 2011; Sapir & Waxman 2017).

After shock breakout, photons continue to diffuse out of the hot expanding ejecta; this is "post-shock cooling emission." At any given time, the light curve is dominated by the innermost shell out of which photons can effectively diffuse, which has $\tau = c/v_{\rm ej}$. Without any additional source of energy, this process can power a light curve with luminosity $\sim 10^{42}\,\rm erg\,s^{-1}$ and lasting R/c. To explain more luminous light curves

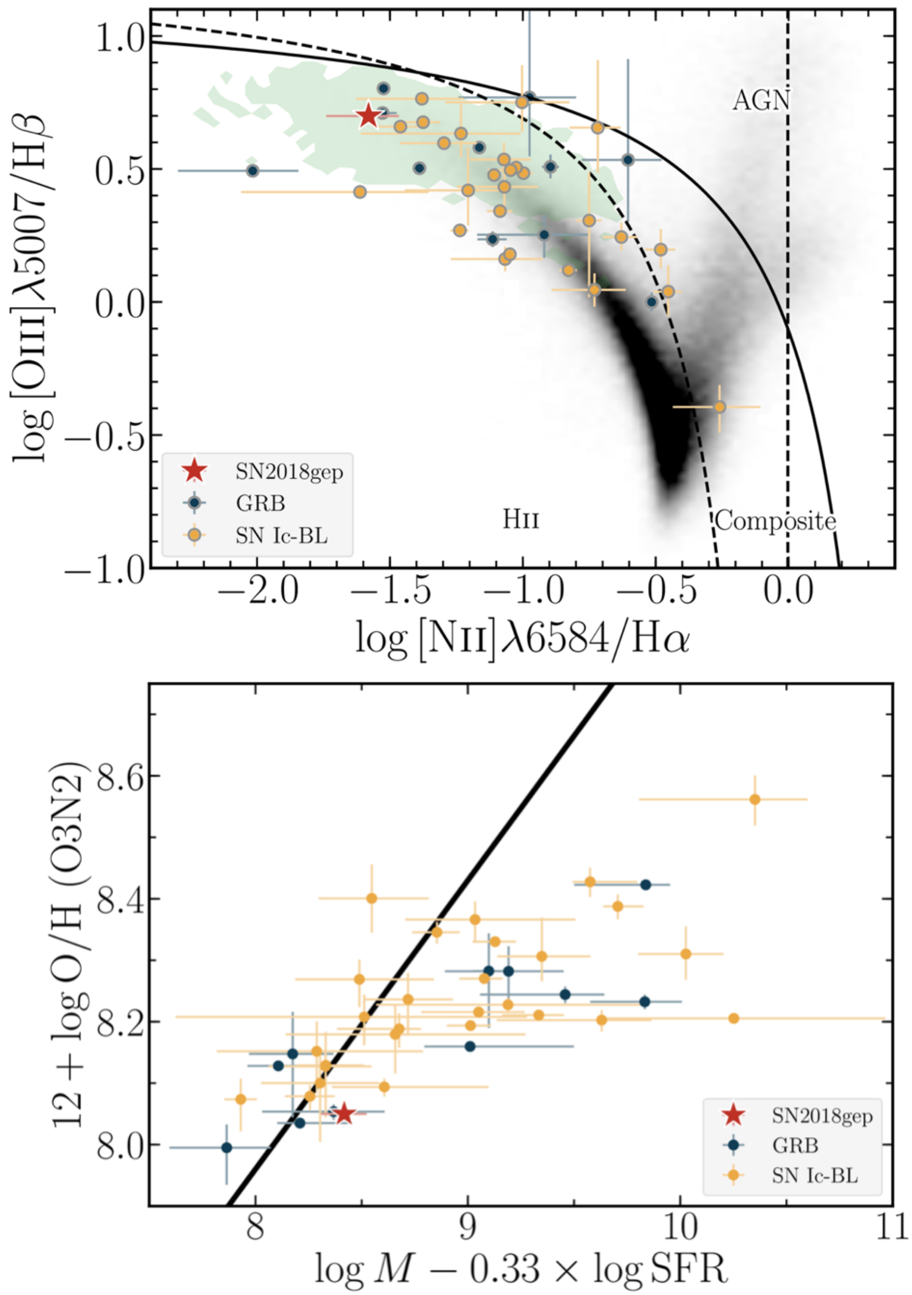

Figure 16. Top: BPT diagram. The host of SN2018gep is a low-metallicity galaxy with an intense ionizing radiation field (green shaded region indicates extreme emission line galaxies). The majority of Ic-BL SNe and long-duration GRBs are found in more metal enriched galaxies (parameterized by [N II]/Hα), and galaxies with less intense radiation fields (parameterized by [O III]/Hα). Field galaxies from SDSS DR15 are shown as a background density distribution. The thick solid line separates star formation- and AGN-dominated galaxies (Kewley et al. 2001). The thick dashed lines encircle the region of composite galaxies (Kauffmann et al. 2003). Bottom: The mass-metallicity-star-formation-rate plane. The bulk of the the SN-Ic-BL and GRB host populations are found in hosts that are more metal enriched. For reference, the host of AT2018cow had $\log M - 0.33 \times \log \mathrm{SFR} \approx 9.4$. The black line is the fundamental metallicity relation in Mannucci et al. (2010).

like the one in SN2018gep, additional energy sources are required. Here we consider the contributions of radioactive decay and interaction with extended circumstellar material (CSM).

4.1. *Radioactive decay*

The majority of stripped-envelope SNe have light curves powered by the radioactive decay of ^{56}Ni. As discussed in Kasen (2017), this mechanism can be ruled out for light curves that rise rapidly to a high peak luminosity, because this would require the unphysical condition of a nickel mass that exceeds the total ejecta mass. With a peak luminosity exceeding $10^{44}\,\mathrm{erg\,s^{-1}}$ and a rise to peak of a few days, SN2018gep clearly falls into the disallowed region (see Figure 1 in Kasen 2017). Thus, we rule out radioactive decay as the mechanism powering the peak of the light curve.

We now consider whether radioactive decay could dominate the light curve at late times ($t \gg t_{\mathrm{peak}}$). The left panel of Figure 17 shows the bolometric light curve of SN2018gep compared to several other Ic-BL SNe from the literature (Cano 2013), whose light curves are thought to be dominated by the radioactive decay of ^{56}Ni (although see Moriya et al. (2017) for another possible interpretation). The luminosity of SN2018gep at $t \sim 20$ day is about half that of SN1998bw, double that of SN2010bh and SN2006aj. By modeling the light curves of the three Ic-BL SNe shown, Cano (2013) infers nickel masses of $0.42\,M_{\odot}$, $0.12\,M_{\odot}$, and $0.21\,M_{\odot}$, respectively. On this scale, SN2018gep has $M_{\mathrm{Ni}} \sim 0.1$–$0.2\,M_{\odot}$.

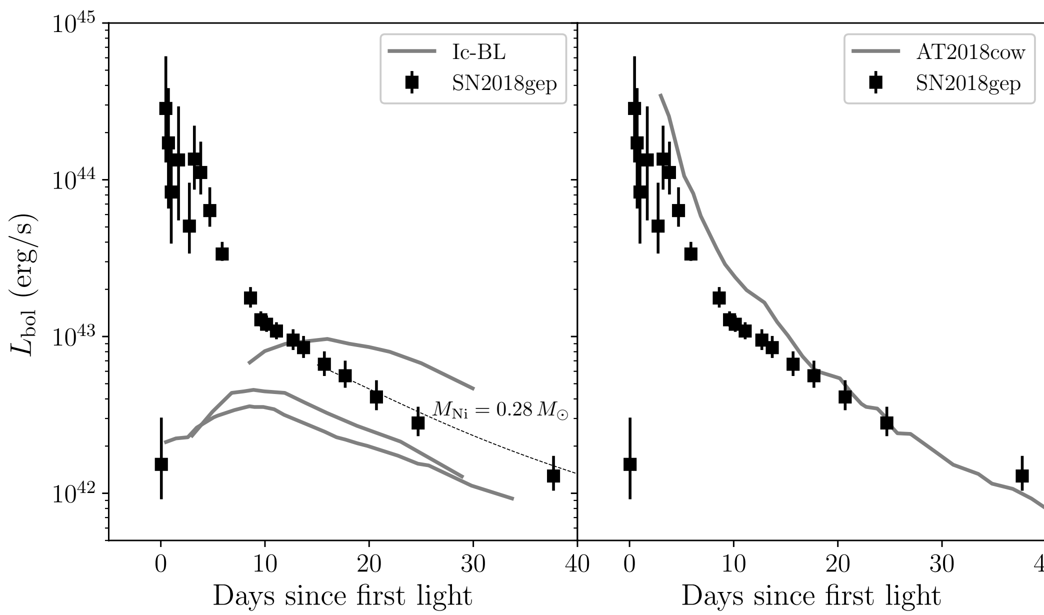

Figure 17. The bolometric light curve of SN2018gep compared to (left) other Ic-BL SNe from the literature (Cano 2013) and (right) to AT2018cow (Perley et al. 2019a). The dotted line shows the expected contribution from the radioactive decay of ^{56}Ni, for a gamma-ray escape time of 30 day and M_{Ni}=$0.28\,M_{\odot}$. In order of decreasing L_{bol}, the three Ic-BL SNe are SN1998bw, SN2010bh, and SN2006aj.

The right panel of Figure 17 shows the light curve of SN2018gep compared to that of AT2018cow (Perley et al. 2019a). To estimate the nickel mass of AT2018cow, Perley et al. (2019a) compared the bolometric luminosity at $t \sim 20\,\mathrm{day}$ to that of SN2002ap (whose nickel mass was derived via late-time nebular spectroscopy; Foley et al. 2003) and found $M_{\mathrm{Ni}} < 0.05\,M_\odot$. On this scale, we would expect $M_{\mathrm{Ni}} \lesssim 0.05\,M_\odot$ for SN2018gep as well.

Finally, Katz et al. (2013) and Wygoda et al. (2019) present an analytical technique for testing whether a light curve is powered by radioactive decay. At late times, the bolometric luminosity is equal to the rate of energy deposition by radioactive decay $Q(t)$, because the diffusion time is much shorter than the dynamical time: $L_{\mathrm{bol}}(t) = Q(t)$. At any given time, the energy deposition rate $Q(t)$ is

$$Q(t) = Q_\gamma(t)\left(1 - e^{-(t_0/t)^2}\right) + Q_{\mathrm{pos}}(t) \tag{1}$$

where $Q_\gamma(t)$ is the energy release rate of gamma-rays and t_0 is the time at which the ejecta becomes optically thin to gamma rays. The expression for $Q_\gamma(t)$ is

$$Q_\gamma(t) = \frac{M_{\mathrm{Ni}}}{M_\odot}\left(6.45e^{-t/8.76\,\mathrm{d}} + 1.38e^{-t/111.4\,\mathrm{d}}\right) \times 10^{43}\,\mathrm{erg\,s^{-1}}. \tag{2}$$

$Q_{\mathrm{pos}}(t)$ is the energy deposition rate of positron kinetic energy, and the expression is

$$Q_{\mathrm{pos}}(t) = 4.64\frac{M_{\mathrm{Ni}}}{M_\odot}\left(-e^{-t/8.76\,\mathrm{d}} + e^{-t/111.4\,\mathrm{d}}\right) \times 10^{41}\,\mathrm{erg\,s^{-1}}. \tag{3}$$

The dotted line in Figure 17 shows a model track with $M_{\mathrm{Ni}} = 0.28\,M_\odot$ and $t_0 = 30\,\mathrm{day}$. Lower nickel masses produce tracks that are too low to reproduce the data, and larger values of t_0 produce tracks that drop off too rapidly. Thus on this scale it seems that $M_{\mathrm{Ni}} \sim 0.3\,M_\odot$, similar to other Ic-BL SNe (Lyman et al. 2016).

We can also try to solve directly for t_0 and M_{Ni} using the technique for Ia SNe in Wygoda et al. (2019). The first step is to solve for t_0 using Equation 1 and a second equation resulting from the fact that the expansion is adiabatic,

$$\int_0^t Q(t')\,t'\,dt' = \int_0^t L_{\mathrm{bol}}(t')\,t'\,dt'. \tag{4}$$

The ratio of Equation 1 to Equation 4 removes the dependence on M_{Ni}, and enables t_0 to be measured. However, as shown in Figure 18, the data have not yet converged to model tracks.

4.2. *Interaction with extended material*

One way to power a rapid and luminous light curve is to deposit energy into circumstellar material (CSM) at large radii (Nakar & Sari 2010; Nakar & Piro 2014; Piro 2015). Since this is a Ic-BL SN, we expect the progenitor to be stripped of its envelope and therefore compact ($R \sim 0.5\,R_\odot \sim 10^{10}\,\mathrm{cm}$; Groh et al. 2013), although this has

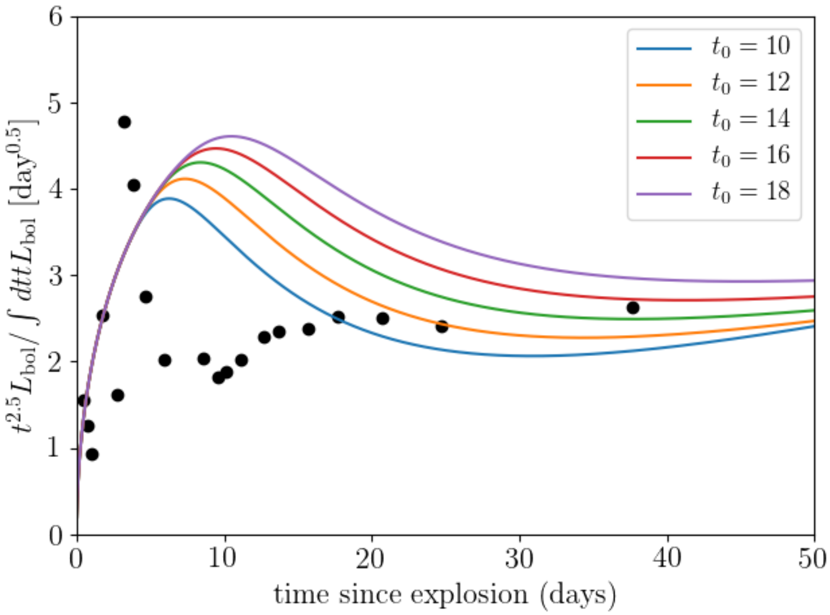

Figure 18. To test whether a light curve is powered by radioactive decay, the ratio of the bolometric luminosity to the time-weighted integrated bolometric luminosity should converge to model tracks, as described in Katz et al. (2013) and Wygoda et al. (2019). This enables a direct measurement of the gamma-ray escape time t_0 and the nickel mass $M_{\rm Ni}$. However, our data have not converged to these tracks, suggesting that either radioactive decay is not dominant, or that we are not yet in a phase where we can perform this measurement.

never been directly observed for a Ic-BL, with only one candidate for a Type Ic SN (Van Dyk 2017; Van Dyk et al. 2018). Given this picture, the presence of extended material at larger radii would point to mass-loss. This would not be surprising, as massive stars are known to shed a significant fraction of their mass in winds and eruptive episodes; see Smith (2014) for a review. This picture is supported by our detections of precursor emission.

First we perform an order-of-magnitude calculation to see whether the rise time and peak luminosity could be explained by a model in which shock interaction powers the light curve ("wind shock breakout"). Assuming that the progenitor ejected material with a velocity v_w at a time t prior to explosion, the radius of this material at any given time is

$$R_{\rm sh} = R_* + v_{\rm w} t \approx (8.64 \times 10^{12}\,{\rm cm}) \left(\frac{v_w}{1000\,{\rm km\,s^{-1}}}\right) \left(\frac{t}{\rm day}\right). \tag{5}$$

For material ejected 15 days prior to explosion, traveling at $1000\,{\rm km\,s^{-1}}$, the radius would be $R_{\rm CSM} \sim 10^{14}\,{\rm cm}$ at the time of explosion. The shock crossing timescale is $t_{\rm cross}$:

$$t_{\rm cross} \sim R_{\rm CSM}/v_s \approx (12\,{\rm day}) \left(\frac{R}{10^{14}\,{\rm cm}}\right) \left(\frac{v_s}{1000\,{\rm km\,s^{-1}}}\right)^{-1} \tag{6}$$

where v_s is the velocity of the shock. The shock heats the CSM with an energy density that is roughly half of the kinetic energy of the sock, so $e_s \sim (1/2)(\rho v_s^2/2)$. The luminosity is the total energy deposited divided by $t_{\rm cross}$,

$$L_{\rm BO} \sim \frac{E_{\rm BO}}{t_{\rm cross}} \sim \frac{v_s^3}{4}\frac{dM}{dR} = (3\times10^{43}\,{\rm erg\,s^{-1}})\left(\frac{v_s}{1000\,{\rm km\,s^{-1}}}\right)^3\left(\frac{dM}{M_\odot}\right)\left(\frac{dR}{10^{14}\,{\rm cm}}\right)^{-1} \quad (7)$$

assuming a constant density. Thus, for reasonable shock velocities of a few thousand $\rm km\,s^{-1}$, it is easy to explain the rise time and peak luminosity that we observe.

To test whether shock breakout (and subsequent post-shock cooling) can explain the evolution of the physical properties we measured in Section 3, we run one-dimensional numerical radiation hydrodynamics simulations of a SN running into a circumstellar shell with CASTRO (Almgren et al. 2010; Zhang et al. 2011). We assume spherical symmetry and solve the coupled equations of radiation hydrodynamics using a grey flux-limited non-equilibrium diffusion approximation. The setup is similar to the models presented in Rest et al. (2018) but with parameters modified to fit SN2018gep. A full discussion of modeling CSM interaction will be presented in a future work (Khatami et al., in prep).

The ejecta is assumed to be homologously expanding, characterized by a broken power-law density profile, an ejecta mass $M_{\rm ej}$, and energy $E_{\rm ej}$. We adopt $n = 0$ and $\delta = 10$ for the inner and outer ejecta profiles, respectively, as is appropriate for core-collapse SN explosions (Matzner & McKee 1999). The circumstellar shell is assumed to be uniform in density with radius $R_{\rm CSM}$ and mass $M_{\rm CSM}$. We adopt a uniform opacity of $\kappa = 0.2$ cm^2 g^{-1}, which is characteristic of hydrogen-poor electron scattering.

The best-fit model, shown in Figure 19, used the following parameters: $M_{\rm ej} = 8\,M_\odot$, $E_{\rm ej} = 2\times10^{52}\,{\rm erg}$, $M_{\rm CSM} = 0.02\,M_\odot$, and $R_{\rm CSM} = 3\times10^{14}\,{\rm cm}$. The inferred kinetic energy is consistent with typical values measured for Ic-BL SNe (e.g. Cano et al. 2017; Taddia et al. 2019), and $R_{\rm CSM}$ is similar in value to the first photospheric radius we measure (at $\Delta t = 0.05\,$day; see Figure 8).

In this framework, the shockwave sweeps through the CSM prior to peak luminosity, so that at maximum luminosity the outer parts of the CSM have been swept into a dense shell moving at SN-like velocities ($v_{\rm post-shock} \approx 3v_s/4$). This scenario was laid out in Chevalier & Irwin (2011) and discussed in Kasen (2017). This explains the high velocities we measure at early times and the absence of narrow emission features in our spectra. For another discussion of the absence of narrow emission lines due to an abrupt cutoff in CSM density, see Moriya & Tominaga (2012). Following Chevalier & Irwin (2011), the rapid rise corresponds to shock breakout from the CSM, and begins at a time $R_{\rm CSM}/v_{\rm sh}$ after the explosion, where $v_{\rm sh}$ is the velocity of the shock. The time to peak luminosity (1.2 day) is longer than this delay time by a factor (R_w/R_d). Given the best-fit $R_w = 3\times10^{14}\,{\rm cm}$, and assuming $R_d \sim R_w$, we find $v_{\rm sh} = 0.1c$, and an explosion time $\sim 1\,$day prior to t_0. This model also predicts an increasing

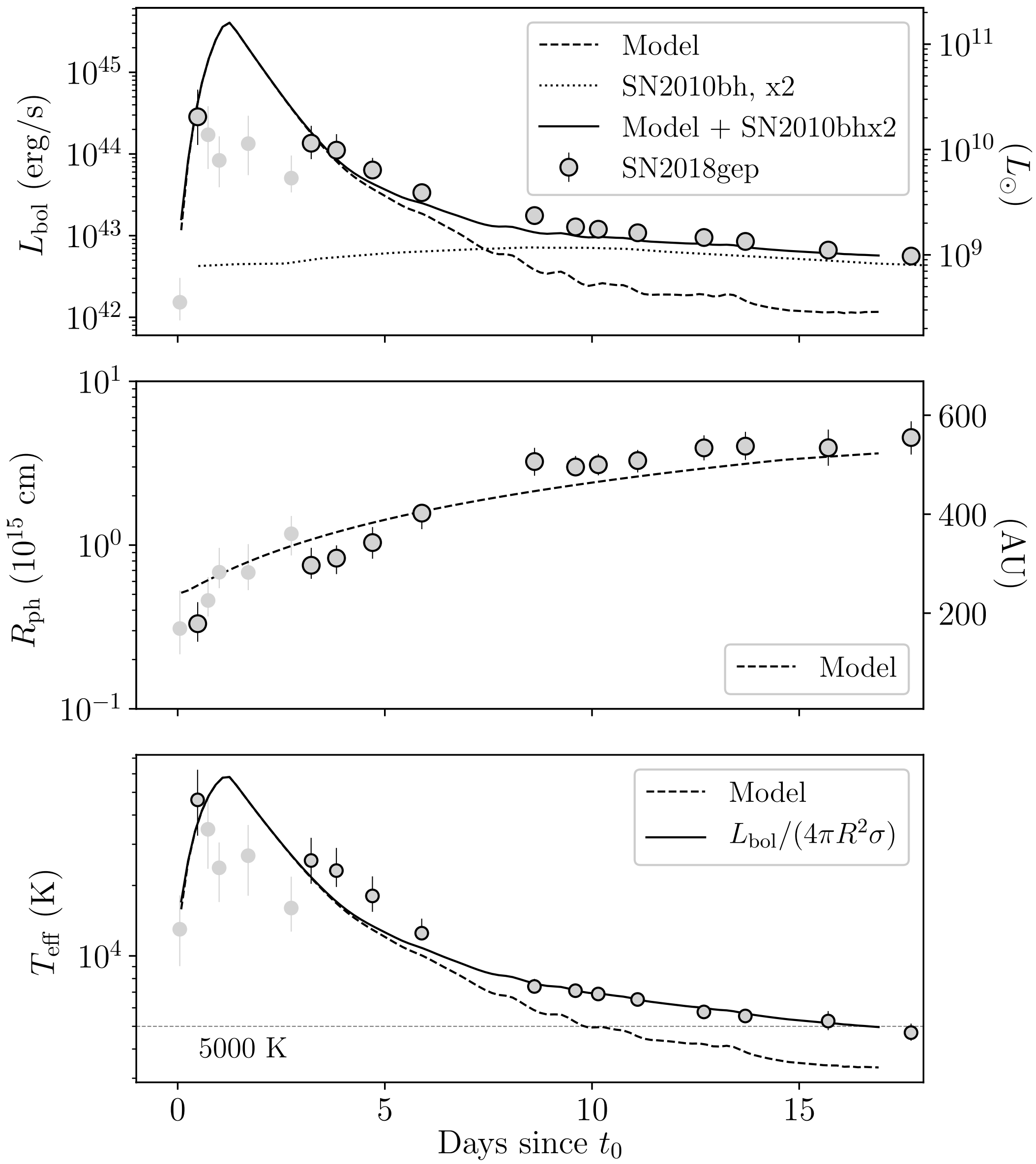

Figure 19. Best-fit CSM interaction model with the light curve of the Ic-BL SN 2010bh (Cano 2013) scaled up by a factor of two. The model parameters are $M_{\rm ej} = 8\,M_\odot$, $E_{\rm ej} = 2 \times 10^{52}$ erg, $M_{\rm CSM} = 0.02\,M_\odot$, and $R_{\rm CSM} = 3 \times 10^{14}$ cm. As in Figure 8, the outlined circles are derived from UV and optical data, while the light grey circles are derived from optical data only.

temperature while the shock breaks out (i.e. during the rise to peak bolometric luminosity).

Other Ic SNe have shown early evidence for interaction in their light curves, but in other cases the emission has been attributed to post-shock cooling in expanding material rather than shock breakout itself. For example, the first peak observed in iPTF14gqr (De et al. 2018) was short-lived ($\lesssim 2$ day) and attributed to shock-cooling emission from material stripped by a compact companion. iPTF14gqr is different in a number of ways from SN2018gep: the spectra showed high-ionization emission lines, including He II, and the explosion had a much smaller kinetic energy ($E_K \approx 10^{50}$ erg) and smaller velocities (10,000 $\mathrm{km\,s^{-1}}$). The main peak in iPTF16asu was also modeled as shock-cooling emission rather than shock breakout (Whitesides et al. 2017).

Under the assumption that the light curve represented post-shock cooling emission, De et al. (2018) and Whitesides et al. (2017) both used one-zone analytic models from Piro (2015) to estimate the properties of the explosion and the CSM. This approximation assumes that the emitting region is a uniformly heated expanding sphere. In iPTF14gqr the inferred properties of the extended material were $M_e \sim 8\times10^{-3}\,M_\odot$ at $R_e \sim 3\times10^{13}$ cm. In iPTF16asu the inferred properties of the extended material were $M_e \sim 0.45\,M_\odot$ at $R_e \sim 1.7\times10^{12}$ cm. The fit also required a more energetic explosion than iPTF14gqr (4×10^{51} erg). By applying the same framework to the decline of the bolometric light curve of SN2018gep, we arrive at similar values to those inferred for iPTF16asu, as shown in Figure 20.

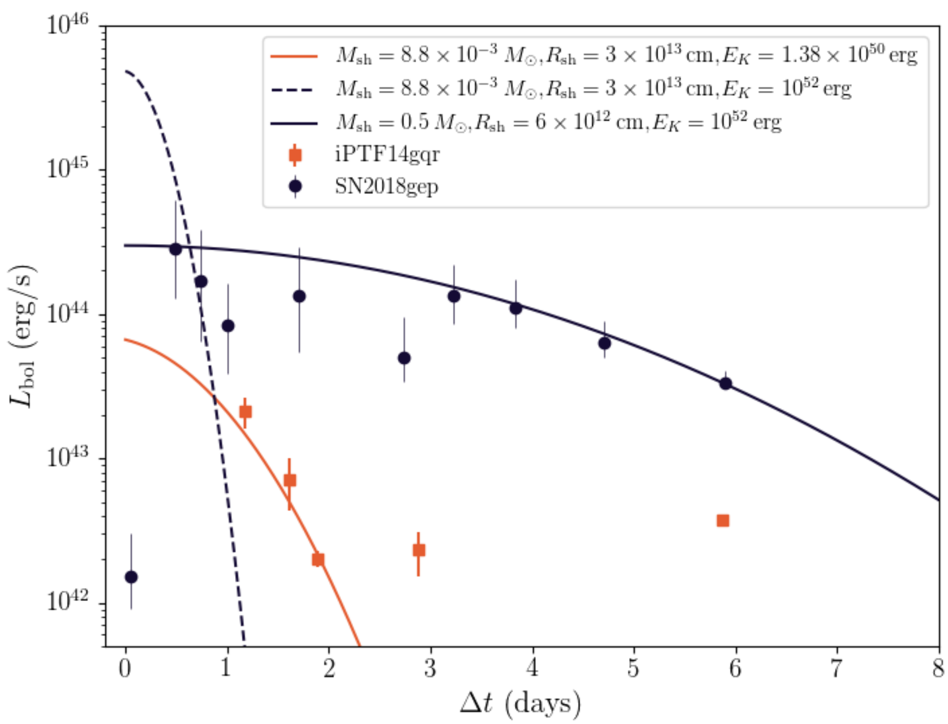

Figure 20. Estimated CSM and explosion properties using models from Piro (2015). The shell mass is much larger than the one in iPTF14gqr, which is the reason for the more extended shock-cooling peak.

We model the main peak of SN2018gep as shock breakout rather than post-shock cooling emission. Our motivation for this choice is that the timescale over which we detect the precursor emission is more consistent with a large radius and lower shell mass. From the shell mass and radius, we can also estimate the mass-loss rate immediately prior to explosion,

$$\frac{\dot{M}}{M_\odot\,\mathrm{yr}^{-1}} \approx 32 \left(\frac{M_\mathrm{sh}}{M_\odot}\right) \left(\frac{v_w}{1000\mathrm{km\,s^{-1}}}\right) \left(\frac{R_\mathrm{sh}}{10^{14}\mathrm{cm}}\right)^{-1}. \tag{8}$$

For our best-fit parameters $M_\mathrm{sh} = 0.02\,M_\odot$ and $R_\mathrm{sh} = 3 \times 10^{14}\,\mathrm{cm}$, and taking $v_w = 1000\,\mathrm{km\,s^{-1}}$, we find $\dot{M} \approx 0.6\,M_\odot\,\mathrm{yr}^{-1}$, 4–6 orders of magnitude higher than what is typically expected for Ic-BL SNe (Smith 2014).

In the shock breakout model, the shock sweeps through confined CSM and passes into lower-density material. Thus, it is not surprising that we do not observe the X-ray or radio emission that would indicate interaction with high-density material. From our VLA observations of SN2018gep, the radio flux marginally decreased from $\Delta t = 5\,\mathrm{day}$ to $\Delta t = 75\,\mathrm{day}$. This could be astrophysical, but could also be instrumental (change in beamsize due to change in VLA configuration). Using the relation of Murphy et al. (2011), the estimated contribution from the host galaxy (for a SFR of $0.12^{+0.08}_{-0.05}\,M_\odot\,\mathrm{yr}^{-1}$; see Section 3.3) is

$$\left(\frac{L_{1.4\,\mathrm{GHz}}}{\mathrm{erg\,s^{-1}\,Hz^{-1}}}\right) \approx 1.57 \times 10^{28} \left(\frac{\mathrm{SFR_{radio}}}{M_\odot\,\mathrm{yr}^{-1}}\right) \approx 1.9 \times 10^{27}\,\mathrm{erg\,s^{-1}\,Hz^{-1}}. \tag{9}$$

Taking a spectral index of -0.7 (a synchrotron spectrum), the expected 9 GHz luminosity would be between $3.0 \times 10^{26}\,\mathrm{erg\,s^{-1}\,Hz^{-1}}$ and $8.6 \times 10^{26}\,\mathrm{erg\,s^{-1}\,Hz^{-1}}$. From Table 1, the measured spectral luminosity is $8.3 \times 10^{26}\,\mathrm{erg\,s^{-1}\,Hz^{-1}}$ (at 10 GHz) in the first epoch, and $6 \times 10^{26}\,\mathrm{erg\,s^{-1}\,Hz^{-1}}$ (at 9 GHz) in the second epoch. The slit covering fraction of our LRIS observations is again relevant here; as discussed in Section 3.3, the true SFR is likely a factor of a few higher than what we inferred from modeling the galaxy SED. So, it is plausible that the first two radio detections are entirely due to the host galaxy.

In the third epoch, the luminosity is (at 9 GHz) is $< 3.9 \times 10^{26}\,\mathrm{erg\,s^{-1}\,Hz^{-1}}$, although the difference from the first two epochs may be due to the different array configuration. Taking the peak of the 9–10 GHz light curve to be $8.3 \times 10^{26}\,\mathrm{erg\,s^{-1}\,Hz^{-1}}$ at $\Delta t \approx 5\,\mathrm{day}$, Figure 21 shows that SN2018gep would be an order of magnitude less luminous in radio emission than any other Ic-BL SN. If the luminosity truly decreased, then the implied mass-loss rate is $\dot{M} \sim 3 \times 10^{-6}$, consistent with the idea that the shock has passed from confined CSM into much lower-density material.

If the emission is constant and due entirely to the host galaxy, the point shown in Figure 21 is an upper limit in luminosity. Assuming that the peak of the SED of any radio emission from the SN is not substantially different from the frequencies we measure (i.e. that the spectrum is not self-absorbed at these frequencies), we have a limit on the 9 GHz radio luminosity of $L_p \lesssim 10^{27}\,\mathrm{erg\,s^{-1}\,Hz^{-1}}$ at $\Delta t \approx 5$–$15\,\mathrm{day}$.

The shell mass and radius also give an estimate of the optical depth: $\tau \approx \kappa M/r^2 \approx 100 >> 1$, which means that the shell would be optically thick. The lack of detected

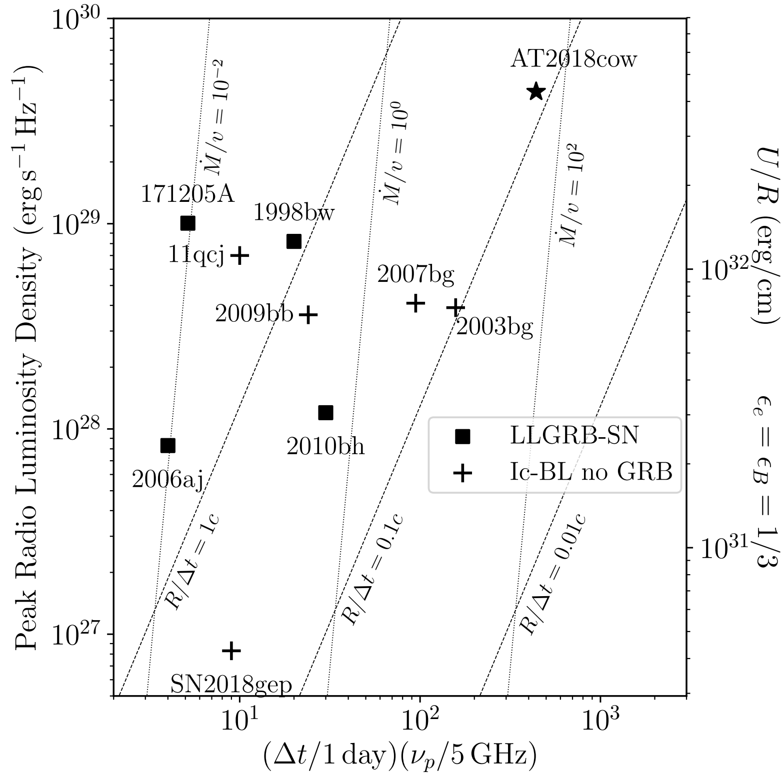

Figure 21. The radio luminosity of SN2018gep compared to AT2018cow and radio-loud Ic-BL SNe (assuming $\epsilon_e = \epsilon_B = 1/3$, cf. Chevalier 1998; Soderberg et al. 2010; Ho et al. 2019). Lines of constant mass-loss rate (scaled to wind velocity) are shown in units of $10^{-4}\,M_\odot\,\mathrm{yr}^{-1}/1000\,\mathrm{km\,s}^{-1}$. The radio luminosity for GRB 171205A was taken from VLA observations reported by Laskar et al. (2017), but we note that this is a lower limit in luminosity and in peak frequency because the source was heavily self-absorbed at this epoch.

X-ray emission is consistent with the expectation that any X-ray photons produced in the collision would be thermalized by the shell and reradiated as blackbody emission.

Finally, we return to the question of the emission detected in the first few minutes, which showed an inflection point prior to the rapid rise to peak (Figure 2). Given the pre-explosion activity and inference of CSM interaction, it is not surprising that the rise is not well-modeled by a simple quadratic function. One possibility is that we are seeing ejecta already heated from earlier precursor activity. Another possibility is that we are seeing the effects of a finite light travel time. For a sphere of $R \sim 3 \times 10^{14}$ cm, the light crossing time is ~ 20 minutes. The slower rising phase could represent the time for photons to reach us across the extent of the emitting sphere.

In Table 4, we summarize the key properties inferred from Section 4.

5. COMPARISON TO UNCLASSIFIED RAPIDLY EVOLVING TRANSIENTS AT HIGH REDSHIFT

In terms of the timescale of its light curve evolution, SN2018gep is similar to AT2018cow in fulfilling the criteria that optical surveys use to identify rapidly evolv-

Table 4. Key model properties of SN2018gep

Parameter	Value	Notes
$t_{\rm rise}$	1.2 day	
$E_{\rm SN}$	2×10^{52} erg	
$M_{\rm ej}$	$8\,M_\odot$	
$M_{\rm CSM}$	$0.02\,M_\odot$	
$R_{\rm CSM}$	3×10^{14} cm	
$\dot{M}$	$0.6\,M_\odot\,{\rm yr}^{-1}$	Assuming $v_w = 1000\,{\rm km\,s}^{-1}$
$M_{\rm Ni}$	< 0.2–$0.3\,M_\odot$	

ing transients (e.g. Drout et al. 2014; Tanaka et al. 2016; Pursiainen et al. 2018). However, there are a number of ways in which SN2018gep is more of a "typical" member of these populations than AT2018cow. In particular, SN2018gep has an expanding photospheric radius and declining effective temperature. By contrast, one of the challenges in explaining AT2018cow as a stellar explosion was its nearly constant temperature (persistent blue color) and *declining* photospheric radius. In Figure 22 we show these two different kinds of evolution as very different tracks in color-magnitude space. We also show a late-time point for KSN2015K (Rest et al. 2018), which shows blue colors even after the transient had faded to half-max. The mass-loss rate inferred for Rest et al. (2018) was $2 \times 10^{-3}\,M_\odot\,{\rm yr}^{-1}$.

Of the PS-1 events, most appear to expand, cool, and redden with time (Drout et al. 2014). That said, there are few co-eval data points in multiple filters, even in the gold sample transients. The transients are also faint; all but one lie at $z > 0.1$. Of the DES sample, most also show evidence for declining temperatures and increasing radii, although three show evidence of a constant temperature and decreasing radius: 15X3mxf, 16X1eho, and 15C3opk. The peak bolometric luminosities for these three transients are reported as $3 \times 10^{43}\,{\rm erg\,s}^{-1}$, $9 \times 10^{43}\,{\rm erg\,s}^{-1}$, and $5 \times 10^{43}\,{\rm erg\,s}^{-1}$, respectively (Pursiainen et al. 2018).

To estimate a rate of Ic-BL SNe that have a light curve powered by shock breakout, we used the sample of 25 nearby ($z < 0.1$) Ic-BL SNe from PTF (Taddia et al. 2019), because these were found in an untargeted survey. Of these, we could not draw a conclusion about eight (either because the peak was not resolved or there was no multi-color photometry available around peak, or both). The remaining clearly lacked the rise time or blue colors of SN2018gep. Furthermore, SN2018gep is unique among the sample of 12 nearby ($z < 0.1$) Ic-BL SNe from ZTF discovered so far (Ho et al. in prep). From this, we estimate that the rate of Ic-BL SNe with a main peak dominated by shock breakout is no more than 10% of the rate of Ic-BL SNe.

6. SUMMARY AND FUTURE WORK

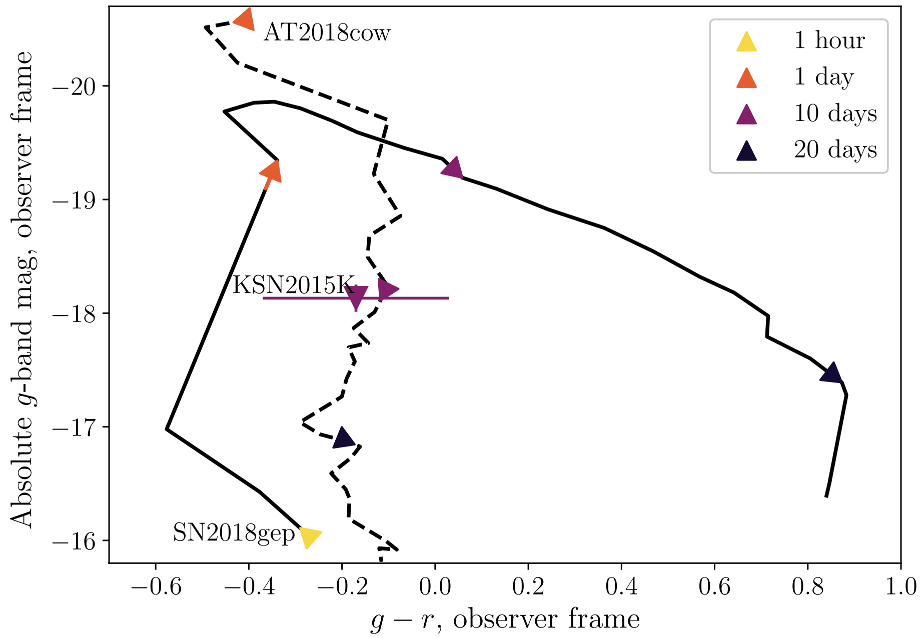

Figure 22. A "color-magnitude" diagram of AT2018cow and SN2018gep, showing the evolution of color with time from first light (t_0). Like AT2018cow, the fast transient KSN2015K stayed persistently blue even after it had faded to half-maximum. SN2018gep has more typical SN evolution, reddening with time (cooling in temperature).

In this paper, we presented an unprecedented dataset that connects the death throes of a stripped massive star to its subsequent explosion as a core-collapse supernova (SN). We argue that the data is best described by eruptive mass-loss episodes in the months before terminal explosion, which produced extended circumstellar material (CSM). The light curve was powered by shock breakout into this CSM, followed by cooling of the shock-heated material. Here we summarize our key findings.

1. High-cadence dual-band observations with ZTF (six observations in 3 hours) captured a rapid rise (1.3 mag/hr) to peak luminosity, and a corresponding increase in temperature. This rise rate is second only to that of SN 2016gkg (Bersten et al. 2018), which was attributed to shock breakout in extended material surrounding a Type IIb progenitor. However, the signal in SN2018gep is two magnitudes more luminous.

2. A retrospective search in ZTF data revealed clear detections of precursor emission in the days and months leading up to the terminal explosion. The luminosity of these detections ($M = -14$) and evidence for variability suggests that they arise from eruptive mass-loss, rather than the luminosity of a quiescent progenitor. This is the first definitive pre-explosion detection of a Ic-BL SN to date.

3. The bolometric light curve peaks after a few days at $> 3 \times 10^{44}\,\mathrm{erg\,s^{-1}}$. At late times, a power-law and an exponential decay are both acceptable fits to the data.

4. The temperature rises to $50,000\,\mathrm{K}$ in the first day, then declines as t^{-1} then flattens at $5000\,\mathrm{K}$, which we attribute to recombination of carbon and oxygen.

5. The photosphere expands at $v = 0.1c$, and flattens once recombination sets in.

6. We obtained nine spectra in the first five days of the explosion, as the effective temperature declined from 50,000 K to 20,000 K. To our knowledge, these represent the earliest-ever spectra of a stripped-envelope SN, in terms of temperature evolution.

7. The early spectra exhibit a "W" feature similar to what has been seen in stripped-envelope superluminous SNe. From a NLTE spectral synthesis model, we find that this can be reproduced with a carbon and oxygen composition.

8. The velocities inferred from the spectra are among the highest observed for stripped-envelope SNe, and are most similar to the velocities of Ic-BL SNe accompanied by GRBs.

9. The host galaxy has a star-formation rate of $0.12\,M_\odot\,\mathrm{yr}^{-1}$, and a lower mass and lower metallicity than galaxies hosting GRB-SNe, which are low-mass and low-metallicity compared to the overall CC SN population.

10. The early light curve is best-described by shock breakout in extended but confined CSM, with $M = 0.02\,M_\odot$ at $R = 3 \times 10^{14}\,\mathrm{cm}$. The implied mass-loss rate is $0.6\,M_\odot\,\mathrm{yr}^{-1}$ in the days leading up to the explosion, consistent with our detections of precursor emission. After the initial breakout, the shock runs through CSM of much lower density, hence the lack of narrow emission features and lack of strong radio and X-ray emission.

11. Although SN2018gep is similar to AT2018cow in terms of its bolometric light curve, it has a very different color evolution. In this sense, the "rapidly evolving transients" in the PS-1 and DES samples are more similar to SN2018gep than to AT2018cow.

12. The late-time light curve seems to require an energy deposition mechanism distinct from shock-interaction. Radioactive decay is one possibility, but further monitoring is needed to test this.

The code used to produce the results described in this paper was written in Python and is available online in an open-source repository[13].

[13] https://github.com/annayqho/SN2018gep

It is a pleasure to thank Tony Piro, Dan Kasen, E. Sterl Phinney, Eliot Quataert, Maryam Modjaz, Jim Fuller, Lars Bildsten, Paul Duffell, and Luc Dessart for helpful discussions. A.Y.Q.H. is particularly grateful to Tony Piro and the community at Carnegie Observatories for their hospitality on Tuesdays during the period in which this work was performed. Thank you to the staff at the SMA, AMI, the VLA, *Swift*, and Chandra for rapidly scheduling and executing the observations. Thank you to David Palmer (LANL) for his assistance in searching the pointing data for *Swift*/BAT. Thank you to Michael J. Koss (Eureka Scientific Int), Andrew Drake (Caltech), Scott Adams (Caltech), Matt Hankins (Caltech), Kevin Burdge (Caltech), and Kirsty Taggart (LJMU) for assisting with optical spectroscopic observations. Thank you to Erik Petigura and David Hogg for their advice on figure aesthetics.

A.Y.Q.H. is supported by a National Science Foundation Graduate Research Fellowship under Grant No. DGE1144469. This work was supported by the GROWTH project funded by the National Science Foundation under PIRE Grant No. 1545949. Y.T. studied as a GROWTH intern at Caltech during the summer and fall of 2017. C.C.N. thanks the funding from MOST grant 104-2923-M-008 -004-MY5. R.L. is supported by a Marie Skłodowska-Curie Individual Fellowship within the Horizon 2020 European Union (EU) Framework Programme for Research and Innovation (H2020-MSCA-IF-2017-794467). A.H. acknowledges support by the I-Core Program of the Planning and Budgeting Committee and the Israel Science Foundation, and support by the ISF grant 647/18. This research was supported by a Grant from the GIF, the German-Israeli Foundation for Scientific Research and Development. This research was funded in part by the Gordon and Betty Moore Foundation through Grant GBMF5076, and a grant from the Heising-Simons Foundation. A.C. acknowledges support from the NSF CAREER award N. 1455090 and from the NASA/Chandra GI award N. GO8-19055A. Research support to I.A. is provided by the GROWTH project, funded by the National Science Foundation under Grant No 1545949.

Based on observations obtained with the Samuel Oschin Telescope 48-inch and the 60-inch Telescope at the Palomar Observatory as part of the Zwicky Transient Facility project. Major funding has been provided by the U.S National Science Foundation under Grant No. AST-1440341 and by the ZTF partner institutions: the California Institute of Technology, the Oskar Klein Centre, the Weizmann Institute of Science, the University of Maryland, the University of Washington, Deutsches Elektronen-Synchrotron, the University of Wisconsin-Milwaukee, and the TANGO Program of the University System of Taiwan. Partially based on observations made with the Nordic Optical Telescope, operated by the Nordic Optical Telescope Scientific Association at the Observatorio del Roque de los Muchachos, La Palma, Spain, of the Instituto de Astrofisica de Canarias. The Liverpool Telescope is operated by Liverpool John Moores University with financial support from the UK Science and Technology Facilities Council. LT is located on the island of La Palma, in the Spanish Observatorio del Roque de los Muchachos of the Instituto de Astrofisica de Canarias. The scientific results reported in this article are based in part on observations made by the Chandra X-ray Observatory. The data presented here were obtained in part with ALFOSC, which is provided by the Instituto de Astrofisica de Andalucia (IAA) under a joint agreement with the University of Copenhagen and NOTSA. The Submillimeter Array is a joint project between the Smithsonian Astrophysical Observatory and the Academia Sinica Institute of Astronomy and Astrophysics and is funded by the Smithsonian Institution and the Academia Sinica. We acknowledge the support of the staff of the Xinglong 2.16-m telescope. This work is supported by the National Natural Science Foundation of China (NSFC grants 11325313 and 11633002), and the National Program on Key Research and Development Project (grant no. 2016YFA0400803). SED Machine is based upon work supported by the National Science Foundation under Grant No. 1106171. This publication has made use of data collected at Lulin Observatory, partly supported by MoST grant 105-2112-M-008-024-MY3.

Software: `Astropy` (Astropy Collaboration et al. 2013, 2018), `IPython` (Pérez & Granger 2007), `matplotlib` (Hunter 2007), `numpy` (Oliphant 2006), `scipy` (Jones et al. 2001), `extinction` (Barbary et al. 2016)

Facilities: CFHT, Keck:I (LRIS), Hale (DBSP), AMI, Liverpool:2m (IO:O, SPRAT), DCT, Swift (UVOT, XRT), Beijing:2.16m, EVLA, SMA, LO:1m, NOT (ALFOSC)

REFERENCES

Ahn, C. P., Alexandroff, R., Allende Prieto, C., et al. 2014, ApJS, 211, 17

Ahn, C. P., Alexandroff, R., Allende Prieto, C., et al. 2012, ApJS, 203, 21.

Almgren, A. S., Beckner, V. E., Bell, J. B., et al. 2010, ApJ, 715, 1221

Arcavi, I., Wolf, W. M., Howell, D. A., et al. 2016, ApJ, 819, 35

Arnett, W. D. 1979, ApJL, 230, L37

Arnouts, S., Cristiani, S., Moscardini, L., et al. 1999, MNRAS, 310, 540

Asplund, M., Grevesse, N., Sauval, A. J., & Scott, P. 2009, ARA&A, 47, 481

Astropy Collaboration, Robitaille, T. P., Tollerud, E. J., et al. 2013, A&A, 558, A33

Astropy Collaboration, Price-Whelan, A. M., Sipőcz, B. M., et al. 2018, AJ, 156, 123

Barbary, K. 2016, extinction, v0.3.0, Zenodo, doi: 10.5281/zenodo.804967, https://github.com/kbarbary/extinction

Barnes, J., Duffell, P. C., Liu, Y., et al. 2018, ApJ, 860, 38

Barthelmy, S. D., Barbier, L. M., Cummings, J. R., et al. 2005, SSRv, 120, 143

Bellm, E. C., Kulkarni, S. R., Graham, M. J., et al. 2019, PASP, 131, 018002

Bellm, E. C., et al. 2019, PASP submitted

Ben-Ami, S., Gal-Yam, A., Filippenko, A. V., et al. 2012, ApJL, 760, L33

Berger, E., Leibler, C. N., Chornock, R., et al. 2013, ApJ, 779, 18

Bersier, D., Fruchter, A. S., Strolger, L.-G., et al. 2006, ApJ, 643, 284

Bersten, M. C., Folatelli, G., García, F., et al. 2018, Nature, 554, 497

Bertin, E. 2010, Astrophysics Source Code Library, ascl:1010.068

Narayana Bhat, P., Meegan, C. A., von Kienlin, A., et al. 2016, The Astrophysical Journal Supplement Series, 223, 28.

Blackburn, L., Briggs, M. S., Camp, J., et al. 2015, The Astrophysical Journal Supplement Series, 217, 8.
Blagorodnova, N., Neill, J. D., Walters, R., et al. 2018, PASP, 130, 035003
Blanton, M. R., & Roweis, S. 2007, AJ, 133, 734
Blaufuss, E. 2018, The Astronomer's Telegram, 12062,
Bourne, N., Maddox, S. J., Dunne, L., et al. 2012, MNRAS, 421, 3027
Branch, D., Benetti, S., Kasen, D., et al. 2002, ApJ, 566, 1005
Breeveld, A. A., Landsman, W., Holland, S. T., et al. 2011, American Institute of Physics Conference Series, 373
Bromberg, O., Nakar, E., Piran, T., & Sari, R. 2011, ApJ, 740, 100
Bruzual, G., & Charlot, S. 2003, MNRAS, 344, 1000
Bufano, F., Pian, E., Sollerman, J., et al. 2012, ApJ, 753, 67
Calzetti, D., Armus, L., Bohlin, R. C., et al. 2000, ApJ, 533, 682
Campana, S., Mangano, V., Blustin, A. J., et al. 2006, Nature, 442, 1008
Cano, Z. 2013, MNRAS, 434, 1098
Cano, Z., Wang, S.-Q., Dai, Z.-G., & Wu, X.-F. 2017, Advances in Astronomy, 2017, 8929054
Cano, Z., Izzo, L., de Ugarte Postigo, A., et al. 2017, A&A, 605, A107
Cenko, S. B., Fox, D. B., Moon, D.-S., et al. 2006, PASP, 118, 1396
Cenko, S. B., Kulkarni, S. R., Horesh, A., et al. 2013, ApJ, 769, 130
Cenko, S. B., Urban, A. L., Perley, D. A., et al. 2015, ApJL, 803, L24
Chabrier, G. 2003, PASP, 115, 763
Chambers, K. C., Magnier, E. A., Metcalfe, N., et al. 2016, arXiv:1612.05560
Chevalier, R. A. 1976, ApJ, 207, 872
Chevalier, R. A., & Fransson, C. 1994, ApJ, 420, 268
Chevalier, R. A. 1998, ApJ, 499, 810
Chevalier, R. A., & Irwin, C. M. 2011, ApJL, 729, L6
Colgate, S. A., & McKee, C. 1969, ApJ, 157, 623
Colgate, S. A. 1974, ApJ, 187, 333
Costantin, L., Avramova-Bonche, A., Pinter, V., et al. 2018, The Astronomer's Telegram, 12047,
Corsi, A., Cenko, S. B., Kasliwal, M. M., et al. 2017, ApJ, 847, 54.
Corsi, A., Ofek, E. O., Gal-Yam, A., et al. 2014, ApJ, 782, 42
Corsi, A., Ofek, E. O., Gal-Yam, A., et al. 2012, ApJL, 747, L5
Cutri, R. M., Wright, E. L., Conrow, T., et al. 2013, Explanatory Supplement to the AllWISE Data Release Products
De, K., Kasliwal, M. M., Ofek, E. O., et al. 2018, Science, 362, 201
Dekany, R., Smith, R. M., Belicki, J., et al. 2016, Proc. SPIE, 9908, 99085M
D'Elia, V., Campana, S., D'Aì, A., et al. 2018, A&A, 619, A66
Dessart, L., John Hillier, D., Yoon, S.-C., Waldman, R., & Livne, E. 2017, A&A, 603, A51
Dessart, L. 2018, A&A, in press, arXiv:1812.03749
Drout, M. R., Chornock, R., Soderberg, A. M., et al. 2014, ApJ, 794, 23
Ergon, M., Fransson, C., et al. 2018, A&A, 620, A156
Evans, P. A., Beardmore, A. P., Page, K. L., et al. 2009, MNRAS, 397, 1177
Fitzpatrick, E. L. 1999, PASP, 111, 63
Flewelling, H. A., Magnier, E. A., Chambers, K. C., et al. 2016, arXiv:1612.05243
Foley, R. J., Papenkova, M. S., Swift, B. J., et al. 2003, PASP, 115, 1220
Foley, R. J., Smith, N., Ganeshalingam, M., et al. 2007, ApJL, 657, L105
Fox, O. D., & Smith, N. 2019, arXiv:1903.01535
Fremling, C. 2018, The Astronomer's Telegram, 11738,
Fremling, C., Sollerman, J., Taddia, F., et al. 2016, Å, 593A, 68F
Galama, T. J., Vreeswijk, P. M., van Paradijs, J., et al. 1998, Nature, 395, 670
Gal-Yam, A. 2018, arXiv:1806.08224
Gal-Yam, A. 2018, arXiv:1812.01428

Garmire, G. P., Bautz, M. W., Ford, P. G., Nousek, J. A., & Ricker, G. R., Jr. 2003, Proc. SPIE, 4851, 28
Gehrels, N., Chincarini, G., Giommi, P., et al. 2004, ApJ, 611, 1005
Goldstein, A., Burns, E., Hamburg, R., et al. 2016, arXiv e-prints , arXiv:1612.02395.
Gorosabel, J., Pérez-Ramírez, D., Sollerman, J., et al. 2005, A&A, 444, 711
Graham, M. J., Kulkarni, S. R., Bellm, E. C., et al. 2019, arXiv:1902.01945
Grassberg, E. K., Imshennik, V. S., & Nadyozhin, D. K. 1971, Ap&SS, 10, 28
Groh, J. H., Meynet, G., Georgy, C., & Ekström, S. 2013, A&A, 558, A131
Gruber, D., Goldstein, A., Weller von Ahlefeld, V., et al. 2014, The Astrophysical Journal Supplement Series, 211, 12.
Gruen, D., Seitz, S., & Bernstein, G. M. 2014, Publications of the Astronomical Society of the Pacific, 126, 158.
Han, X. H., Hammer, F., Liang, Y. C., et al. 2010, A&A, 514, A24
Hickish, J., Razavi-Ghods, N., Perrott, Y. C., et al. 2018, MNRAS, 475, 5677
Hjorth, J., Malesani, D., Jakobsson, P., et al. 2012, ApJ, 756, 187
Hjorth, J., & Bloom, J. S. 2012, Chapter 9 in "Gamma-Ray Bursts", Cambridge Astrophysics Series 51, eds. C. Kouveliotou, R. A. M. J. Wijers and S. Woosley, Cambridge University Press (Cambridge), p. 169-190, 169
Ho, A. Y. Q., Ness, M. K., Hogg, D. W., et al. 2017, ApJ, 836, 5
Ho, A. Y. Q., Kulkarni, S. R., Nugent, P. E., et al. 2018, ApJL, 854, L13
Ho, A. Y. Q., Schulze, S., Perley, D. A., et al. 2018, The Astronomer's Telegram, 12030,
Ho, A. Y. Q., Perley, D. A., Hallinan, G., et al. 2018, The Astronomer's Telegram, 12056,
Ho, A. Y. Q., Phinney, E. S., Ravi, V., et al. 2019, ApJ, 871, 73
Ho, P. T. P., Moran, J. M., & Lo, K. Y. 2004, ApJL, 616, L1
Högbom, J. A. 1974, A&AS, 15, 417
Howell, D. A., Kasen, D., Lidman, C., et al. 2013, ApJ, 779, 98
Hudelot, P., Cuillandre, J.-C., Withington, K., et al. 2012, VizieR Online Data Catalog, 2317,
Hunter, J. D. 2007, CISE, 9(3), 90
Hurley, K., Golenetskii, S., Aptekar, R., et al. 2010, American Institute of Physics Conference Series, 1279, 330
Ilbert, O., Arnouts, S., McCracken, H. J., et al. 2006, A&A, 457, 841
Immler, S., Modjaz, M., Landsman, W., et al. 2008, ApJL, 674, L85
Izotov, Y. I., Stasińska, G., Meynet, G., Guseva, N. G., & Thuan, T. X. 2006, A&A, 448, 955
Izzo, L., Thöne, C. C., Schulze, S., et al. 2017, MNRAS, 472, 4480
Izzo, L., de Ugarte Postigo, A., Maeda, K., et al. 2019, Nature, 565, 324
Jones, E., Oliphant, E., Peterson, P. et al. 2001, http://www.scipy.org/
Kasen, D., Metzger, B. D., & Bildsten, L. 2016, ApJ, 821, 36
Kasen, D. 2017, Handbook of Supernovae, ISBN 978-3-319-21845-8. Springer International Publishing AG, 2017, p. 939, 939
Kasen, D., & Bildsten, L. 2010, ApJ, 717, 245
Kasliwal, M. M., Cannella, C., Bagdasaryan, A., et al. 2019, PASP, 131, 038003
Kennicutt, R. C., Jr. 1998, ARA&A, 36, 189
Kasliwal, M. M. 2011, Ph.D. Thesis,
Katz, B., Kushnir, D., & Dong, S. 2013, arXiv:1301.6766
Kauffmann, G., Heckman, T. M., Tremonti, C., et al. 2003, MNRAS, 346, 1055.
Kewley, L. J., Dopita, M. A., Sutherland, R. S., et al. 2001, ApJ, 556, 121.
Khatami, D. K., & Kasen, D. N. 2018, arXiv:1812.06522
Kocevski, D., Modjaz, M., Bloom, J. S., et al. 2007, ApJ, 663, 1180
Krühler, T., Malesani, D., Fynbo, J. P. U., et al. 2015, A&A, 581, A125

Kuin N. P. M., et al., 2015, MNRAS 449, 2514
Kuin, N. P. M., Wu, K., Oates, S., et al. 2018, arXiv:1808.08492
Kulkarni, S. R., Frail, D. A., Wieringa, M. H., et al. 1998, Nature, 395, 663
Laskar, T., Coppejans, D. L., Margutti, R., & Alexander, K. D. 2017, GRB Coordinates Network, Circular Service, No. 22216, #1 (2017), 22216, 1
Law, N. M., Kulkarni, S. R., Dekany, R. G., et al. 2009, Publications of the Astronomical Society of the Pacific, 121, 1395.
Levesque, E. M., Kewley, L. J., Graham, J. F., & Fruchter, A. S. 2010, ApJL, 712, L26
Lupton, R., Blanton, M. R., Fekete, G., et al. 2004, Publications of the Astronomical Society of the Pacific, 116, 133.
Luridiana, V., Morisset, C., & Shaw, R. A. 2015, A&A, 573, A42
Lyman, J. D., Bersier, D., James, P. A., et al. 2016, MNRAS, 457, 328
Lyutikov, M., & Toonen, S. 2018, arXiv:1812.07569
Madau, P., & Dickinson, M. 2014, Annual Review of Astronomy and Astrophysics, 52, 415
Malesani, D., Tagliaferri, G., Chincarini, G., et al. 2004, ApJL, 609, L5
Mannucci, F., Cresci, G., Maiolino, R., Marconi, A., & Gnerucci, A. 2010, MNRAS, 408, 2115
Margutti, R., Chincarini, G., Covino, S., et al. 2007, A&A, 474, 815
Margutti, R., Soderberg, A. M., Wieringa, M. H., et al. 2013, ApJ, 778, 18
Margutti, R., Milisavljevic, D., Soderberg, A. M., et al. 2014, ApJ, 797, 107
Margutti, R., Guidorzi, C., Lazzati, D., et al. 2015, ApJ, 805, 159
Margutti, R., Metzger, B. D., Chornock, R., et al. 2019, ApJ, 872, 18
Marino, R. A., Rosales-Ortega, F. F., Sánchez, S. F., et al. 2013, A&A, 559, A114.
Martin, D. C., Fanson, J., Schiminovich, D., et al. 2005, ApJL, 619, L1
Masci, F. J., Laher, R. R., Rusholme, B., et al. 2019, PASP, 131, 018003
Matzner, C. D., & McKee, C. F. 1999, ApJ, 510, 379
Mazzali, P. A., Sullivan, M., Pian, E., et al. 2016, MNRAS, 458, 3455
McMullin, J. P., Waters, B., Schiebel, D., Young, W., & Golap, K. 2007, Astronomical Data Analysis Software and Systems XVI, 376, 127
Meegan, C., Lichti, G., Bhat, P. N., et al. 2009, ApJ, 702, 791
Mereghetti, S., Götz, D., Borkowski, J., et al. 2003, A&A, 411, L291.
Michałowski, M. J., Hjorth, J., Malesani, D., et al. 2009, ApJ, 693, 347
Modjaz, M., Li, W., Butler, N., et al. 2009, ApJ, 702, 226
Modjaz, M., Liu, Y. Q., Bianco, F. B., & Graur, O. 2016, ApJ, 832, 108
Modjaz, M., Bianco, F. B., Siwek, M., et al. 2019, arXiv:1901.00872
Moriya, T. J., & Tominaga, N. 2012, ApJ, 747, 118
Moriya, T. J., Chen, T.-W., & Langer, N. 2017, ApJ, 835, 177
Moriya, T. J., Sorokina, E. I., & Chevalier, R. A. 2018, SSRv, 214, 59
Murphy, E. J., Condon, J. J., Schinnerer, E., et al. 2011, ApJ, 737, 67
Nakar, E., & Piro, A. L. 2014, ApJ, 788, 193
Nakar, E., & Sari, R. 2010, ApJ, 725, 904
Nakar, E. 2015, ApJ, 807, 172
Nicholl, M., Smartt, S. J., Jerkstrand, A., et al. 2013, Nature, 502, 346
Ofek, E. O., Sullivan, M., Shaviv, N. J., et al. 2014, ApJ, 789, 104
Ofek, E. O., Rabinak, I., Neill, J. D., et al. 2010, ApJ, 724, 1396
Oke, J. B., & Gunn, J. E. 1982, PASP, 94, 586
Oke, J. B., Cohen, J. G., Carr, M., et al. 1995, PASP, 107, 375
Oliphant, T. E. 2006, *A guide to NumPy*, Trelgol Publishing

Osterbrock, D. E., & Ferland, G. J. 2006, Astrophysics of gaseous nebulae and active galactic nuclei, 2nd. ed. by D.E. Osterbrock and G.J. Ferland. Sausalito, CA: University Science Books, 2006,

Ovaldsen, J.-E., Jaunsen, A. O., Fynbo, J. P. U., et al. 2007, ApJ, 662, 294

Pastorello, A., Smartt, S. J., Mattila, S., et al. 2007, Nature, 447, 829

Pérez, F. & Granger, B. E. 2007, CISE, 9(3), 29

Perley, D. A., Mazzali, P. A., Yan, L., et al. 2019, MNRAS, 484, 1031

Perley, D. A. 2019, arXiv e-prints , arXiv:1903.07629.

Perrott, Y. C., Scaife, A. M. M., Green, D. A., et al. 2013, MNRAS, 429, 3330

Pettini, M., & Pagel, B. E. J. 2004, MNRAS, 348, L59.

Piascik, A. S., Steele, I. A., Bates, S. D., et al. 2014, Proc. SPIE, 9147, 91478H

Piran, T. 2004, Reviews of Modern Physics, 76, 1143

Piro, A. L. 2015, ApJL, 808, L51

Planck Collaboration, Ade, P. A. R., Aghanim, N., et al. 2016, A&A, 594, A13.

Poznanski, D., Chornock, R., Nugent, P. E., et al. 2010, Science, 327, 58

Prentice, S. J., Mazzali, P. A., Pian, E., et al. 2016, MNRAS, 458, 2973

Prentice, S. J., Maguire, K., Smartt, S. J., et al. 2018, ApJL, 865, L3

Pursiainen, M., Childress, M., Smith, M., et al. 2018, MNRAS, 481, 894.

Quimby, R. M., De Cia, A., Gal-Yam, A., et al. 2018, ApJ, 855, 2

Quimby, R. M., Kulkarni, S. R., Kasliwal, M. M., et al. 2011, Nature, 474, 487

Rabinak, I., & Waxman, E. 2011, ApJ, 728, 63

Rest, A., Garnavich, P. M., Khatami, D., et al. 2018, Nature Astronomy, 2, 307

Roming, P. W. A., Kennedy, T. E., Mason, K. O., et al. 2005, SSRv, 120, 95

Sapir, N., & Waxman, E. 2017, ApJ, 838, 130

Sault, R. J., Teuben, P. J., & Wright, M. C. H. 1995, Astronomical Data Analysis Software and Systems IV, 77, 433

Schlafly, E. F., & Finkbeiner, D. P. 2011, ApJ, 737, 103

Schlegel, E. M. 1990, MNRAS, 244, 269

Schulze, S., Ho, A. Y. Q., & Mill, A. A. 2018, The Astronomer's Telegram, 12032,

Schulze, S., Krühler, T., Leloudas, G., et al. 2018, MNRAS, 473, 1258

Schulze, S., Malesani, D., Cucchiara, A., et al. 2014, A&A, 566, A102

Shivvers, I., Zheng, W. K., Mauerhan, J., et al. 2016, MNRAS, 461, 3057

Skrutskie, M. F., Cutri, R. M., Stiening, R., et al. 2006, AJ, 131, 1163

Smartt, S. J., Clark, P., Smith, K. W., et al. 2018, The Astronomer's Telegram, 11727,

Smith, N. 2014, Annual Review of Astronomy and Astrophysics, 52, 487.

Soderberg, A. M., Kulkarni, S. R., Berger, E., et al. 2004, Nature, 430, 648

Soderberg, A. 2006, The Astronomer's Telegram, 917,

Soderberg, A. M., Kulkarni, S. R., Nakar, E., et al. 2006, Nature, 442, 1014

Soderberg, A. M., Chakraborti, S., Pignata, G., et al. 2010, Nature, 463, 513

Stalder, B., Tonry, J., Smartt, S. J., et al. 2017, arXiv:1706.00175

Stanway, E. R., Levan, A. J., Tanvir, N., et al. 2015, MNRAS, 446, 3911

Starling, R. L. C., Wiersema, K., Levan, A. J., et al. 2011, MNRAS, 411, 2792

Steele, I. A., Smith, R. J., Rees, P.-C., et al. 2004, SPIE, 5489, 679S

Strotjohann, N. L., Ofek, E. O., Gal-Yam, A., et al. 2015, ApJ, 811, 117.

Taddia, F., Sollerman, J., Fremling, C., et al. 2019, A&A, 621, A71

Tanaka, M., Tominaga, N., Morokuma, T., et al. 2016, ApJ, 819, 5.

Thöne, C. C., Fynbo, J. P. U., Östlin, G., et al. 2008, ApJ, 676, 1151

Thöne, C. C., Christensen, L., Prochaska, J. X., et al. 2014, MNRAS, 441, 2034

Tonry, J. L., Denneau, L., Heinze, A. N., et al. 2018, PASP, 130, 064505

Toy, V. L., Cenko, S. B., Silverman, J. M., et al. 2016, ApJ, 818, 79

Van der Walt, S. J., Crellin-Quick, A., Bloom, J. S., JOSS, 28a83ab, submitted, 2019

Van Dyk, S. D. 2017, Philosophical Transactions of the Royal Society of London Series A, 375, 20160277

Van Dyk, S. D., Zheng, W., Brink, T. G., et al. 2018, ApJ, 860, 90

von Kienlin, A., Meegan, C. A., Paciesas, W. S., et al. 2014, The Astrophysical Journal Supplement Series, 211, 13.

Wang, J., Xin, L., Ren, J., et al. 2018, The Astronomer's Telegram, 12055,

Whitesides, L., Lunnan, R., Kasliwal, M. M., et al. 2017, ApJ, 851, 107

Woosley, S. E. 2010, ApJL, 719, L204

Woosley, S. E., Heger, A. 2007, Phys. Rep., 442, 269

Wright, E. L., Eisenhardt, P. R. M., Mainzer, A. K., et al. 2010, AJ, 140, 1868

Wright, A. H., Robotham, A. S. G., Bourne, N., et al. 2016, MNRAS, 460, 765

Wygoda, N., Elbaz, Y., & Katz, B. 2019, MNRAS, 484, 3941

Yan, L., Quimby, R., Gal-Yam, A., et al. 2017, ApJ, 840, 57

Yaron, O., Perley, D. A., Gal-Yam, A., et al. 2017, Nature Physics, 13, 510.

Zackay, B., Ofek, E. O., & Gal-Yam, A. 2016, ApJ, 830, 27

Zhang, W., Howell, L., Almgren, A., Burrows, A., & Bell, J. 2011, ApJS, 196, 20

Zwart, J. T. L., Barker, R. W., Biddulph, P., et al. 2008, MNRAS, 391, 1545

APPENDIX

A. UV AND OPTICAL PHOTOMETRY

In Figure 23 we show the photometry interpolated onto common epochs, and fit to a blackbody function to derive the photospheric evolution (Section 3). The full set of photometry is listed in Table 5.

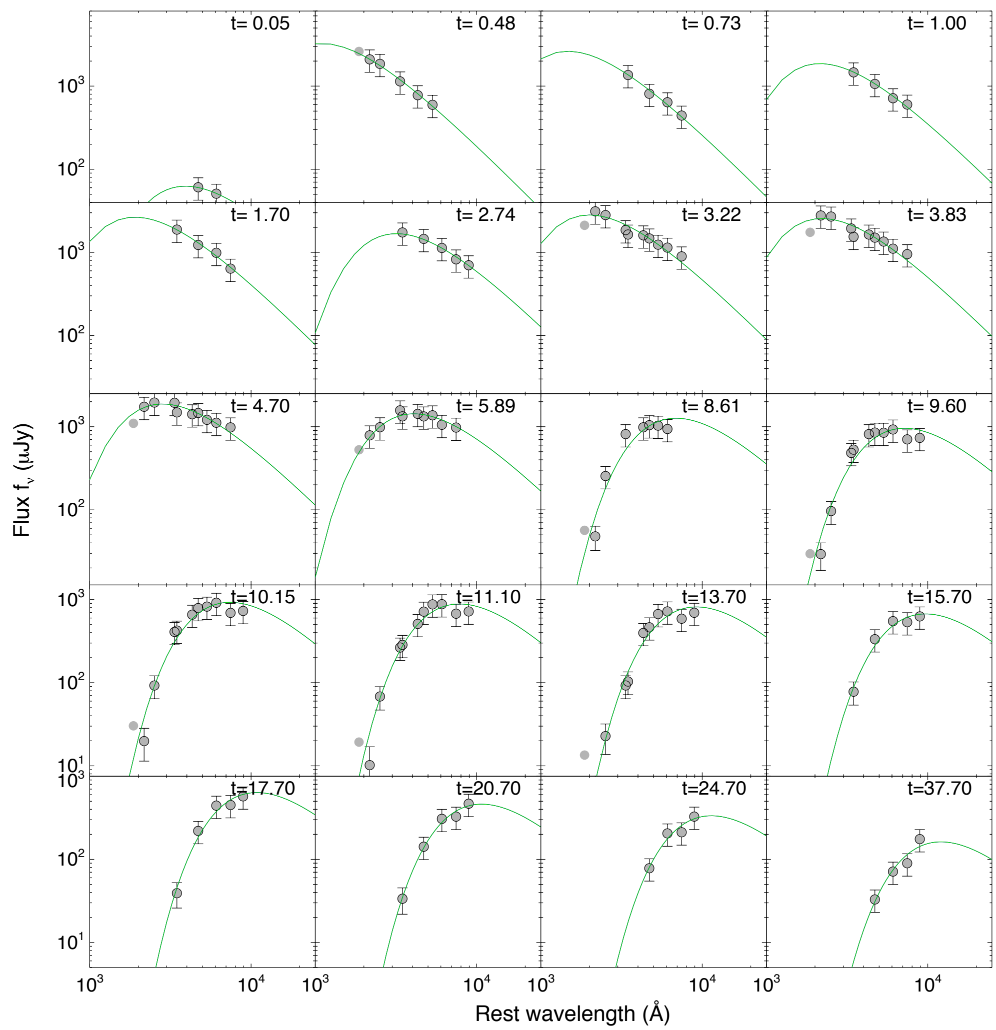

Figure 23. Blackbody fits to *Swift*/UVOT and optical photometry for SN2018gep. Since the UVOT and ground-based observations were taken at slightly different epochs, we interpolated the data in time using UVOT epochs at early times and LT epochs at later times.

Table 5. Optical and ultraviolet photometry for SN2018gep

Date (JD)	Δt	Instrument	Filter	AB Mag	Error in AB Mag
2458370.6634	0.02	P48+ZTF	r	20.5	0.3
2458370.6856	0.04	P48+ZTF	g	19.7	0.1
2458370.6994	0.05	P48+ZTF	g	19.3	0.1
2458370.7153	0.07	P48+ZTF	g	18.8	0.1
2458370.7612	0.11	P48+ZTF	r	18.4	0.1
2458370.7612	0.11	P48+ZTF	r	18.4	0.1
2458371.6295	0.98	P60+SEDM	r	16.8	0.0
2458371.6323	0.99	P60+SEDM	g	16.4	0.0
2458371.6351	0.99	P60+SEDM	i	17.0	0.0
2458371.6369	0.99	P48+ZTF	r	16.8	0.0
2458371.6378	0.99	P48+ZTF	r	16.8	0.0
2458371.6378	0.99	P48+ZTF	r	16.8	0.0
2458371.6392	0.99	P60+SEDM	u	16.0	0.0
2458371.642	0.99	P60+SEDM	r	16.8	0.0
2458371.6448	1.0	P60+SEDM	g	16.4	0.0
2458371.6476	1.0	P60+SEDM	i	17.0	0.0
2458371.6514	1.0	P48+ZTF	r	16.8	0.0
2458371.6517	1.0	P60+SEDM	u	16.0	0.0
2458371.6838	1.04	P48+ZTF	r	16.8	0.0
2458371.6959	1.05	P48+ZTF	g	16.3	0.0
2458371.6968	1.05	P48+ZTF	g	16.3	0.0
2458371.6968	1.05	P48+ZTF	g	16.3	0.0
2458371.7138	1.07	P48+ZTF	g	16.3	0.0
2458371.7138	1.07	P48+ZTF	g	16.3	0.0
2458371.7359	1.09	P48+ZTF	g	16.3	0.0
2458372.6396	1.99	P48+ZTF	r	16.5	0.0
2458372.6396	1.99	P48+ZTF	r	16.5	0.0
2458372.6586	2.01	P48+ZTF	r	16.5	0.1
2458372.6586	2.01	P48+ZTF	r	16.5	0.1
2458372.6861	2.04	P48+ZTF	r	16.5	0.0
2458372.6861	2.04	P48+ZTF	r	16.5	0.0
2458372.7134	2.07	P48+ZTF	g	16.0	0.0
2458372.7371	2.09	P48+ZTF	g	16.0	0.0
2458372.7371	2.09	P48+ZTF	g	16.0	0.0
2458373.6276	2.98	P48+ZTF	r	16.4	0.0
2458373.6447	3.0	P60+SEDM	r	16.3	0.0
2458373.6464	3.0	P60+SEDM	g	16.0	0.0
2458373.6481	3.0	P60+SEDM	i	16.6	0.0
2458373.6498	3.0	P60+SEDM	u	15.9	0.0
2458373.6627	3.02	P48+ZTF	r	16.4	0.0
2458373.6627	3.02	P48+ZTF	r	16.4	0.0
2458373.685	3.04	P48+ZTF	r	16.3	0.0
2458373.685	3.04	P48+ZTF	r	16.3	0.0

Table 5 continued on next page

Table 5 *(continued)*

Date (JD)	Δt	Instrument	Filter	AB Mag	Error in AB Mag
2458373.6984	3.05	P48+ZTF	g	15.9	0.0
2458373.7189	3.07	P48+ZTF	g	15.9	0.0
2458373.736	3.09	P48+ZTF	g	15.9	0.0
2458374.6316	3.98	P48+ZTF	r	16.3	0.0
2458374.6316	3.98	P48+ZTF	r	16.3	0.0
2458374.6429	4.0	P48+ZTF	r	16.3	0.0
2458374.6495	4.0	P48+ZTF	r	16.3	0.0
2458374.6551	4.01	P60+SEDM	r	16.3	0.0
2458374.6569	4.01	P60+SEDM	g	16.0	0.0
2458374.6586	4.01	P60+SEDM	i	16.4	0.0
2458374.6603	4.01	P60+SEDM	u	15.9	0.0
2458374.6845	4.04	P48+ZTF	r	16.3	0.0
2458374.6845	4.04	P48+ZTF	r	16.3	0.0
2458374.6994	4.05	P48+ZTF	g	15.9	0.0
2458374.6994	4.05	P48+ZTF	g	15.9	0.0
2458374.7041	4.06	P48+ZTF	g	15.9	0.0
2458374.7264	4.08	P48+ZTF	g	15.9	0.0
2458374.7428	4.1	P48+ZTF	g	15.9	0.0
2458374.7428	4.1	P48+ZTF	g	15.9	0.0
2458375.6247	4.98	P60+SEDM	r	16.3	0.0
2458375.6265	4.98	P60+SEDM	g	16.1	0.0
2458375.6282	4.98	P60+SEDM	i	16.4	0.0
2458375.6299	4.98	P60+SEDM	u	16.0	0.0
2458375.6757	5.03	P48+ZTF	r	16.3	0.0
2458375.6757	5.03	P48+ZTF	r	16.3	0.0
2458375.7144	5.07	P48+ZTF	g	16.0	0.0
2458375.7144	5.07	P48+ZTF	g	16.0	0.0
2458375.7381	5.09	P48+ZTF	g	16.0	0.0
2458376.62	5.97	P48+ZTF	r	16.4	0.0
2458376.6623	6.02	P60+SEDM	r	16.4	0.0
2458376.6626	6.02	P48+ZTF	r	16.4	0.0
2458376.664	6.02	P60+SEDM	g	16.2	0.0
2458376.6657	6.02	P60+SEDM	i	16.4	0.0
2458376.6674	6.02	P60+SEDM	u	16.1	0.0
2458376.6739	6.03	P48+ZTF	r	16.4	0.0
2458376.7272	6.08	P48+ZTF	g	16.1	0.0
2458376.7272	6.08	P48+ZTF	g	16.1	0.0
2458376.7423	6.1	P48+ZTF	g	16.1	0.0
2458376.7423	6.1	P48+ZTF	g	16.1	0.0
2458377.6186	6.97	P60+SEDM	r	16.4	0.0
2458377.6204	6.97	P60+SEDM	g	16.3	0.0
2458377.6221	6.97	P60+SEDM	i	16.5	0.0
2458377.6238	6.98	P60+SEDM	u	16.3	0.0

Table 5 continued on next page

Table 5 *(continued)*

Date (JD)	Δt	Instrument	Filter	AB Mag	Error in AB Mag
2458377.6301	6.98	P48+ZTF	r	16.4	0.0
2458377.6301	6.98	P48+ZTF	r	16.4	0.0
2458377.6513	7.0	P48+ZTF	r	16.4	0.0
2458377.6639	7.02	P48+ZTF	r	16.4	0.0
2458377.6639	7.02	P48+ZTF	r	16.4	0.0
2458377.6761	7.03	P48+ZTF	r	16.4	0.0
2458377.6761	7.03	P48+ZTF	r	16.4	0.0
2458377.6935	7.05	P48+ZTF	g	16.2	0.0
2458377.7038	7.06	P48+ZTF	g	16.2	0.0
2458377.7165	7.07	P48+ZTF	g	16.2	0.0
2458377.7165	7.07	P48+ZTF	g	16.2	0.0
2458377.7458	7.1	P48+ZTF	g	16.2	0.0
2458377.7458	7.1	P48+ZTF	g	16.2	0.0
2458378.6164	7.97	P48+ZTF	r	16.4	0.0
2458378.6437	8.0	P48+ZTF	r	16.5	0.0
2458378.665	8.02	P48+ZTF	g	16.3	0.0
2458378.665	8.02	P48+ZTF	g	16.3	0.0
2458378.6844	8.04	P48+ZTF	g	16.3	0.0
2458378.693	8.05	P60+SEDM	r	16.4	0.0
2458378.7039	8.06	P48+ZTF	g	16.3	0.0
2458378.7158	8.07	P48+ZTF	r	16.5	0.0
2458379.6623	9.02	P48+ZTF	g	16.4	0.0
2458379.6823	9.04	P48+ZTF	g	16.4	0.0
2458379.6823	9.04	P48+ZTF	g	16.4	0.0
2458379.6977	9.05	P48+ZTF	g	16.4	0.0
2458379.7176	9.07	P48+ZTF	r	16.5	0.0
2458379.7409	9.09	P48+ZTF	r	16.5	0.0
2458379.7577	9.11	P48+ZTF	r	16.5	0.0
2458380.6214	9.97	P48+ZTF	g	16.6	0.0
2458380.6251	9.98	P48+ZTF	g	16.7	0.0
2458380.6778	10.03	P48+ZTF	g	16.6	0.0
2458380.6778	10.03	P48+ZTF	g	16.6	0.0
2458381.6238	10.98	P48+ZTF	r	16.6	0.0
2458381.6289	10.98	P48+ZTF	r	16.6	0.0
2458381.659	11.01	P48+ZTF	r	16.6	0.0
2458381.6837	11.04	P48+ZTF	g	16.7	0.0
2458381.7053	11.06	P48+ZTF	g	16.7	0.0
2458381.7122	11.06	P48+ZTF	g	16.7	0.0
2458383.6141	12.97	P48+ZTF	r	16.7	0.0
2458383.6141	12.97	P48+ZTF	r	16.7	0.0
2458383.6342	12.99	P48+ZTF	r	16.7	0.0
2458383.6555	13.01	P48+ZTF	r	16.7	0.0
2458383.6829	13.04	P48+ZTF	g	17.0	0.1

Table 5 continued on next page

Table 5 *(continued)*

Date (JD)	Δt	Instrument	Filter	AB Mag	Error in AB Mag
2458383.6829	13.04	P48+ZTF	g	17.0	0.1
2458383.6838	13.04	P48+ZTF	g	17.0	0.0
2458383.6838	13.04	P48+ZTF	g	17.0	0.0
2458383.705	13.06	P48+ZTF	g	17.0	0.0
2458383.7143	13.07	P48+ZTF	g	17.0	0.0
2458383.7143	13.07	P48+ZTF	g	17.0	0.0
2458384.6451	14.0	P48+ZTF	r	16.8	0.0
2458384.6525	14.01	P48+ZTF	r	16.8	0.0
2458384.6741	14.03	P48+ZTF	r	16.8	0.0
2458384.717	14.07	P48+ZTF	g	17.3	0.1
2458384.717	14.07	P48+ZTF	g	17.3	0.1
2458384.7384	14.09	P48+ZTF	g	17.2	0.0
2458385.6151	14.97	P48+ZTF	g	17.4	0.0
2458385.633	14.99	P48+ZTF	g	17.4	0.0
2458385.633	14.99	P48+ZTF	g	17.4	0.0
2458385.6622	15.01	P48+ZTF	g	17.5	0.0
2458385.6622	15.01	P48+ZTF	g	17.5	0.0
2458385.6844	15.04	P48+ZTF	r	16.9	0.0
2458385.6844	15.04	P48+ZTF	r	16.9	0.0
2458385.6919	15.04	P48+ZTF	r	16.9	0.0
2458385.6919	15.04	P48+ZTF	r	16.9	0.0
2458385.7117	15.06	P48+ZTF	r	16.9	0.0
2458385.7117	15.06	P48+ZTF	r	16.9	0.0
2458386.6167	15.97	P48+ZTF	g	17.6	0.1
2458386.6242	15.98	P48+ZTF	g	17.7	0.1
2458386.6242	15.98	P48+ZTF	g	17.7	0.1
2458386.6404	15.99	P48+ZTF	g	17.6	0.1
2458386.6546	16.01	P48+ZTF	g	17.6	0.1
2458386.6994	16.05	P48+ZTF	r	17.0	0.0
2458386.6994	16.05	P48+ZTF	r	17.0	0.0
2458386.7013	16.05	P48+ZTF	r	17.0	0.0
2458386.7158	16.07	P48+ZTF	r	17.0	0.0
2458386.7377	16.09	P48+ZTF	r	17.0	0.0
2458387.6227	16.98	P48+ZTF	r	17.1	0.0
2458387.6227	16.98	P48+ZTF	r	17.1	0.0
2458387.6399	16.99	P48+ZTF	r	17.1	0.0
2458387.6541	17.01	P48+ZTF	r	17.2	0.0
2458387.6541	17.01	P48+ZTF	r	17.2	0.0
2458387.6822	17.03	P48+ZTF	g	17.8	0.1
2458387.6822	17.03	P48+ZTF	g	17.8	0.1
2458387.7041	17.06	P48+ZTF	g	17.8	0.1
2458387.7041	17.06	P48+ZTF	g	17.8	0.1
2458387.7232	17.08	P48+ZTF	g	17.9	0.1

Table 5 continued on next page

Table 5 *(continued)*

Date (JD)	Δt	Instrument	Filter	AB Mag	Error in AB Mag
2458387.7232	17.08	P48+ZTF	g	17.9	0.1
2458388.6124	17.97	P60+SEDM	r	17.2	0.0
2458388.6154	17.97	P48+ZTF	g	18.0	0.1
2458388.6154	17.97	P48+ZTF	g	18.0	0.1
2458388.6396	17.99	P48+ZTF	g	18.0	0.1
2458388.6396	17.99	P48+ZTF	g	18.0	0.1
2458388.6542	18.01	P48+ZTF	g	18.0	0.1
2458388.6542	18.01	P48+ZTF	g	18.0	0.1
2458388.6834	18.04	P48+ZTF	r	17.3	0.1
2458388.6936	18.05	P48+ZTF	r	17.3	0.0
2458388.7203	18.07	P48+ZTF	r	17.2	0.1
2458389.6156	18.97	P48+ZTF	r	17.4	0.1
2458389.6227	18.98	P48+ZTF	r	17.4	0.0
2458389.6317	18.98	P48+ZTF	g	18.2	0.1
2458389.6317	18.98	P48+ZTF	g	18.2	0.1
2458389.6416	18.99	P48+ZTF	g	18.2	0.1
2458389.6416	18.99	P48+ZTF	g	18.2	0.1
2458389.6804	19.03	P48+ZTF	g	18.2	0.1
2458389.6804	19.03	P48+ZTF	g	18.2	0.1
2458389.6947	19.05	P48+ZTF	g	18.2	0.1
2458389.6947	19.05	P48+ZTF	g	18.2	0.1
2458389.7166	19.07	P48+ZTF	r	17.4	0.0
2458389.7476	19.1	P48+ZTF	r	17.4	0.0
2458390.6228	19.98	P48+ZTF	g	18.4	0.1
2458390.6228	19.98	P48+ZTF	g	18.4	0.1
2458390.6326	19.99	P48+ZTF	g	18.4	0.1
2458390.6326	19.99	P48+ZTF	g	18.4	0.1
2458390.6797	20.03	P48+ZTF	r	17.6	0.0
2458390.7209	20.07	P48+ZTF	r	17.6	0.1
2458390.7347	20.09	P48+ZTF	r	17.5	0.0
2458399.5989	28.95	P48+ZTF	g	19.4	0.2
2458399.5989	28.95	P48+ZTF	g	19.4	0.2
2458400.6307	29.98	P48+ZTF	g	19.5	0.1
2458400.6638	30.02	P48+ZTF	r	18.7	0.1
2458400.6756	30.03	P48+ZTF	r	18.7	0.1
2458400.6756	30.03	P48+ZTF	r	18.7	0.1
2458400.6987	30.05	P48+ZTF	r	18.6	0.1
2458415.6169	44.97	P60+SEDM	r	19.6	0.1
2458415.6196	44.97	P60+SEDM	g	20.2	0.2
2458415.6223	44.98	P60+SEDM	i	19.4	0.1
2458420.593	49.95	P60+SEDM	r	19.7	0.0
2458420.5958	49.95	P60+SEDM	g	20.7	0.1
2458420.5984	49.95	P60+SEDM	i	19.5	0.0

Table 5 continued on next page

Table 5 *(continued)*

Date (JD)	Δt	Instrument	Filter	AB Mag	Error in AB Mag
2458420.6011	49.95	P60+SEDM	r	19.8	0.0
2458420.6038	49.96	P60+SEDM	g	20.9	0.1
2458423.584	52.94	P60+SEDM	r	19.8	0.1
2458423.5894	52.94	P60+SEDM	i	19.7	0.1
2458429.5848	58.94	P60+SEDM	r	20.0	0.1
2458429.5875	58.94	P60+SEDM	g	21.3	0.1
2458429.5902	58.94	P60+SEDM	i	19.8	0.0
2458371.3802	0.73	LT	u	16.1	0.0
2458372.3561	1.71	LT	u	15.7	0.0
2458373.3944	2.75	LT	u	15.8	0.0
2458380.3607	9.71	LT	u	17.1	0.0
2458380.3612	9.71	LT	u	17.1	0.0
2458381.3403	10.69	LT	u	17.5	0.0
2458381.3409	10.69	LT	u	17.6	0.0
2458382.3451	11.7	LT	u	18.0	0.0
2458383.3399	12.69	LT	u	18.3	0.1
2458383.3404	12.69	LT	u	18.3	0.1
2458384.34	13.69	LT	u	18.7	0.1
2458384.3405	13.69	LT	u	18.9	0.1
2458385.339	14.69	LT	u	18.9	0.1
2458386.3369	15.69	LT	u	19.2	0.2
2458388.3375	17.69	LT	u	20.1	0.2
2458388.338	17.69	LT	u	19.9	0.3
2458391.3458	20.7	LT	u	20.1	0.2
2458371.3794	0.73	LT	g	16.6	0.0
2458372.3554	1.71	LT	g	16.2	0.0
2458373.3951	2.75	LT	g	16.0	0.0
2458380.3599	9.71	LT	g	16.6	0.0
2458381.3396	10.69	LT	g	16.7	0.0
2458382.3438	11.7	LT	g	16.9	0.0
2458383.3391	12.69	LT	g	17.0	0.0
2458384.3392	13.69	LT	g	17.3	0.0
2458385.3377	14.69	LT	g	17.5	0.0
2458386.3362	15.69	LT	g	17.6	0.1
2458388.3367	17.69	LT	g	18.1	0.0
2458389.3394	18.69	LT	g	18.2	0.0
2458390.367	19.72	LT	g	18.3	0.1
2458391.3445	20.7	LT	g	18.6	0.0
2458393.3452	22.7	LT	g	18.9	0.0
2458394.3463	23.7	LT	g	19.0	0.0
2458395.3462	24.7	LT	g	19.2	0.0
2458396.3496	25.7	LT	g	19.3	0.0
2458397.3884	26.74	LT	g	19.5	0.0

Table 5 continued on next page

Table 5 *(continued)*

Date (JD)	Δt	Instrument	Filter	AB Mag	Error in AB Mag
2458407.3531	36.71	LT	g	20.1	0.1
2458407.3537	36.71	LT	g	20.2	0.1
2458408.3179	37.67	LT	g	20.3	0.1
2458408.3186	37.67	LT	g	20.1	0.1
2458409.3255	38.68	LT	g	20.2	0.1
2458409.3262	38.68	LT	g	20.3	0.1
2458371.3787	0.73	LT	r	16.9	0.0
2458372.3546	1.71	LT	r	16.4	0.0
2458373.3958	2.75	LT	r	16.3	0.0
2458380.3592	9.71	LT	r	16.5	0.0
2458381.3389	10.69	LT	r	16.5	0.0
2458382.3431	11.7	LT	r	16.6	0.0
2458383.3384	12.69	LT	r	16.7	0.0
2458384.3385	13.69	LT	r	16.8	0.0
2458385.337	14.69	LT	r	16.9	0.0
2458386.3354	15.69	LT	r	17.1	0.0
2458388.336	17.69	LT	r	17.3	0.0
2458389.3387	18.69	LT	r	17.4	0.0
2458390.3663	19.72	LT	r	17.6	0.0
2458391.3438	20.7	LT	r	17.7	0.0
2458393.3444	22.7	LT	r	17.9	0.0
2458394.3456	23.7	LT	r	18.1	0.0
2458395.3455	24.7	LT	r	18.1	0.0
2458396.3489	25.7	LT	r	18.3	0.0
2458397.3877	26.74	LT	r	18.4	0.0
2458407.3524	36.71	LT	r	19.2	0.0
2458408.317	37.67	LT	r	19.3	0.0
2458409.3246	38.68	LT	r	19.4	0.2
2458371.378	0.73	LT	i	17.3	0.0
2458372.3539	1.71	LT	i	16.9	0.0
2458373.3965	2.75	LT	i	16.6	0.0
2458380.3585	9.71	LT	i	16.8	0.0
2458381.3381	10.69	LT	i	16.8	0.0
2458382.3424	11.7	LT	i	16.9	0.0
2458383.3377	12.69	LT	i	16.9	0.0
2458384.3378	13.69	LT	i	17.0	0.2
2458385.3363	14.69	LT	i	17.0	0.0
2458386.3347	15.69	LT	i	17.1	0.0
2458388.3353	17.69	LT	i	17.3	0.0
2458389.338	18.69	LT	i	17.4	0.0
2458390.3656	19.72	LT	i	17.6	0.0
2458391.3431	20.7	LT	i	17.6	0.0
2458393.3437	22.7	LT	i	17.8	0.0

Table 5 continued on next page

Table 5 *(continued)*

Date (JD)	Δt	Instrument	Filter	AB Mag	Error in AB Mag
2458394.3449	23.7	LT	i	18.0	0.0
2458395.3448	24.7	LT	i	18.1	0.0
2458396.3481	25.7	LT	i	18.2	0.0
2458397.3869	26.74	LT	i	18.3	0.0
2458407.3517	36.7	LT	i	19.0	0.0
2458408.3162	37.67	LT	i	19.0	0.1
2458409.3238	38.68	LT	i	19.1	0.1
2458373.3972	2.75	LT	z	16.8	0.0
2458380.3577	9.71	LT	z	16.8	0.0
2458381.3374	10.69	LT	z	16.8	0.0
2458382.3416	11.69	LT	z	16.8	0.0
2458383.3369	12.69	LT	z	16.8	0.0
2458384.337	13.69	LT	z	16.8	0.0
2458385.3355	14.69	LT	z	16.9	0.0
2458386.334	15.69	LT	z	16.9	0.0
2458388.3345	17.69	LT	z	17.0	0.0
2458389.3372	18.69	LT	z	17.1	0.0
2458390.3648	19.72	LT	z	17.2	0.1
2458391.3423	20.7	LT	z	17.3	0.0
2458393.343	22.7	LT	z	17.4	0.0
2458394.3441	23.7	LT	z	17.6	0.0
2458395.344	24.7	LT	z	17.7	0.0
2458396.3474	25.7	LT	z	17.7	0.0
2458397.3862	26.74	LT	z	17.8	0.0
2458407.3509	36.7	LT	z	18.2	0.0
2458408.3155	37.67	LT	z	18.3	0.1
2458409.3231	38.68	LT	z	18.3	0.1
2458374.9769	4.33	LOT	g	16.1	0.0
2458375.9702	5.32	LOT	g	16.2	0.0
2458379.9736	9.33	LOT	g	16.6	0.0
2458381.0023	10.36	LOT	g	16.8	0.0
2458381.9909	11.34	LOT	g	16.9	0.0
2458386.0102	15.36	LOT	g	17.6	0.0
2458391.0243	20.38	LOT	g	18.6	0.0
2458391.9648	21.32	LOT	g	18.7	0.0
2458392.9823	22.34	LOT	g	18.8	0.0
2458393.9679	23.32	LOT	g	19.0	0.0
2458394.9508	24.3	LOT	g	19.2	0.0
2458395.9525	25.31	LOT	g	19.3	0.0
2458396.9584	26.31	LOT	g	19.4	0.0
2458406.9893	36.34	LOT	g	20.3	0.1
2458411.95	41.3	LOT	g	20.5	0.1
2458374.9847	4.34	LOT	i	16.5	0.0

Table 5 continued on next page

Table 5 *(continued)*

Date (JD)	Δt	Instrument	Filter	AB Mag	Error in AB Mag
2458379.9812	9.33	LOT	i	16.7	0.0
2458381.01	10.36	LOT	i	16.8	0.0
2458381.9986	11.35	LOT	i	16.8	0.0
2458386.018	15.37	LOT	i	17.0	0.0
2458391.0321	20.38	LOT	i	17.6	0.0
2458391.9726	21.33	LOT	i	17.7	0.0
2458392.9901	22.34	LOT	i	17.8	0.0
2458393.9756	23.33	LOT	i	18.0	0.0
2458394.9692	24.32	LOT	i	18.1	0.0
2458395.9603	25.31	LOT	i	18.2	0.0
2458396.978	26.33	LOT	i	18.3	0.0
2458406.9971	36.35	LOT	i	18.9	0.0
2458411.9578	41.31	LOT	i	19.1	0.0
2458374.9807	4.33	LOT	r	16.3	0.0
2458375.974	5.33	LOT	r	16.3	0.0
2458379.9774	9.33	LOT	r	16.5	0.0
2458381.0061	10.36	LOT	r	16.6	0.0
2458381.9947	11.35	LOT	r	16.6	0.0
2458386.014	15.37	LOT	r	17.0	0.0
2458391.0282	20.38	LOT	r	17.7	0.0
2458391.9686	21.32	LOT	r	17.8	0.0
2458392.9862	22.34	LOT	r	17.9	0.0
2458393.9717	23.32	LOT	r	18.1	0.0
2458394.9653	24.32	LOT	r	18.2	0.0
2458395.9564	25.31	LOT	r	18.3	0.0
2458396.9623	26.31	LOT	r	18.4	0.0
2458406.9932	36.35	LOT	r	19.1	0.0
2458411.9538	41.31	LOT	r	19.4	0.0
2458371.0917	0.44	UVOT	B	16.8	0.1
2458371.1601	0.51	UVOT	B	16.7	0.1
2458373.8837	3.24	UVOT	B	15.9	0.1
2458374.0828	3.44	UVOT	B	15.9	0.1
2458374.481	3.83	UVOT	B	15.9	0.1
2458375.3416	4.69	UVOT	B	16.1	0.1
2458376.48	5.83	UVOT	B	16.0	0.1
2458376.599	5.95	UVOT	B	16.2	0.1
2458379.2575	8.61	UVOT	B	16.5	0.1
2458380.184	9.54	UVOT	B	16.5	0.1
2458380.3172	9.67	UVOT	B	16.7	0.1
2458380.7873	10.14	UVOT	B	16.8	0.1
2458381.6447	11.0	UVOT	B	17.3	0.1
2458381.7774	11.13	UVOT	B	16.8	0.1
2458381.8438	11.2	UVOT	B	17.0	0.1

Table 5 continued on next page

Table 5 *(continued)*

Date (JD)	Δt	Instrument	Filter	AB Mag	Error in AB Mag
2458383.3045	12.66	UVOT	B	17.7	0.2
2458383.3705	12.72	UVOT	B	17.4	0.1
2458384.3114	13.66	UVOT	B	17.4	0.1
2458371.0908	0.44	UVOT	U	16.4	0.1
2458371.1591	0.51	UVOT	U	16.2	0.1
2458373.8834	3.24	UVOT	U	15.7	0.1
2458374.0825	3.44	UVOT	U	15.7	0.1
2458374.4806	3.83	UVOT	U	15.8	0.1
2458375.3411	4.69	UVOT	U	15.7	0.1
2458376.4794	5.83	UVOT	U	16.0	0.1
2458376.5986	5.95	UVOT	U	15.8	0.1
2458379.2569	8.61	UVOT	U	16.7	0.1
2458380.1836	9.54	UVOT	U	17.2	0.1
2458380.3168	9.67	UVOT	U	17.3	0.1
2458380.7866	10.14	UVOT	U	17.3	0.1
2458381.6444	11.0	UVOT	U	17.7	0.1
2458381.7771	11.13	UVOT	U	17.9	0.2
2458381.8435	11.2	UVOT	U	18.1	0.2
2458383.3041	12.66	UVOT	U	18.8	0.2
2458383.37	12.72	UVOT	U	18.4	0.2
2458384.3105	13.66	UVOT	U	19.0	0.2
2458371.1013	0.45	UVOT	UVM2	15.7	0.0
2458371.1669	0.52	UVOT	UVM2	15.6	0.1
2458373.8864	3.24	UVOT	UVM2	15.2	0.1
2458374.0856	3.44	UVOT	UVM2	15.2	0.1
2458374.4841	3.84	UVOT	UVM2	15.4	0.1
2458375.3466	4.7	UVOT	UVM2	15.9	0.1
2458376.4854	5.84	UVOT	UVM2	16.7	0.1
2458376.6032	5.96	UVOT	UVM2	16.8	0.1
2458379.2631	8.62	UVOT	UVM2	19.8	0.2
2458380.1881	9.54	UVOT	UVM2	20.1	0.3
2458380.3209	9.67	UVOT	UVM2	20.3	0.4
2458380.7945	10.15	UVOT	UVM2	21.3	0.6
2458381.648	11.0	UVOT	UVM2	21.1	0.7
2458381.7807	11.13	UVOT	UVM2	20.6	0.4
2458381.8472	11.2	UVOT	UVM2	21.9	1.2
2458383.3088	12.66	UVOT	UVM2	21.4	0.8
2458383.3752	12.73	UVOT	UVM2	22.1	1.4
2458384.3213	13.67	UVOT	UVM2	26.7	76.2
2458371.0893	0.44	UVOT	UVW1	15.9	0.1
2458371.1577	0.51	UVOT	UVW1	15.8	0.0
2458373.8829	3.24	UVOT	UVW1	15.3	0.1
2458374.082	3.43	UVOT	UVW1	15.2	0.1

Table 5 continued on next page

Table 5 *(continued)*

Date (JD)	Δt	Instrument	Filter	AB Mag	Error in AB Mag
2458374.4801	3.83	UVOT	UVW1	15.4	0.1
2458375.3402	4.69	UVOT	UVW1	15.7	0.1
2458376.4784	5.83	UVOT	UVW1	16.4	0.1
2458376.5979	5.95	UVOT	UVW1	16.5	0.1
2458379.2558	8.61	UVOT	UVW1	17.9	0.1
2458380.1828	9.54	UVOT	UVW1	18.7	0.1
2458380.3161	9.67	UVOT	UVW1	19.1	0.2
2458380.7853	10.14	UVOT	UVW1	18.8	0.1
2458381.6437	11.0	UVOT	UVW1	19.1	0.2
2458381.7765	11.13	UVOT	UVW1	19.4	0.3
2458381.8429	11.2	UVOT	UVW1	20.0	0.4
2458383.3033	12.66	UVOT	UVW1	20.2	0.4
2458383.3692	12.72	UVOT	UVW1	20.7	0.6
2458384.3086	13.66	UVOT	UVW1	20.6	0.3
2458371.0941	0.45	UVOT	UVW2	15.5	0.1
2458371.1625	0.52	UVOT	UVW2	15.4	0.1
2458373.8845	3.24	UVOT	UVW2	15.6	0.1
2458374.0835	3.44	UVOT	UVW2	15.7	0.1
2458374.4818	3.83	UVOT	UVW2	15.9	0.1
2458375.343	4.7	UVOT	UVW2	16.4	0.1
2458376.4815	5.83	UVOT	UVW2	17.1	0.1
2458376.6002	5.95	UVOT	UVW2	17.3	0.1
2458379.2591	8.61	UVOT	UVW2	19.6	0.2
2458380.1852	9.54	UVOT	UVW2	20.1	0.3
2458380.3183	9.67	UVOT	UVW2	20.3	0.3
2458380.7894	10.14	UVOT	UVW2	20.4	0.3
2458381.6457	11.0	UVOT	UVW2	20.2	0.3
2458381.7783	11.13	UVOT	UVW2	20.9	0.6
2458381.8447	11.2	UVOT	UVW2	21.6	1.0
2458383.3057	12.66	UVOT	UVW2	21.5	0.9
2458383.3718	12.72	UVOT	UVW2	21.8	1.0
2458384.3142	13.67	UVOT	UVW2	21.2	0.5
2458371.0965	0.45	UVOT	V	17.3	0.1
2458371.1649	0.52	UVOT	V	16.8	0.1
2458373.8852	3.24	UVOT	V	16.2	0.1
2458374.0843	3.44	UVOT	V	16.1	0.1
2458374.4827	3.84	UVOT	V	16.1	0.1
2458375.3444	4.7	UVOT	V	16.2	0.1
2458376.483	5.84	UVOT	V	16.1	0.1
2458376.6013	5.95	UVOT	V	16.0	0.1
2458379.2607	8.61	UVOT	V	16.4	0.1
2458380.1863	9.54	UVOT	V	16.4	0.1
2458380.3193	9.67	UVOT	V	16.6	0.2

Table 5 continued on next page

Table 5 *(continued)*

Date (JD)	Δt	Instrument	Filter	AB Mag	Error in AB Mag
2458380.7914	10.14	UVOT	V	16.6	0.1
2458381.6466	11.0	UVOT	V	16.6	0.2
2458381.7793	11.13	UVOT	V	16.7	0.2
2458381.8456	11.2	UVOT	V	16.5	0.2
2458383.3069	12.66	UVOT	V	16.6	0.1
2458383.3731	12.73	UVOT	V	16.7	0.1
2458384.317	13.67	UVOT	V	16.9	0.1

B. UV AND OPTICAL SPECTROSCOPY

The full spectral sequence is shown in Figure 24, and the log is presented in Table 6.

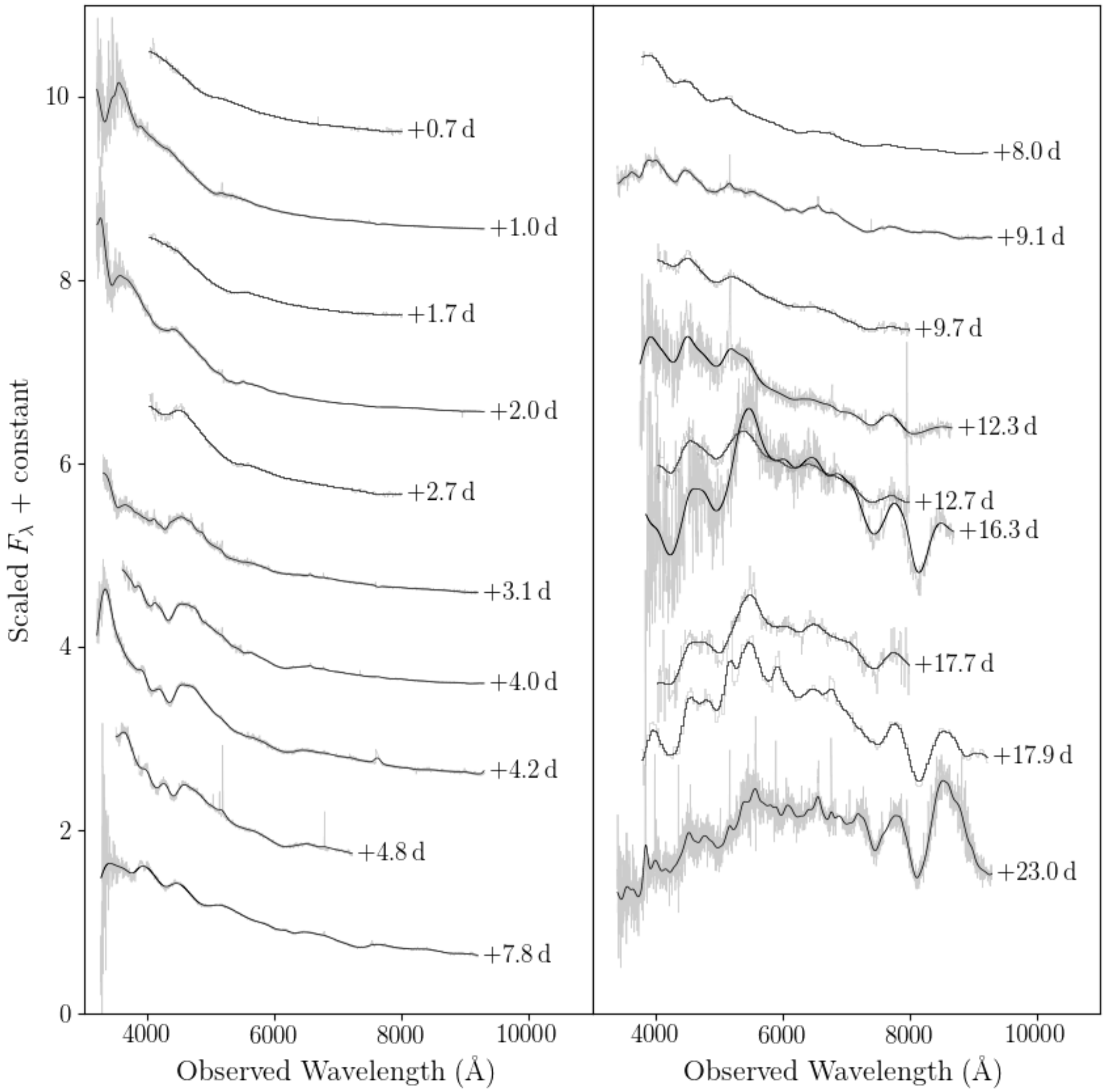

Figure 24. Ground-based optical spectra of SN2018gep. The light grey represents the observed spectrum, interpolating over host emission lines and telluric features. The black line is a Gaussian-smoothed version of the spectrum, using a Gaussian width that is several times the width of a galaxy emission line at that resolution. For more details on the smoothing procedure, see Section 2.1 of Ho et al. (2017).

Table 6. Log of SN2018gep optical spectra

Start Time (UTC)	Δt	Instrument	Exp. Time (s)	Airmass
2018 Sep 09 20:30:01	0.7	LT+SPRAT	1200	1.107

Table 6 continued on next page

Table 6 *(continued)*

Start Time (UTC)	Δt	Instrument	Exp. Time (s)	Airmass
2018 Sep 10 04:28:51	1.0	P200+DBSP	600	1.283
2018 Sep 10 21:03:42	1.7	LT+SPRAT	900	1.182
2018 Sep 11 04:59:19	2.0	P200+DBSP	600	1.419
2018 Sep 11 20:22:35	2.7	LT+SPRAT	900	1.107
2018 Sep 12 06:09:59	3.1	P200+DBSP		
2018 Sep 13 03:52:58	4.0	P200+DBSP	300	1.209
2018 Sep 13 09:17:25	4.2	Keck1+LRIS	300	3.483
2018 Sep 14 02:44:24.24	4.8	DCT+Deveny+LMI	300	1.11
2018 Sep 17 04:38:40	8.0	P60+SEDM	1440	1.435
2018 Sep 17 20:40:25.750	8.7	NOT+ALFOSC	1800	1.19
2018 Sep 18 05:21:58	9.1	P200+DBSP	600	1.720
2018 Sep 18 20:14:35	9.7	LT+SPRAT	1000	1.143
2018 Sep 21 11:15:10	12.3	XLT+BFOSC	3000	1.181
2018 Sep 21 20:58:21	12.7	LT+SPRAT	1000	1.293
2018 Sep 25 11:16:43	16.3	XLT+BFOSC	3000	1.225
2018 Sep 26 20:22:54	17.7	LT+SPRAT	1000	1.242
2018 Sep 27 02:42:29	17.9	P60+SEDM	1440	1.172
2018 Oct 02 04:34:35	23.0	P200+DBSP	600	1.780
2018 Nov 09 05:26:17	61.1	Keck1+LRIS	900	3.242

Note—Gratings used: Wasatch600 (LT+SPRAT), Gr4 (NOT+ALFOSC), 600/4000 (P200+DBSP; blue side), 316/7500 (P200+DBSP; red side), 400/8500 (Keck1+LRIS; red side).
Filters used: 400nm (LT+SPRAT), open (NOT+ALFOSC), clear (Keck1+LRIS)
Wavelength range: 4020–7995 Å (LT+SPRAT), 3200–9600 Å (NOT+ALFOSC), 1759–10311 Å (Keck1+LRIS), 3777–9223 Å (P60+SEDM)
Resolution: 20 (LT+SPRAT), 710 (NOT+ALFOSC)

C. ATOMIC DATA FOR SPECTRAL MODELING

The atomic data used for the spectral modelling in Section 3.2 is the same as described in Appendix A.4 of Ergon et al. (2018), but with the following modifications. The stage II-IV ions where (whenever possible) updated to include at least 50 levels for N, Na, Al, Ar and Ca, at least 100 levels for C, O, Ne, Mg, Si and S, and at least 300 levels for Sc, Ti, V, Cr, Mn, Fe, Co and Ni. In addition we updated the C II - C IV and O II - O III ions with specific recombination rates from the online table by S. Nahar[14].

D. DATA FOR MEASURING HOST PROPERTIES

[14] http://www.astronomy.ohio-state.edu/~nahar/_naharradiativeatomicdata/

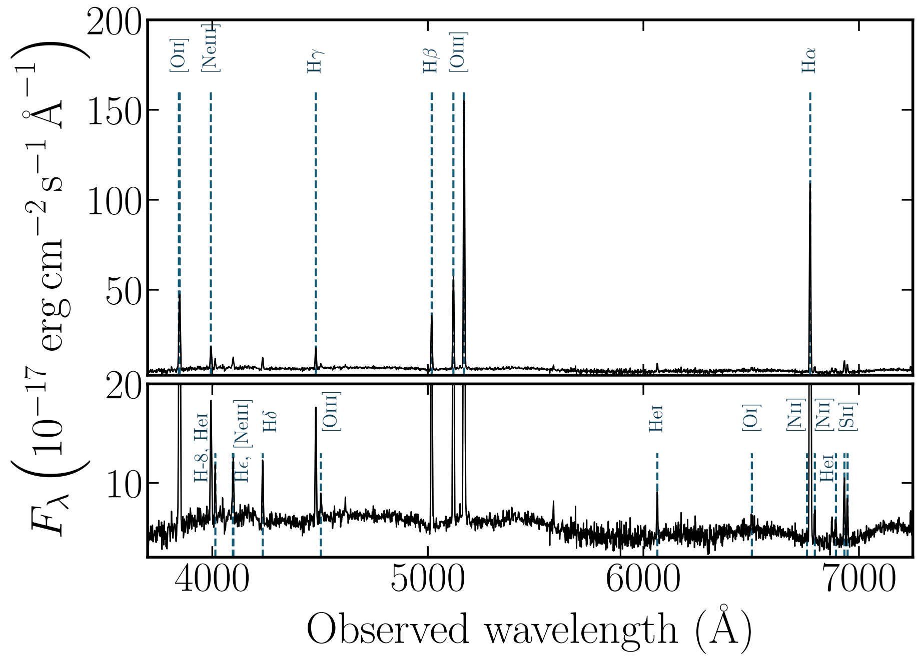

Figure 25. Host spectrum of SN2018gep obtained with Keck/LRIS on 9 November 2018, about two months after explosion. Strong emission lines from the host galaxy are labeled. The low host metallicity of 0.1 solar is reflected by very small N II/Hα flux ratio. The large rest-frame [O III]λ5007 equivalent width of > 160 Å puts the host also in regime of extreme emission-line galaxies. These galaxy class constitute $< 2\%$ of all star-forming galaxies at $z < 0.3$ in the SDSS DR15 catalogue. The undulations are due to the supernova. The spectrum is truncated at 7250 Å for presentation purposes, and it is corrected for Galactic reddening.

Table 7. Line fluxes from the host galaxy of SN2018gep extracted from the Keck/LRIS spectrum obtained on 9 November 2018.

Transition	$\lambda_{\rm obs}$ (Å)	F $\left(10^{-17}\ {\rm erg\,cm^{-2}\,s^{-1}}\right)$
[O II]$\lambda\lambda$3726,3729	3848.17 ± 0.05	334.5 ± 6.23
[Ne III]λ3869	3993.50 ± 0.16	82.34 ± 6.18
He Iλ3889,H-8	4014.49 ± 0.16	29.01 ± 4.73
[Ne III]λ3968,Hϵ	4096.66 ± 0.26	36.61 ± 3.98
Hδ	4233.87 ± 0.13	44.88 ± 2.59
Hγ	4480.20 ± 0.10	81.95 ± 3.74
[O III]λ4364	4503.68 ± 0.10	15.01 ± 2.69
Hβ	5017.87 ± 0.08	213.41 ± 10.53
[O III]λ4960	5118.61 ± 0.04	352.42 ± 6.50
[O III]λ5008	5168.04 ± 0.04	1066.70 ± 19.50
He Iλ5877	6064.21 ± 0.20	27.04 ± 2.30
O Iλ6302	6502.18 ± 1.08	6.72 ± 2.94
[N II]λ6549	6758.16 ± 0.02	11.15 ± 6.73
Hα	6773.40 ± 0.02	723.85 ± 7.65
[N II]λ6585	6794.67 ± 0.02	19.01 ± 5.76
[He I]λ6678	6890.29 ± 0.14	7.88 ± 2.19
[S II]λ6718	6931.83 ± 0.10	41.76 ± 2.38
[S II]λ6732	6946.68 ± 0.10	28.15 ± 2.19

Note—All measurements are corrected for Galactic reddening.

Table 8. Brightness of the host galaxy from UV ot IR wavelenghts

Instrument/ Filter	$\lambda_{\rm eff}$ (Å)	Brightness (mag)	Instrument/ Filter	$\lambda_{\rm eff}$ (Å)	Brightness (mag)
GALEX/FUV	1542.3	20.20 ± 0.03	SDSS/i'	7439.5	18.62 ± 0.04
GALEX/NUV	2274.4	20.09 ± 0.03	SDSS/z'	8897.1	18.59 ± 0.12
UVOT/$w2$	2030.5	19.91 ± 0.12	PS1/$g_{\rm PS1}$	4775.6	18.96 ± 0.04
UVOT/$m2$	2228.1	20.00 ± 0.14	PS1/$r_{\rm PS1}$	6129.5	18.82 ± 0.04
UVOT/$w1$	2589.1	20.11 ± 0.16	PS1/$i_{\rm PS1}$	7484.6	18.88 ± 0.04
UVOT/u	3501.2	19.74 ± 0.16	PS1/$z_{\rm PS1}$	8657.8	18.71 ± 0.05
UVOT/b	4328.6	19.45 ± 0.20	WIRCam/J	12481.5	18.99 ± 0.09
UVOT/v	5402.1	18.45 ± 0.21	2MASS/H	16620.0	18.33 ± 0.36
SDSS/u'	3594.9	19.97 ± 0.12	WISE/$W1$	33526.0	19.39 ± 0.08
SDSS/g'	4640.4	18.88 ± 0.02	WISE/$W2$	46028.0	19.85 ± 0.19
SDSS/r'	6122.3	18.76 ± 0.05			

Note—All measurements are reported in the AB system and are not corrected for reddening. For guidance, we report the effective wavelengths of each filter.